Coiled-coil homo-oligomerization and disaggregase Hsp104 act in parallel to stabilize orphan septins (100 characters)

Italo A Cavini*, Randi M Yeager, Alejandra Velasquez, Andressa P A Pinto, Ana Paula U Araujo, Richard C Garratt, Michael A McMurray*

Department of Cell and Developmental Biology University of Colorado Anschultz Medical Campus School of Medicine, USA
Biophysical and Structural Biology Group, Institute of Physics of São Carlos, University of São Paulo, Brazil
School of Pharmaceutical Sciences of Ribeirão Preto, University of São Paulo, Brazil

ABSTRACT

Multiple septin family proteins co-assemble with strict subunit stoichiometry into hetero-oligomers. In the absence of native septin partners, purified septins aggregate in vitro, and "orphan" septins are found in pathological aggregates associated with neurodegenerative diseases. Cytosolic chaperones bind the septin GTPase domain to promote on-pathway septin folding but it was unclear how cells manage orphan septins to maintain septin subunit stoichiometry. Most septins have C-terminal domains (CTDs) that form heteromeric coiled coils within or between septin complexes. Here we present evidence that orphan yeast septins are protected from proteasomal degradation by forming transient coiled-coil homodimers and trimers and, in parallel, by the disaggregase chaperone Hsp104. Septins unable to undergo CTD-mediated homo-oligomerization require Hsp104 to accumulate to super-stoichiometric levels. We show that the number of septin-encoding mRNAs per yeast cell is low and variable, creating opportunities for transient subunit imbalances. These findings reveal a novel role for coiled coils and the cellular proteostasis machinery in the fidelity of higher-order septin assembly.

INTRODUCTION

The septin family of eukaryotic filament-forming proteins function in cellular morphogenesis, intracellular trafficking, and cytokinesis, among other processes (Mostowy and Cossart, 2012). In humans and budding yeast, filaments form via polymerization of rod-shaped septin hetero-octamers into which two molecules of each of four septin subunits assemble via alternating interfaces on opposite faces of a globular GTPase domain (Sirajuddin *et al.*, 2007; Bertin *et al.*, 2008; McMurray and Thorner, 2019; Mendonça *et al.*, 2019; Soroor *et al.*, 2021) (Fig.1A). Neuronal septins involved in synaptic plasticity have been found in protein aggregates associated with human neurodegenerative diseases (reviewed in (Marttinen *et al.*, 2015; Alkhanjari *et al.*, 2025)), and in the absence of native hetero-dimerization partners, human septins can form amyloid-like fibrils in vitro with properties indicative of cross-β sheet aggregation (Garcia *et al.*, 2007; Pissuti Damalio *et al.*, 2012; Kumagai *et al.*, 2019). Indeed, a septin was the first identified substrate of Parkin, an E3 ubiquitin-protein ligase, mutations in which are responsible for early-onset Parkinson disease (Zhang *et al.*, 2000). A model that emerges from these findings is that excess of a single septin protein creates a scenario in which unoccupied hetero-oligomerization interfaces mediate the assembly of dysfunctional homo-oligomers that can perturb normal septin function. However, we know few molecular details about how cells manage septin homo-oligomerization to maintain normal function.

In addition to the GTPase domain, most septins have extended CTDs with the propensity to form coiled coils (reviewed in (Cavini *et al.*, 2021)). Septin coiled-coil-forming sequences are the targets of viral proteases that perturb cellular function (Li *et al.*, 2019; Lee *et al.*, 2023), but it remains unclear exactly how septin coiled coil assembly fits into the mechanism of septin rod and filament assembly (Sala *et al.*, 2016). For example, in addition to parallel hetero-dimeric coiled coils, it has been proposed that the CTDs of the budding yeast septins Cdc3 and Cdc12 form anti-parallel four-helix coiled-coil bundles when filaments pair side-by-side (Bertin *et al.*, 2008) (Fig. 1A). Both may be true: in the coiled coils formed by human septins both parallel and anti-parallel arrangements are energetically favorable and individual septins may switch between them (Leonardo *et al.*, 2021).

Such “metastability” may be important in allowing dynamic changes in septin organization/assembly. Indeed, a short helical region of the CTD of Cdc12 (residues 382-399) has amphipathic properties that allow septin rods to sense membrane curvature (Cannon *et al.*, 2019; Woods *et al.*, 2021) (Fig.1A). The same hydrophobic Cdc12 residues predicted to be immersed in the inner leaflet of the plasma membrane are also predicted to be engaged in a heterodimeric coiled coil with the CTD of Cdc3 (Fig.1B,C). If the same Cdc12 molecule participates in both kinds of interactions, the Cdc12–Cdc3 coiled coil must undergo some degree of “unzipping” when a rod or

filament binds a curved membrane, which metastability would facilitate. Unzipping would not destabilize septin rods or filaments, since Cdc3 and Cdc12 interact stably within hetero-octamers even when Cdc12 residues 318-407 are missing (Bertin *et al.*, 2010). The CTD of septin Shs1 mediates interaction with the CTD of septin Cdc11 (Versele *et al.*, 2004; Finnigan *et al.*, 2015b) and also harbors its own curvature-sensing amphipathic helix (Woods *et al.*, 2021) as well as a predicted coiled-coil-forming sequence that is sufficient to recruit a non-septin protein to septin filaments in vivo (Finnigan *et al.*, 2015a, 2015b). Hence septin coiled-coil-forming sequences may engage in multiple distinct modes of interaction with other molecules before and/or after incorporation of a septin into a hetero-octameric rod, but such dynamic interactions have not yet been defined.

At steady-state, there are very few septin monomers or sub-octameric septin hetero-oligomers in wild-type budding yeast cells (Frazier *et al.*, 1998; Vrabioiu *et al.*, 2004; Farkasovsky *et al.*, 2005; Bridges *et al.*, 2014; Johnson *et al.*, 2015) and in wild-type human cells septins exist solely as hetero-hexamers or -octamers (Sellin *et al.*, 2011b, 2011a, 2014; Kuzmić *et al.*, 2022). We proposed that Cdc12 normally acts as a slowly translated platform for efficient co-translational assembly of yeast septin hetero-octamers (Hassell *et al.*, 2022). Since hetero-octamer assembly requires strict 2:2:2:2 stoichiometry of septin subunits, excess Cdc12 would complete translation with one or more interfaces left unengaged with a partner septin. Cytosolic chaperone proteins co-translationally bind nascent septins as the GTPase domain folds and compete transiently with partner septins to engage the G interface (Johnson *et al.*, 2015; Stein *et al.*, 2019; Denney *et al.*, 2021; Hassell *et al.*, 2022), which encompasses the GTP-binding pocket (Fig. 1A) and includes a region with high predicted propensity for β aggregation (Pissuti Damalio *et al.*, 2012; Hassell *et al.*, 2022). Engaging the G interface in a native septin-septin heterodimer prevents human septin aggregation in vitro (Kumagai *et al.*, 2019).

By experimentally overexpressing Cdc12, we showed that post-translational hetero-octamer assembly is possible but it requires cytosolic chaperones of the chaperonin and Hsp70 families (Hassell *et al.*, 2022), presumably to maintain the excess Cdc12 in a conformation that is competent to properly associate with other septins once those molecules are synthesized. When those chaperones were mutated, excess Cdc12 persisted in cells but was unable to incorporate into septin filaments (Hassell *et al.*, 2022). Notably, this model of chaperone-guided septin hetero-octamer assembly focused on the septin GTPase domain and ignored the CTD, in part because the yeast septin Cdc10 lacks a CTD but displays similar chaperone interactions to Cdc12 and the other CTD-containing septins (Johnson *et al.*, 2015; Denney *et al.*, 2021). Thus it was unknown if chaperones also engage otherwise unoccupied septin hetero-oligomerization interfaces within the CTDs to promote efficient biogenesis of functional septin complexes.

One abundant cytosolic chaperone in budding yeast, Hsp104, displayed septin interactions that were unique compared to other chaperones. Hsp104 forms a homohexamer that is capable of disassembling protein oligomers, including β aggregates, by threading substrate proteins through a central channel and thereby unfolding them (Shorter and Southworth, 2019). We previously reported that Hsp104 binds all budding yeast septins and shows evidence of increased binding to G-interface mutant septins (Johnson *et al.*, 2015; Denney *et al.*, 2021). Intriguingly, overexpression of a double-mutant Hsp104 (G217S T499I) causes lethality in wild-type yeast cells in a manner that mimics septin dysfunction: cells become highly elongated and fail in cytokinesis (Hartwell, 1971; Schirmer *et al.*, 2004). Either of two spontaneous single missense mutations in the Cdc12 CTD is sufficient to confer resistance to the lethality of Hsp104(G217S T499I) (Schirmer *et al.*, 2004). These observations suggested that wild-type Hsp104 may normally bind the wild-type Cdc12 CTD without adverse effect on Cdc12 function, whereas the G217S T499I mutations unleash Hsp104 unfolding activity upon Cdc12, preventing septin hetero-octamer and filament assembly. The Cdc12 mutations might confer resistance by inhibiting Hsp104(G217S T499I) binding. However, these speculations had not been tested.

Here we investigated homo-oligomerization of the Cdc12 CTD and the contexts in which it might be physiologically relevant. Substitutions in a residue in the Cdc12 CTD, E368, altered both homo-oligomerization and the effects of Hsp104(G217S T499I), leading us to further explore the relationship between Cdc12 oligomerization and Hsp104.

RESULTS

Coiled-coil-mediated homo-oligomerization of the Cdc12 C-terminal domain

Previous studies provided evidence of CTD-mediated Cdc12 homo-oligomerization. In a yeast two-hybrid assay of septin-septin interactions (which may be complicated by interactions with endogenous septins), Cdc12–Cdc12 interaction generated the strongest signal and required the CTD (Farkasovsky *et al.*, 2005). Purified full-length Cdc12 was almost exclusively a homodimer when analyzed by size exclusion chromatography (SEC) (Hassell *et al.*, 2022). The Cdc12 CTD (residues 339-407) fused to GST binds full-length Cdc12 in vitro, demonstrating that the CTD sequence alone is capable of mediating Cdc12 homo-oligomerization (Versele *et al.*, 2004), and analysis of a small part of the Cdc12 CTD (residues 368-407) revealed evidence of homo-oligomeric coiled coils that could also weakly hetero-dimerize with the Cdc3 CTD (Barth *et al.*, 2008). We analyzed the purified Cdc12 CTD by SEC-multi-angle light scattering (SEC-MALS) and found evidence of coiled-coil-mediated Cdc12 homodimerization and, unexpectedly, homotrimerization (Fig. 1D). The Cdc12 CTD was either fused to a short residual N-terminal sequence (GSHM, in single-letter amino acid code) following cleavage with thrombin from a larger hexahistidine (H_6) fusion, or fused at its N terminus to a H_6 tag and *E. coli* maltose-binding protein (MBP). GSHM fused to Cdc12 residues 316-407 or 341-407 generated a

slightly asymmetrical peak with predicted molecular mass 2.6 times that of the monomer (Fig. 1D). We interpret these signals as a mix of homodimers and homotrimers undergoing rapid exchange relative to the light-scattering timescale. The indistinguishable behavior of the two constructs shows that the unstructured tail in the CTD (residues 316-340) does not contribute to the oligomeric equilibrium. We also directly detected a homotrimeric species when we crosslinked the shorter construct with BS3 and resolved the products by tricine-SDS-PAGE (Fig. 1E).

We used AlphaFold3 (Abramson *et al.*, 2024) to predict the structure of the Cdc12 CTD homotrimer at higher resolution. The result was a parallel trimer with high-quality metrics (high average pLDDT for the coiled coil region (77.3) and low interchain pAEs, Fig. S1A). Including the residual GSHM residues and/or removing residues 316-340 did not affect the outcome (Fig.1F, Fig.S1B). To determine the coiled-coil orientation in solution, we employed SEC coupled with small angle X-ray scattering (SAXS) using N-terminal MBP-fused constructs to add mass to one end of each helix. All relevant information regarding the SEC-SAXS data analysis is presented in Table S1. We analyzed two distinct constructs that differed in the number of residues between the coiled-coil forming sequences and MBP: "MBP-Cdc12CC" has a three-residue linker (SGS) before Cdc12 residue 340, whereas in "MBP-Cdc12CC+8" the Cdc12 residues following the SGS linker begin at Cdc12 residue 332. Initially, frames corresponding to the top of the SEC elution peaks were analysed. Dimensionless Kratky plots indicate folded complexes (Figs. S2,S3). All values for MBP-Cdc12CC+8 were consistent with a mix of dimers and trimers, as with the isolated Cdc12 sequences. MBP-Cdc12CC, on the other hand, behaved as a relatively pure homodimer. We suspect that the shorter linker between the MBP and Cdc12 sequences in this construct led to interactions between the MBP portions that prevented trimerization.

Atomistic modelling of MBP-Cdc12CC data with MultiFoXs (Schneidman-Duhovny *et al.*, 2016) using flexible linkers agreed with a parallel dimeric assembly (χ^2 = 1.41, CorMap *P*-value = 0.051). The data for MBP-Cdc12CC+8 could not be fitted well with either a single parallel dimer (di-p, χ^2 = 2.17, CorMap *P*-value = 0.000) or a single parallel trimer (tri-p, χ^2 = 7.91, CorMap *P*-value = 0.000). We then employed EOM-NNLSJOE (Bernadó *et al.*, 2007; Tria *et al.*, 2015) to analyse the MBP-Cdc12CC+8 dataset considering a mixture of parallel dimers and trimers. Antiparallel assemblies were not considered for the fit given the incompatibility between their calculated R_g's and the experimental $P(r)$-derived R_g (Fig. S4). RANCH was used to build 10,000 linker-flexible models, equally divided between parallel dimers and trimers (5,000 models each). EOM-NNLSJOE identified an ensemble in agreement with the experimental data (χ^2 = 1.07, CorMap *P*-value = 0.203), in which 66.0% of the models are parallel trimers and 34.0% are parallel dimers.

An additional analysis was conducted on two parts of the MBP-Cdc12CC+8 elution peak, selecting groups of contiguous frames in which trimers (peak front) and dimers (peak tail) were likely enriched (Fig. S5). Indeed, the calculation of mass, D_{max} and Porod volume using these two datasets was consistent with this assumption. The $P(r)$ function of the peak tail dataset resembled that obtained for MBP-Cdc12CC. Real space R_g's from the peak front and the peak tail datasets matched well with the mean/median of tri-p and di-p models generated by RANCH, respectively (Fig. S4). Atomistic model fitting with a single-state parallel dimer using MultiFoXs yields appropriate χ^2 for both reduced regions (χ^2 = 1.28 and 1.20 for peak front and peak tail datasets, respectively) although with CorMap *P*-values (0.0057 and 0.0053, respectively) insufficient to assure similitude between experimental and calculated data. MultiFoXs analysis using a single-state parallel trimer generates inadequate fit for both regions. This might indicate that MBP-Cdc12CC+8 is flexible enough to prevent a good fit of its SAXS data using a single oligomer and conformer. Fit of the MBP-Cdc12CC+8 peak front dataset with EOM-NNLSJOE using parallel dimers and trimers results in a good fit with an ensemble composed of a majority of trimers (χ^2 = 1.01, CorMap *P*-value = 0.940; 53.4% tri-p, 46.6% di-p). For MBP-Cdc12CC+8 peak tail dataset, parallel dimers and trimers also fit the data well, with only a small fraction of trimers (χ^2 = 0.97, CorMap *P*-value = 0.310; 93.0% di-p, 7.0% tri-p). This confirmed our initial conjecture that MBP-Cdc12CC+8 exists as a mixture of dimers and trimers (Fig. 1G). Together, these observations are consistent with an intrinsic ability of the Cdc12 CTD to form two kinds of homomeric parallel coiled coils in solution: homodimers and homotrimers.

Mutations in a conserved motif alter Cdc12 homo-oligomerization in vitro

Previous studies identified a sequence motif enriched in homotrimeric coiled coils, RhxxhE, wherein "h" denotes a hydrophobic residue and "x" is any residue (Kammerer *et al.*, 2005). A perfect match to this motif is found in the middle of the Cdc12 CTD (RFRQWE), representing the most highly conserved stretch of CTD residues (Fig.1B). W367 is conserved in most Cdc12 homologs and its presence in the core of the predicted homotrimer stands out, interacting hydrophobically with the two other Trp from other chains and also with F364. In the prediction, W367 and E368 side chains from different helices are in close proximity (Fig. 2A), and residues within the core pack against each other with acute angles, as expected for coiled-coil trimers. The coiled-coil radius reaches its maximum value of ~7.7 Å near the RhxxhE motif, likely to accommodate bulky side-chain residues (F364 and W367) in the core, and gradually decreases to a typical value (~6.0 Å) towards the C-terminus. The enlarged Cdc12 coiled-coil radius, which creates cavities in the region between F353 and W367, likely underlies its metastability.

We identified a single substitution in the homotrimerization motif, E368V, that drives the normal CTD homodimer:homotrimer equilibrium to homotrimers exclusively (Fig.2B). The E368V homotrimers were

exceedingly thermostable (Fig.2C, Table S2). In the AlphaFold model, the side chain of E368 projects slightly away from the hydrophobic core of the trimer that includes W367 and F354 (Fig.2A); burial of the hydrophobic valine side chain in this hydrophobic core likely confers the high stability of the E368V homotrimer. Consistent with the prediction, nano differential scanning fluorimetry experiments indicated that W367 is more buried when E368 is replaced by valine (Fig.2D). Replacing E368 with lysine (E368K), a residue found in this position in the Cdc12 homolog from the yeast *Ogataea parapolymorpha*, should alter the contact with W367 without disturbing the hydrophobic core, and indeed this mutation maintained helical character while shifting the equilibrium to homodimers (Fig.2E, Table S4). Disturbing the hydrophobic core by replacing W367 with hydrophilic lysine (W367K) ablated oligomerization and reduced helical character (Tables S2-4), whereas substitution to another hydrophobic residue, leucine, did not (Fig.2F). These results support a model in which the CTD of Cdc12 mediates metastable coiled-coil homo-oligomerization via a previously unrecognized, highly conserved motif, mutations in which can drive homotrimerization or block homo-oligomerization altogether.

Evidence for Cdc12 homo-oligomerization in vivo

In the top-ranked AlphaFold3 prediction for a full-length Cdc12 trimer, homotrimerization was mediated by the same three-helix coiled coil predicted by our in silico and in vitro experiments with the isolated CTDs (Fig. 3A). [We note that in this trimeric context the globular Cdc12 GTPase domains did not interact with each other. By contrast, in all five predictions for a full-length Cdc12 homodimer, the globular GTPase domains interacted via the canonical septin G or NC interface (Fig. S6), even though such Cdc12–Cdc12 interfaces are not found in the native septin hetero-octamer (Fig.1A).] We took two approaches to ask if such Cdc12 homo-oligomers occur in living cells. First, we used the *GAL1/10* promoter and culture medium containing 2% galactose to drive overexpression of C-terminally GFP-tagged Cdc12, lysed cells, separated clarified lysates by SEC, and used an anti-GFP antibody to detect relative Cdc12-GFP levels in fractions corresponding to expected sizes of hetero-octamers, homotrimers, and homodimers. GFP-tagged wild-type Cdc12 was found in three obvious peaks: mostly in the hetero-octamer fraction (expected ~400 kDa, observed 334-391 kDa), less in a homotrimer-sized fraction (expected ~210 kDa, observed 208-244 kDa) and even less in a homodimer-sized fraction (expected ~144 kDa, observed 130-152 kDa) (Fig.3B). As we observed in vitro with purified Cdc12 CTD, the relative abundance of apparent homotrimers increased, and homodimers decreased, upon introduction of the E368V mutation (Fig.3B). Due to its severe effects on cell proliferation (see below), we did not assess the W367K mutant in the same way. While they do not address the presence or absence of other proteins in complex with the overexpressed Cdc12-GFP, these data are consistent with the accumulation of excess molecules of Cdc12 in CTD-mediated homodimers and -trimers in vivo.

As a second approach to detect Cdc12 homo-oligomerization in vivo, we adapted a tripartite split-GFP system (here referred to as trimolecular fluorescence complementation, or TriFC) previously used to detect dimeric septin-septin interactions in yeast (Finnigan *et al.*, 2016). [We (Garcia *et al.*, 2016; Weems and McMurray, 2017; Benson and McMurray, 2023) and others (Kang *et al.*, 2024) have also used a bipartite BiFC approach to detect septin-septin interactions in yeast, but we reasoned that any Cdc12–Cdc12 BiFC signal could result from antiparallel CTD interactions in the context of pairing of adjacent septin filaments (Fig. 1A), rather than CTD-mediated homodimerization per se.] In the TriFC system, the 11-stranded GFP β barrel is split into three fragments corresponding to β strands 1-9, 10, and 11 (Cabantous *et al.*, 2013) (Fig.3C). We looked for fluorescence in cells co-expressing three Cdc12 fusion proteins with the GFP fragments plus untagged endogenous Cdc12. To favor the coiled-coil interaction as a driver of TriFC, we included in the Cdc12-GFP(β11) fusion the G-interface mutation W267A, known to weaken non-native Cdc12–Cdc12 G interface interactions (McMurray *et al.*, 2011). Indeed, in all five AlphaFold3 predictions for the complex formed by the three fusions, the GFP was reconstituted at the tip of the same three-helix coiled coil supported by our other experiments, and while all models included at least one interaction between GTPase domains, the Cdc12(W267A)-GFP(β11) G interface was never engaged (Fig. 3C, Fig. S8A).

Cdc12-GFP(β1-9) was expressed from the *GAL1/10* promoter; we used low galactose concentrations (brought to 2% final sugar with raffinose) to better match the levels of the other two fusions, which were expressed from the *CDC12* promoter. We detected TriFC signal only in 2% raffinose (no galactose), where *GAL1/10* transcription is neither repressed nor induced (Johnston *et al.*, 1994), and in only 13 of 3,098 cells (0.4%, see Fig.3D for representative images). Given four distinct versions of Cdc12 expressed in these cells (untagged, β1-9, β10, and β11), if expression levels were perfectly equivalent, at most 9.375% of Cdc12 trimers would be comprised of the three distinct TriFC fusions and thus capable of generating fluorescence. Furthermore, all three fusion proteins were expressed from distinct plasmids, which may vary in copy number per cell, and expression of each individual gene may be "bursty". Hence the rarity of TriFC signal was not surprising. Crucially, introducing the W367K mutation that blocks homo-oligomerization in vitro into the Cdc12-GFP(β1-9) fusion eliminated TriFC signal: no signal was observed in 3,169 cells analyzed. As we demonstrate in multiple ways (see below), Cdc12(W367K) incorporates efficiently into septin hetero-octamers and filaments, hence the loss of TriFC signal with this mutation provides strong evidence that TriFC signal with wild-type Cdc12 represents coiled-coil homo-oligomerization by excess Cdc12 molecules occurring prior to hetero-octamer assembly.

The lack of fluorescence in cultures with galactose is readily explained by an excess of Cdc12-GFP(β1-9) forming non-fluorescent homotrimers. In these cultures cell morphology was abnormal and worsened with

increasing galactose concentrations (Fig. 3E), indicative of dominant perturbation of septin function by Cdc12-GFP(β1-9). Such dominant perturbation is a common effect of overexpressing septins fused to certain large tags and is evidence that the tagged septin displaces untagged septins in hetero-octamers and perturbs filament polymerization and/or function (McMurray, 2016). The same or worse galactose-dependent morphological defects were observed with Cdc12(W367K)-GFP(β1-9) (Fig.3E), confirming that the mutant protein was expressed at equivalent levels to wild type Cdc12-GFP(β1-9). Interestingly, cells fell into only two categories with regard to TriFC signal: no fluorescence, or bright fluorescence, the latter being either at cortical current/former sites of budding (where rings of septin filaments are normally found (Haarer and Pringle, 1987; Ong *et al.*, 2014)) or in long "fibers" (Fig.3D), which have also been previously reported for C-terminal Cdc12 fusions (McMurray, 2016). We suspect that in the rare cells in which the expression of the three Cdc12 fusions achieves the 1:1:1 balance that supports Cdc12 TriFC, many fluorescent trimers are produced, leading to bright signals. Coiled coil metastability allows one of the Cdc12 fusions to disengage from the homotrimeric coiled coil and engage with the CTD of Cdc3 in the context of a septin hetero-octamer, without dissociating the reconstituted GFP. Indeed, this very scenario was represented in the highest-ranked AlphaFold3 prediction when we included Cdc3, Cdc10, and Cdc11 with the three Cdc12 fusions (Fig.S8B). Incorporation of one Cdc12 fusion into septin filaments recruits to the bud neck the other two Cdc12 fusions still linked via the TriFC event, analogous to the bud neck signals we previously observed by BiFC for septin interactions with cytosolic chaperones (Denney *et al.*, 2021). These data are thus consistent with a model in which CTD-mediated homodimers and homotrimers are transient species formed by superstoichiometric molecules of Cdc12 en route toward hetero-octamer and filament assembly once partner septins become available.

We wondered if the increased homotrimer stability induced by the E368V mutation might "lock" the CTDs of excess Cdc12 subunits into permanent homotrimers that would be unable to incorporate into septin hetero-oligomers. However, excess molecules of Cdc12(E368V)-GFP showed no defect in post-translational filament assembly (Fig.S9), suggesting that even the E368V-mutant Cdc12 homo-oligomers are sufficiently metastable to eventually hetero-oligomerize.

Cdc12 C-terminal domain homo-oligomerization mutants exert potent dominant-negative effects on septin filament function

To further study potential roles for Cdc12 CTD-mediated homo-oligomerization in septin hetero-oligomerization and function in vivo, we overexpressed GFP-tagged Cdc12 or W367K or E368V mutants thereof in haploid cells co-expressing wild-type, untagged Cdc12 and mCherry-tagged Cdc3 from the respective genomic loci. We compared colony growth, cell morphology, and septin localization of cells cultured in galactose-containing medium to control conditions with 2% glucose, which represses *GAL1/10* promoter

activity. Surprisingly, wild-type Cdc12-GFP overexpression slightly reduced colony growth (Fig. S10A), and cells were frequently elongated and displayed mislocalization of mCherry-Cdc3, a phenotype that was not previously observed using this same Cdc12-GFP plasmid in cells of the same strain background but lacking any tag on Cdc3 (Versele *et al.*, 2004; Benson and McMurray, 2023). The mCherry-Cdc3 fusion we used has also never before been reported to itself cause septin dysfunction (Gao *et al.*, 2007; McMurray, 2016). We suspected that, since Cdc3 and Cdc12 directly interact via an interface involving residues near their N and C termini (Fig.1A), the defects we observed represent a "synthetic" effect of the C-terminal GFP tag on Cdc12 combined with the mCherry tag inserted near the N terminus of Cdc3.

To address this concern, we repeated these experiments in yeast cells with no tag on any other septin except the GFP tag on the overexpressed Cdc12 (the same set-up used in the SEC experiments above). Here, only the mutant versions of Cdc12-GFP had any detectable effect on colony growth and cell morphology, and these effects were equivalent to those seen in the strain with tagged Cdc3 (Fig. 4A and Fig. S10A). Thus, the effects of CTD mutations in Cdc12 were not a consequence of Cdc3 dysfunction caused by the mCherry tag. Whereas the E368V mutant had no obvious effect, the W367K mutant was nearly lethal upon overexpression, causing drastic morphology and cytokinesis defects (and mCherry-Cdc3 mislocalization; Fig. 4 and S10A,B). We also tested a W367K E368V double mutant construct, which caused defects but not as severe as W367K alone (Fig. S10A,B). SEC results suggested that Cdc12(W367K E368V) molecules accumulate as homodimers in vivo and in vitro (Fig.3B, Fig. S10C); the homodimer-destabilizing effect of the hydrophilic lysine at position 367 is likely counteracted by the hydrophobic valine at position 368.

We also included a truncated version of Cdc12-GFP lacking the CTD (residues 339-407 deleted), which was already known to be dominant lethal when overexpressed (Johnson *et al.*, 2015). The W367K mutant was nearly as potently lethal as the ΔCTD mutant (Fig.4A). We interpret the ability of the Cdc12 mutants to interfere with septin function despite the presence of wild-type Cdc12 as evidence that the mutant proteins co-assemble with wild-type septins into dysfunctional complexes/filaments.

When we determined the sequence of the mutant Cdc12-GFP plasmids to confirm the presence of the mutations, we discovered another mutation already present in the "wild-type" Cdc12-GFP parent plasmid, encoding the substitution N379D. N379 is highly conserved and makes a predicted contact in the Cdc12 CTD homotrimer but not the Cdc3–Cdc12 heterodimer (Fig.1B). However, restoring N379 in the W367K plasmid did not alter its ability to dominantly perturb septin function (Fig. S11). Thus we consider the N379D mutation to be phenotypically neutral with regard to the experiments in this study.

Mutating the Cdc12 CTD homotrimerization motif mimics the effects of CTD truncations on cellular septin functions

According to our model, Cdc12(W367K) dominantly perturbs septin function not because excess Cdc12 monomers are unable to homo-oligomerize, but because Cdc12(W367K) monomers are able to co-assemble with other septins into hetero-octamers, and the filaments made from these octamers are ultimately dysfunctional. Since W367 is located in the CTD, it might perturb septin function in a way similar to other CTD mutations, many of which cause phenotypes that are modified by temperature. For example, truncation of residues 392-407 (associated with the *cdc12-6* allele) is tolerated at 22˚C but is lethal at ≥30˚C (Adams and Pringle, 1984; Johnson *et al.*, 2015). [Like the W367K mutant, the Δ392-407 truncation blocked homo-oligomerization by purified Cdc12 CTD (Table S4)]. We asked if the septin dysfunction caused by Cdc12(W367K) overexpression is also modified by temperature. Indeed, cultivation at 37˚C exacerbated, and cultivation at 22˚C ameliorated, the adverse overexpression effects of Cdc12(W367K), as well as the effects of the other CTD mutants, including Cdc12ΔCTD (Fig.5A). Thus Cdc12(W367K) overexpression phenocopies the effects of other CTD mutations on septin function.

Deletion of the *RTS1* gene allows *cdc12-6* cells to proliferate at 30˚C (Dobbelaere *et al.*, 2003). *RTS1* encodes a phosphatase that drives destabilization of septin filaments and higher-order structural transitions during the yeast cell division cycle (Dobbelaere *et al.*, 2003). If Cdc12(W367K) overexpression perturbs septin function by populating hetero-octamers with CTD-defective subunits, then *rts1*Δ might also confer the ability to proliferate at 30˚C despite Cdc12(W367K) overexpression. Indeed, *rts1*Δ cells overexpressing Cdc12(W367K)-GFP were able to form colonies almost as well as cells overexpressing wild-type Cdc12-GFP, and showed only subtle morphological defects (Fig.5B). Furthermore, in *rts1*Δ cells Cdc12(W367K)-GFP localized strongly to septin rings at bud necks (Fig.5B). These findings support the conclusion that the W367K mutation does not perturb septin hetero-octamer assembly per se but the resulting octamers are defective in Cdc12 CTD function in a manner that resembles dysfunction associated with loss/truncation of the CTD. Moreover, septin filaments populated with Cdc12(W367K) subunits are severely dysfunctional only in the presence of Rts1; otherwise, they function almost normally.

Substitutions of Cdc12 CTD residue E368 confer resistance to the lethal effect of Hsp104(G217S T499I)

Either of two single missense mutations in Cdc12 confers resistance to the lethality caused by overexpression of Hsp104(G217S T499I) (Schirmer *et al.*, 2004). One of these mutations, E368Q, alters a residue we implicated in homotrimerization. We used AlphaFold3 to predict where the substrate-binding domain of Hsp104 (residues 1-152) binds Cdc12. First, as a control, we generated predictions of Hsp104 binding to residues 96-151 of a known Hsp104 substrate, the prion-forming protein Sup35 (Sweeny *et al.*, 2015). Satisfyingly, all five

predictions showed Hsp104 binding to precisely the region of Sup35 found recently by others using purified proteins (Shen *et al.*, 2024) (Figs. 6A and S12A).

Next, we generated predictions for Hsp104 binding to Cdc12, either the CTD alone (residues 297-407) or full-length Cdc12. In both cases, in the highest-confidence predictions Hsp104 contacts Cdc12 via residues that lie within the hydrophobic groove between helix 1 and helix 4 and overlap with residues that contact Sup35 and other known Hsp104 substrates (Harari *et al.*, 2022) (Fig.6A). Hsp104 binding to the Cdc12 CTD centered around Cdc12 E368, and the side chain of Cdc12 E368 made predicted contact with Hsp104 Q19 (Fig.6A). When we used full-length Cdc12, Hsp104 binding centered around K351, with additional residues outside the Hsp104 hydrophobic groove contacting the globular GTPase domain of Cdc12 (Fig.6A). K351N is the other mutation that confers Hsp104(G217S T499I) resistance (Schirmer *et al.*, 2004).

When we superimposed the Hsp104 homohexamer structure (PDB 6N8T) on the prediction for the Hsp104 substrate-binding domain bound to the Cdc12 CTD, the Cdc12 CTD projected directly into the central pore (Fig.6A). These predictions support a model in which Hsp104(G217S T499I) binds the Cdc12 CTD in two locations that are primed for threading and Cdc12 unfolding. Hsp104 threading can disassemble otherwise irreversible amyloid-type aggregates formed from β-sheet-like intermolecular interactions (Shorter and Lindquist, 2004). We previously noted that a sequence-based algorithm predicts high β-aggregation potential for the β4 strand in the septin GTPase domain that is ultimately buried in the septin-septin G interface, and we directly crosslinked chaperones to the Cdc10 β4 strand in vivo (Hassell *et al.*, 2022). Indeed, in all AlphaFold3 predictions, the Hsp104 substrate-binding domain bound the aggregation-prone β4 peptides from Cdc10 and Cdc12 via the same interface as it binds Sup35 (Fig. S12B). Whereas the Cdc12 CTD is predicted to be natively helical, the WALTZ algorithm (Maurer-Stroh *et al.*, 2010) predicted residues 367-375 as the only non-β4 region with β-aggregation potential (Fig. 6B). These findings are consistent with a model in which Hsp104 binds aggregation-prone regions in septin proteins, which includes a part of the Cdc12 CTD also involved in homo-oligomerization.

Notably, when wild-type Hsp104 takes apart β aggregates of Sup35, it does not unfold all of Sup35. Instead, Hsp104 threads only the Sup35 N-terminal tail, and leaves the C-terminal GTPase domain intact (Sweeny *et al.*, 2015). This partial substrate processing behavior of Hsp104 has also been observed with other substrates (Haslberger *et al.*, 2008). Thus our unbiased in silico predictions provide strong support for a model in which — due to two misfolding/aggregation-prone regions, one in the GTPase domain and one in the CTD — the Cdc12 CTD is a native substrate for folding assistance and/or aggregation reversal by wild-type Hsp104, and these events need not unfold the Cdc12 GTPase domain. The G217S T499I mutations in Hsp104 hyperactivate

unfoldase activity, driving complete unfolding of the Cdc12 and resulting in defective septin filament assembly and cytokinesis failure. In this model, the E368Q mutation in Cdc12 prevents Hsp104(G217S T499I) binding to the CTD, which is frequently exposed due to coiled-coil metastability; the aggregation-prone region in the GTPase domain would be buried in the Cdc12–Cdc11 G interface and consequently hidden from Hsp104(G217S T499I).

One prediction of this model is that the E368V substitution should, like E368Q, confer protection from Hsp104(G217S T499I) overexpression. We co-overexpressed in the same cells Hsp104(G217S T499I) and Cdc12-GFP or CTD mutants thereof and assessed colony growth via dilution series. Consistent with the prediction, overexpression of the Cdc12(E368V) allowed colony growth by cells also overexpressing Hsp104(G217S T499I) (Fig. 6C). Morphology of cells from these colonies and bud neck localization of Cdc12-GFP therein correlated with colony growth (Fig. S13A). Overexpression of wild-type Hsp104 had no obvious effect on colony growth, cell morphology, or Cdc12-GFP localization (Fig. 6C and Fig. S13A).

These results support a model in which Hsp104 binds the Cdc12 CTD unless a CTD mutation (E368V) that promotes homotrimerization is present. We imagined two ways this could work: the mutation could directly eliminate a critical contact between Hsp104 and Cdc12, or the mutation could drive homotrimerization, which buries the residue(s) otherwise involved in Hsp104–Cdc12 contact. To distinguish between these two models, we asked if the E368Q mutation also promotes CTD homotrimerization in vitro. Unlike E368V, and instead like the wild type, purified Cdc12(E368Q) CTD formed a mix of homodimers and trimers (Table S4). Thus we favor the interpretation that mutations at E368 confer resistance to overexpression of Hsp104(G217S T499I) due to loss of direct contact between Hsp104 and E368, not as a result of burial of Hsp104–Cdc12 contacts specifically in a coiled-coil homotrimer.

Hsp104 potentiates the dominant-negative effects of homo-oligomerization-defective Cdc12(W367K) on septin assembly by protecting CTD-mutant Cdc12 against proteasomal degradation

The findings above suggest that Hsp104 binds the Cdc12 CTD and that mutations affecting CTD-mediated Cdc12 homo-oligomerization also affect interaction with Hsp104. We therefore asked if deleting *HSP104* alters the phenotypic consequences of overexpressing CTD-mutant versions of Cdc12. Strikingly, the absence of Hsp104 completely eliminated the functional defects associated with overexpression of Cdc12(W367K)-GFP but had no effect on the phenotypes associated with overexpression of Cdc12(W367K E368V)-GFP (Fig. 4B,C). The amelioration of Cdc12(W367K)-induced septin dysfunction in *hsp104*Δ cells was accompanied by a drastic decrease in the cellular levels of Cdc12(W367K)-GFP (Fig. 4C). By contrast, wild-type Cdc12-GFP was unaffected by deletion of *HSP104* (Fig. 4C). The simplest explanation for the amelioration of septin dysfunction

is that the absence of Hsp104 specifically prevented high-level accumulation of Cdc12(W367K)-GFP, and therefore that Hsp104 is required for such accumulation.

Hsp104 could promote high-level accumulation of Cdc12(W367K) by preventing degradation of monomeric Cdc12. According to this model, the effects of Cdc12(W367K E368V) overexpression are unchanged by *hsp104*Δ because the E368V mutation restores Cdc12 homo-oligomerization, not because the E368V mutation prevents Hsp104 interaction with the Cdc12 CTD. To learn more about how changes to the Cdc12 CTD influence the dependency on Hsp104, we tested the effect of *hsp104*Δ on overexpression of Cdc12ΔCTD-GFP. As with Cdc12(W367K)-GFP, cells lacking Hsp104 were entirely unaffected by the presence of the Cdc12ΔCTD-GFP-encoding plasmid (Fig. 4B). Notably, faint Cdc12(W367K)-GFP signals could be detected in septin rings at the bud necks of *hsp104*Δ cells (Fig. 4C), indicating that low levels of incorporation of the mutant proteins into septin rods and filaments are tolerated from a functional perspective. Presumably, the presence of wild-type (untagged) Cdc12 in at least some threshold number of rods/filaments is sufficient for function.

Human Septin-5 is degraded by the proteasome (Zhang *et al.*, 2000). To ask if the proteasome is responsible for the lack of high-level accumulation of Cdc12(W367K) in *hsp104*Δ cells, we combined *hsp104*Δ with a hypomorphic allele of a proteasome subunit, *pre1(S142F)*, which reduces the proteolytic activity of the proteasome (Heinemeyer *et al.*, 1991; Seufert and Jentsch, 1992)). In these cells, overexpressed Cdc12(W367K)-GFP accumulated to sufficiently high levels to perturb septin function (Fig. 7), representing a restoration of the behavior observed in *HSP104*$^{+}$ cells. We conclude from these data that Hsp104 protects excess Cdc12 monomers from proteasomal degradation. In the absence of Hsp104, the excess mutant Cdc12 molecules stabilized by the proteasome mutation must not all be irreversibly misfolded or aggregated — at least in the conditions tested here — because at least some are apparently competent to interact with other septins and dominantly perturb septin function.

Hsp104 co-localization and co-elution with Cdc12 CTD mutants

For Hsp104 substrates that form visible foci in cells, Hsp104 co-localizes with those foci (Lum *et al.*, 2004). We previously showed that the same construct we used here for overexpressing Cdc12-GFP (but not other constructs with different Cdc12 fusions) leads to the formation of foci in a subset of cells, and these foci rarely co-localize with mCherry-tagged Hsp104 (Hassell *et al.*, 2022). We exploited the focus formation by GFP-tagged Cdc12 to test our model that Hsp104 stabilizes monomeric Cdc12 via direct binding. Whereas most cells overexpressing Cdc12(W367K)-GFP become grossly misshapen, a subset of cells have relatively normal morphology, allowing us to compare Hsp104-mCherry–Cdc12-GFP co-localization between cells

overexpressing wild-type Cdc12-GFP and cells overexpressing Cdc12(W367K)-GFP. The W367K mutation had no effect on the frequency of Cdc12-GFP foci but caused a >20-fold increase in the co-localization of Cdc12-GFP and Hsp104-mCherry in foci: among 340 cells expressing wild-type Cdc12-GFP, there were 183 GFP foci and 139 mCherry foci, of which only 2 overlapped (0.6%), whereas among 197 cells expressing Cdc12(W367K)-GFP, there were 113 GFP foci and 107 mCherry foci, of which 27 overlapped (13.7%; see Fig. 8A for representative images). Increased co-localization of Cdc12(W367K)-GFP with Hsp104 is consistent with Hsp104 binding to Cdc12 molecules that are not engaged in CTD-mediated homo-oligomerization. Note that the foci formed by GFP-tagged Cdc12 in these experiments are an artifact of the GFP tag and should not be taken as evidence of Cdc12 aggregation per se; instead, they conveniently concentrated Cdc12-GFP signal in a way that allowed us to detect co-localization with Hsp104.

We found independent evidence of Hsp104 association with monomeric Cdc12 in SEC experiments with yeast lysates in which we exploited the exclusionary effect of the G268R mutation in the Cdc12 G interface (Johnson *et al.*, 2015) to overcome the lethality of Cdc12(W367K) overexpression (Fig.8B). In contrast to the dominant-negative behavior of CTD mutants, mutant septins harboring substitutions in the G interface are rendered innocuous via prolonged G interface binding to cytosolic chaperones and exclusion from septin hetero-octamers (Johnson *et al.*, 2015; Hassell *et al.*, 2022). Rather than eluting as monomers, overexpressed Cdc12(G268R W367K)-GFP eluted in fractions with a peak corresponding to ~700-kDa (Fig.8C). This peak matches the expected size of an Hsp104 hexamer bound to Cdc12(G268R W367K)-GFP (694 kDa) and, when we exposed the blot to an anti-Hsp104 antibody, overlapped with a "shoulder" on the peak of Hsp104 elution (Fig. 8C). The ~627-kDa fraction with the peak of Hsp104 matches the size of Hsp104 hexamers without bound substrate (624 kDa). Together with the co-localization of Hsp104-mCherry and excess Cdc12(W367K)-GFP, these findings strongly support a model in which hexameric Hsp104 binds and sequesters excess Cdc12 monomers.

Hsp104 is required to maintain super-stoichiometric expression of septins that cannot undergo CTD-mediated homo-oligomerization

Despite lacking a CTD (Fig.1A), Cdc10 can homo-oligomerize: purified Cdc10-6xHis binds purified GST-Cdc10 in vitro (Versele *et al.*, 2004), Cdc10 expressed individually in *E. coli* purifies as apparent homo-oligomers (Baur *et al.*, 2019), and available in vivo evidence suggests Cdc10 homodimerizes prior to Cdc10–Cdc3 interaction during octamer assembly (Weems and McMurray, 2017). If a septin CTD is required for Hsp104 independence, then the absence of Hsp104 should prevent high-level accumulation of Cdc10. Alternatively, if homodimerization per se is sufficient to stabilize an excess septin against degradation despite the absence of Hsp104, then excess Cdc10 should not require Hsp104 for stability. In support of the first hypothesis, Cdc10-GFP overexpressed using the *MET25* promoter accumulated to high levels in wild-type cells

but not in *hsp104*Δ cells, where only faint bud neck signals were detected (Fig. 9A). Furthermore, analogous to the effects of Cdc12ΔCTD overexpression, overexpression of Cdc10Δα0, a version of Cdc10 lacking a critical component of the homodimerization interface that allows hetero-octamers to assemble (McMurray *et al.*, 2011), was lethal to wild-type cells but *hsp104*Δ cells were completely unaffected (Fig. 9A). Thus homodimerization per se is not sufficient to stabilize an excess septin in the absence of Hsp104.

Conversely, while Cdc3 has a CTD (Fig.1A), the purified Cdc3 CTD does not homo-oligomerize at all (Fig.9B), and only a fraction of purified full-length Cdc3 homo-oligomerizes (Hassell *et al.*, 2022). By contrast, purified full-length Cdc11 is nearly 100% homodimers and this homodimerization requires the CTD (Brausemann *et al.*, 2016). If CTD-mediated homo-oligomerization, not just the presence of a CTD or homodimerization alone, is required to stabilize an excess septin in the absence of Hsp104, then excess Cdc3 molecules, but not excess Cdc11 molecules, should require Hsp104 for their stability. Indeed, compared to the fluorescence observed in wild-type cells overexpressing Cdc3-GFP from the *GAL1/10* promoter, signal in *hsp104*Δ cells was greatly reduced (Fig. 9C). By contrast, Hsp104 was not required for the accumulation of high levels of Cdc11 (or its paralog Shs1, which also has a CTD) or for the septin dysfunction known to result from overexpression of either of these septins (Sopko *et al.*, 2006) (Fig. 9D). Thus having a CTD with coiled-coil-forming potential is not enough to stabilize a septin: that CTD must also confer efficient homo-oligomerization.

The low levels of Cdc10-GFP and Cdc12(W367K)-GFP found at the bud neck upon attempted overexpression of those septins in *hsp104*Δ cells (Figs. 4C,9A) suggested that in the absence of Hsp104 the mutant septins are protected from degradation if they successfully incorporated into septin-hetero-oligomers or filaments. If protection from degradation reflects burial of otherwise exposed proteasome-targeting regions in septin-septin interfaces (e.g. the G interface), then we wondered if co-overexpressing two septins that interact via the G interface would bury these regions and provide protection. We recently showed that simultaneous co-overexpression of tagged versions of Cdc3 and Cdc10 — which interact via a G interface (Fig. 1A) — severely perturbs septin function, as evidenced by highly elongated cells (Benson and McMurray, 2023). Here we found that this functional perturbation also manifests as defects in colony formation at 30˚C (Fig. 9E). This effect was entirely lost in *hsp104*Δ cells and levels of both tagged Cdc3 and Cdc10 were greatly reduced (Fig. 9E), suggesting that the G interface partners could not protect each other.

When Cdc3 is specifically tagged with a fragment of the YFP derivative Venus ("V_C") and co-overexpressed with Cdc10 tagged with a BiFC-compatible Venus fragment ("V_N"), in addition to inducing cell elongation, the "excess" molecules of Cdc3-V_C and Cdc10-V_N co-assemble into stable, plasma-membrane-associated filaments composed only of tagged Cdc3 and Cdc10 (Benson and McMurray, 2023). Even in this scenario, the absence of

Hsp104 prevented both the high-level accumulation of BiFC fluorescence and the associated cell elongation and plasma membrane localization (Fig.S13B). Instead, only low levels of Cdc3–Cdc10 BiFC signal were detected at bud necks (Fig.S13B), similar to the situation with attempted overexpression of Cdc10-GFP alone. Unique among the five mitotic yeast septins, Cdc3 has a ~100-residue N-terminal domain (Fig. 1A) that we previously proposed may occlude the Cdc3 G interface and prevent Cdc3–Cdc10 interaction until Cdc3 interacts with Cdc12 (Weems and McMurray, 2017). We tried removing the Cdc3 NTD to improve Cdc3–Cdc10 G dimerization, but this mutation — which does not block the assembly of membrane-associated filaments upon Cdc3-V_C–Cdc10-V_N co-overexpression in wild-type cells (Benson and McMurray, 2023) — failed to restore the dominant perturbation of septin function or high-level accumulation of Cdc3–Cdc10 BiFC signal in *hsp104*Δ cells (Fig. S13B). Thus even the ability to polymerize into membrane-associated filaments does not protect "excess" Cdc10 from degradation when Hsp104 is absent.

Immunoblotting confirmed these findings: whereas steady-state overexpression levels of Cdc11-mCherry (~15-fold higher than endogenous/native levels) were unaffected by *HSP104* deletion, Cdc3-mCherry levels were reduced to an amount equivalent to endogenous/native levels (Fig. S14). Thus all available evidence supports the idea that CTD-mediated homo-oligomerization lifts the Hsp104 requirement for a septin to accumulate at superstoichiometric levels, and in the absence of Hsp104 only incorporation into native-like hetero-octamers is able to protect a CTD-less septin from degradation.

The number of septin-encoding mRNAs per cell is low and variable between cells and between different septins

Our findings reveal unappreciated roles for transient septin homo-oligomerization and the cellular proteostasis machinery in the ability of cells to maintain excess septin subunits. We discovered these roles via experimental, high-level overexpression of single septin subunits. What is the natural context in which these maintenance mechanisms may have evolved? We reasoned that if the endogenous septin genes are infrequently transcribed, this could create a scenario in which the number of septin-encoding mRNAs per cell fluctuates widely within a population of cells. Efficient translation of septin mRNAs (estimates range from five to 11 ribosomes per septin mRNA (Arava *et al.*, 2003)) would then generate transient imbalances in subunit stoichiometry within a given cell. Indeed, existing evidence from transcriptome-wide studies pointed to a low number of septin-encoding mRNAs per cell. For Cdc12, estimates ranged from 0.3 to 3.2 copies/cell, depending on the technique (Velculescu *et al.*, 1997; Holstege *et al.*, 1998; Miura *et al.*, 2008); other septin mRNAs were in a similar range (Cdc3 1.5-2.9 copies/cell; Cdc10 1.7-3.0; Cdc11 1-3.1 (Velculescu *et al.*, 1997; Holstege *et al.*, 1998; Miura *et al.*, 2008)).

These published values come from relatively indirect assays. To directly determine cell-to-cell variation in septin mRNA copy number, we used single-molecule inexpensive fluorescence in situ hybridization (smiFISH) (Tsanov *et al.*, 2016). We first validated our experimental approach by localizing in the same cells mRNAs encoding Ash1, which are specifically localized to the bud tip (Long *et al.*, 1997), and Abp140, which are specifically localized in the mother cell distal from the bud (Kilchert and Spang, 2011) (Fig. 10A). Next, using mutant cells missing or depleted for the target mRNA to control for non-specific background signal, we localized mRNAs encoding Cdc3 and/or Cdc10 and found that the number of septin mRNAs per cell was low and highly variable (Fig. 10B,D), in agreement with the indirect estimates. Importantly, Cdc3 and Cdc10 mRNA copy numbers per cell varied independently (Fig. 10D), providing many potential opportunities for stoichiometric imbalances.

DISCUSSION

Various factors dictate the fate of excess subunits of heteromeric protein complexes. A previous study used yeast strains with an extra copy of a single chromosome to generate a two-fold excess of individual subunits and found that 73% of proteins that function in complexes either aggregated or were degraded (Brennan *et al.*, 2019). Those authors proposed that "excess proteins that do not aggregate or get degraded are simply less aggregation-prone and lack the signals that target them for degradation" (Brennan *et al.*, 2019). While in this study Cdc3 and Cdc12 were among the 437 proteins found in "aggregates" (as defined by pelleting during centrifugation of lysates) (Brennan *et al.*, 2019), we have clearly shown here and elsewhere (Hassell *et al.*, 2022) that individual yeast septins expressed at high levels are not irreversibly aggregated. Thus despite being intrinsically aggregation-prone and possessing signals able to target them for degradation, excess yeast septins avoid these fates via a combination of assistance from chaperones and coiled-coil-mediated homo-oligomerization (Fig.10E).

Homo-oligomerization by septins that do not normally occupy two adjacent positions within a septin filament has previously been viewed as a vestige from the evolutionary past, potentially generating "off-pathway" homo-oligomers (Hassell *et al.*, 2022; Brown and McMurray, 2025) or, in some cases, alternative hetero-oligomers with distinct functions (hetero-hexamers vs hetero-octamers) (Johnson *et al.*, 2020). Roles in hetero-oligomer assembly for the conserved predicted coiled-coil-forming sequences in many septin CTDs have remained mostly enigmatic, particularly with regard to their metastable character. In the septin literature, CTDs mostly contribute to higher-order septin hetero-oligomer structure and function: how filaments interact with each other and with membranes and/or other proteins (Finnigan *et al.*, 2015a; Sala *et al.*, 2016; Cannon *et al.*, 2019; Leonardo *et al.*, 2021; Woods *et al.*, 2021; Castro *et al.*, 2023). There is no place for septin homotrimers in this view, which is why we were so intrigued by our observation of Cdc12 CTD homotrimerization in vitro and particularly the presence of a highly conserved homotrimerization motif. Indeed, to our knowledge the Cdc12 CTD is the first septin coiled coil to exhibit trimerization. Human SEPT1, SEPT2, SEPT4, SEPT5, SEPT6, SEPT7, SEPT8, SEPT14 and SmSEPT10 CTDs are all homodimers (Leonardo *et al.*, 2021; Cavini *et al.*, 2023, 2024).

While we found evidence of Cdc12 homotrimers in vivo, Cdc12 homodimers were also present and appear to function in the same way: together with Hsp104, they help protect excess Cdc12 molecules against degradation (Fig.10E). The Cdc12(W367K E368V) mutant was particularly informative: if E368 is required for Hsp104–Cdc12 binding, then Hsp104 should be incapable of stabilizing excess Cdc12(W367K E368V) molecules, yet Cdc12(W367K E368V)-GFP accumulated to high levels and dominantly interfered with septin function in the absence of Hsp104 (Fig. 4B). Thus the key property deciding the distinct fates of excess Cdc12(W367K) versus

Cdc12(W367K E368V) is most likely the ability of Cdc12(W367K E368V) to homodimerize. We conclude that an important, previously unappreciated function of CTD-mediated homo-oligomerization is to promote the assembly of a transient, metastable reservoir of super-stoichiometric septins that are competent to incorporate into septin hetero-octamers and filaments once partner septins become available (Fig.10E). Homotrimers would simply have a greater "storage capacity" than homodimers. Indeed, studies of the RhxxhE motif in other coiled coils found that while it is enriched in homotrimers, many proteins with the motif form homodimers (Testa *et al.*, 2009). In Cdc12 and homologous septins, the motif contains bulky side chains (Trp and Phe) that are not typically found in the core of dimeric coiled coils. These residues likely favor homotrimerization to accommodate these side chains in a slightly larger radius of a trimeric coiled coil (Woolfson, 2023).

We could find no precedent in the literature for the loss of high-level accumulation we observed for specific septins in *hsp104*Δ cells. Deletion of *HSP104* did not prevent the *GAL1/10* promoter-driven accumulation of any of many aggregation-prone human proteins or fragments thereof, including Huntingtin (Giorgini *et al.*, 2005), TDP-43, FUS, α-synuclein, or EWSR1 (Jackrel and Shorter, 2014; Jackrel *et al.*, 2014). On the contrary, Hsp104 is *required for* the degradation of yeast-expressed aggregation-prone versions of human ataxin-1 (Lee and Goldberg, 2010), apolipoprotein B, and cystic fibrosis transmembrane conductance regulator (CFTR) (Doonan *et al.*, 2019). We also find it remarkable that of >1,000 essential proteins in *S. cerevisiae*, Hsp104(G214S T499I) specifically perturbs the septin Cdc12 (Schirmer *et al.*, 2004); the additional Hsp104 binding sites in the Cdc12 CTD and their persistent exposure for Hsp104 binding presumably explain why other septins are not targets of Hsp104(G214S T499I).

How are excess septins targeted for proteolysis? Like Parkin, yeast Dma1 and Dma2 are E3 ubiquitin-protein ligases that mediate ubiquitinylation of septins, and the mammalian Dma homolog, RNF8, promotes ubiquitinylation of human Septin-7 (Chahwan *et al.*, 2013). Interestingly, Cdc12 K351 was found to be ubiquitinylated in a proteomic study (Swaney *et al.*, 2013), but this cannot be the only lysine mediating Cdc12 degradation, since excess Cdc12ΔCTD was degraded in *hsp104*Δ cells (Fig. 4C). Future work will be required to dissect the molecular properties that make excess septins targets for Hsp104 intervention and, when Hsp104 is absent, intervention by the proteasome. Such studies could reveal valuable insights regarding the molecular etiology of human diseases linked to septin aggregation and degradation.

Earlier in vitro studies supported a model in which a G-partnerless septin is prone to loss of bound nucleotide, which destabilizes the G interface and predisposes to β aggregation (Garcia *et al.*, 2007; Pissuti Damalio *et al.*, 2012; Kumagai *et al.*, 2019). It is easy to imagine how this could work, given the proximity of the nucleotide-binding pocket and key features of the G dimer interface to the aggregation-prone β4 strand. Consistent with

this hypothesis, a Cdc10 mutant that likely cannot bind GDP shows prolonged interaction with Hsp104 (Johnson *et al.*, 2015; Denney *et al.*, 2021). However, in the non-native septin filaments composed only of "excess" Cdc3 and Cdc10 that assemble upon simultaneous co-overexpression of specific tagged forms of these two septins (Benson and McMurray, 2023), the nucleotide-binding pockets of Cdc3 and Cdc10 should be fully occupied, yet deletion of *HSP104* blocked accumulation of Cdc3–Cdc10 (Fig. 9D). This finding thus points to the earliest stages of individual septin folding — prior to septin-septin hetero-oligomerization — as the crucial period for stabilization by Hsp104. In support of this model, we previously detected Hsp104 co-eluting specifically with newly-made molecules of a G-interface-mutant Cdc10 (Johnson *et al.*, 2015).

If Hsp104 acts on individual septins before they hetero-oligomerize, why are superstoichiometric septins specifically susceptible, when hetero-oligomerization is the step where stoichiometry is defined? One possibility is that GTP/GDP availability is limited (Bianchi-Smiraglia *et al.*, 2021; Scott *et al.*, 2024), and excess septins are poor nucleotide scavengers and tend to be nucleotide-free and consequently misfolded. Alternatively, kinetics may be the key. Septins that are delayed in G dimerization are excluded from hetero-octamers by faster-associating competitor septins and their G interfaces are instead bound by chaperones (Johnson *et al.*, 2015; Schaefer *et al.*, 2016; Denney *et al.*, 2021). If co-overexpressed Cdc3 and Cdc10 are slower to assemble into homodimers or non-native Cdc3–Cdc10 polymers than to incorporate into hetero-octamers, then the window of misfolding/aggregation opportunity is wider for these excess septins than for septins that quickly homo-oligomerize, and the requirement for Hsp104 is correspondingly greater. An untested prediction of this model is that, like its paralog Cdc11, purified Shs1 quickly forms CTD-mediated homodimers that would serve in cells to stabilize superstoichiometric Shs1 against aggregation/degradation. The existence of such homodimers in vivo likely explains why Cdc11 and Shs1 perturb septin hetero-octamer function when overexpressed: they "cap" octamer ends and interfere with polymerization into filaments.

Whereas previous studies emphasized the importance of a G-dimer partner in stabilizing the septin GTPase domain against aggregation and/or chaperone sequestration, here we propose that homo-oligomerization via the CTD — considered an extension of the NC interface — also performs this function (Fig.10E). A portion of the Cdc12 CTD has homology to a C-terminal domain of Ran GTPases that allosterically communicates with parts of the GTPase domain that change conformation upon GTP hydrolysis (Vetter *et al.*, 1999; Nilsson *et al.*, 2002; Weems *et al.*, 2014). Removing the Cdc12 CTD accelerates GTPase activity (Versele and Thorner, 2004), providing more evidence of such communication. Several other mechanisms have also been proposed that link conformational changes at the G interface with changes in parts of the NC interface (Sirajuddin *et al.*, 2009; Zeraik *et al.*, 2014; Mendonça *et al.*, 2024). It is also possible that CTD-mediated homo-oligomerization simply brings the GTPase domains in close proximity and promotes otherwise low-affinity associations between them

(see Figs. S6, S8), which somehow protects against degradation (Fig.10E). Additional studies will be needed to better understand what stabilizes septins.

We are careful not to assume that aggregation necessarily precedes or drives septin degradation. What constitutes a septin "aggregate" is also imprecisely defined. Upon mild heat shock, some misfolded mutant yeast proteins transiently coalesce with Hsp104 and other chaperones, which protects them against proteasomal degradation (Boronat *et al.*, 2023). Due to limited resolution, the mostly diffuse cellular fluorescence we observe for overexpressed, tagged single septins cannot be interpreted as "soluble" protein, and our SEC analysis would have missed large complexes that co-eluted with hetero-octamers or pelleted when we clarified our lysates. While the simplest explanation is that Hsp104 binding counteracts aggregation by excess septins, further studies will be required to rigorously test this model.

As it remains mechanistically unclear how PP2A–Rts1 ($PP2A^{Rts1}$) phosphatase activity affects septins, we do not fully understand why *RTS1* deletion ameliorated the septin dysfunction observed upon overexpression of Cdc12(W367K). $PP2A^{Rts1}$ dephosphorylates Shs1 (Dobbelaere *et al.*, 2003), the other mitotic yeast septin with a C-terminal curvature-sensing amphipathic helix; deletion of both amphipathic helices severely cripples septin function (Woods *et al.*, 2021). $PP2A^{Rts1}$ acts on Shs1 during or just prior to cytokinesis (Dobbelaere *et al.*, 2003) and may modify curvature sensing by the Shs1 amphipathic helix to accommodate changes in plasma membrane curvature. Additionally, a phosphoproteomic study identified Ser509 in the CTD of Cdc3 as undergoing Rts1-dependent dephosphorylation (Touati *et al.*, 2019). Cdc3 Ser509 lies just C-terminal of the residues predicted to engage the CTD of Cdc12 in a heterodimeric coiled coil (Fig. 1A) and adjacent to the Cdc3 "polybasic region 3" (**S**PVPTKKKGFLR, basic residues underlined), which may also influence membrane interactions (Cavini *et al.*, 2024). The dephosphorylation events appear to drive "mobility" of septins within the septin ring (Dobbelaere *et al.*, 2003) at the same time when polarized fluorescence microscopy reveals large-scale reorientation of the Cdc12 CTD (Vrabioiu and Mitchison, 2006; DeMay *et al.*, 2011; McQuilken *et al.*, 2017). These changes in higher-order septin structure likely reflect orchestrated rearrangement of the meshwork of septin filaments with respect to each other and the plasma membrane. CTD mutations in Cdc12 disrupt these dynamics; persistent phosphorylation of Shs1 and the Cdc3 CTD in *rts1*Δ cells may allow cytokinesis by restoring filament-filament interactions and/or interactions between filaments and the membrane. We speculate that the temperature-sensitive nature of the dysfunction caused by Cdc12 CTD mutations (and by *RTS1* deletion in cells with wild-type Cdc12 (Dobbelaere *et al.*, 2003)) reflect temperature effects on plasma membrane properties that indirectly impinge on higher-order septin structure and function. Such effects likely explain why mutating R363 (also within the Cdc12 trimerization motif) to Lys has little effect on CTD oligomerization in vitro (Table S4) but makes cells sensitive to cold temperatures (Cvrcková and

Nasmyth, 1993; Weems *et al.*, 2014), which strongly alter membrane fluidity and lipid composition (Gunde-Cimerman *et al.*, 2013).

Human cells lack Hsp104 and the Cdc10 homolog septin-9 lacks a CTD but at least in some circumstances septin-9 appears to persist stably outside of septin hetero-oligomers. For example, whereas in a human chronic myelogenous leukemia cell line ectopic expression of tagged septin-9 or depletion of endogenous septin-7 (the G dimer partner) results in disappearance of endogenous septin-9 molecules not incorporated into hetero-oligomers (Sellin *et al.*, 2012), in an osteosarcoma cell line mutating the G interface of septin-9 results in the accumulation of what appear to be septin-9 monomers (Kuzmić *et al.*, 2022). Mutating the Septin-7 G interface in mouse embryonic fibroblasts also generates apparent Septin-9 monomers (Abbey *et al.*, 2016). Most septin-9 isoforms have extended N-terminal domains that may confer monomer stability. Alternatively, other mammalian chaperones might perform Hsp104's septin-stabilizing function.

Cancer cells appear to exploit the homo-oligomerization properties of septin CTD coiled coils for other purposes: spontaneous fusions of the epidermal growth factor receptor (EGFR) to the coiled coil sequence in the CTD of human Septin-14 are the most frequently found functional gene fusion in glioblastoma (Frattini *et al.*, 2013) and have also been found in colorectal cancer (Li *et al.*, 2020) and lung adenocarcinoma (Zhu *et al.*, 2019). Artificial EGFR dimerization via fusion to a leucine zipper is sufficient to activate its signaling activity in a ligand-independent manner (Kourouniotis *et al.*, 2016). Hence, fusion to the Septin-14 sequence presumably drives EGFR homodimerization. Notably, Septin-14 is not predicted to homodimerize within the septin hetero-octamers that comprise septin filaments in non-cancer cells (Wang *et al.*, 2025), but purified Septin-14 CTD can indeed form coiled-coil homodimers in vitro (Cavini *et al.*, 2023). Whether transient Septin-14 coiled-coil homo-oligomers play a role in septin hetero-octamer assembly is an interesting question for future research.

METHODS

Strains and plasmids

Plasmids for *E. coli* expression of Cdc12 (Uniprot:P32468) or Cdc3 (Uniprot:P32457) or fragments thereof were made by PCR amplification from full-length synthetic genes with optimized codons for *E. coli* (Synbio). A tryptophan residue was inserted at the N terminus of Cdc3 CTD constructs. For CTD fragments, the amplified DNA fragment was purified and subcloned using restriction enzymes (*Nde*I and *Xho*I) into pET28a(+) vector (Novagen), yielding a sequence with an N-terminal H_6 tag and a thrombin cut site. For MBP-fused Cdc12 constructs, the insert with *BamH*I and *Xho*I terminal sites was cloned into pOPINM vector (Novagen) with the In-fusion HD cloning kit (Takara), resulting in a coding sequence with a H_6 tag and MBP at the N-terminus and

a tripeptide linker (SGS) between the MBP and the Cdc12 sequence. Site-directed mutagenesis of *E. coli* expression plasmids was performed using non-overlapping primers (NEBaseChanger, New England BioLabs) and the mutations were confirmed by Sanger sequencing.

The following plasmids were used for yeast expression. pMVB2 (Versele *et al.*, 2004) was used to express Cdc12-GFP under control of the *GAL1/10* promoter, and derivatives thereof were previously published (pMVB160, encoding Cdc12ΔCTD-GFP (Versele *et al.*, 2004)) or made via site-directed mutagenesis by Keyclone Technologies (C6F1B99E, encoding Cdc12(N379D W367K)-GFP; BD7C264E, encoding Cdc12(N379D E368V)-GFP), 9F2B6E98, encoding Cdc12(N379D W367K E368V)-GFP)) or GenScript (10633A79, encoding Cdc12(W367K)-GFP, with the N379D mutation repaired). pMVB169 (*ARS/CEN URA3* $P_{GAL1/10}$*–CDC3*) is based on plasmid TS395 (Carminati and Stearns, 1997) with the *CDC3* ORF cloned into the *Bam*HI site but has no GFP, and was constructed by Matthias Versele while in the lab of Jeremy Thorner. D2AC2EB4, encoding Cdc12-GFP(β1-9), was made by recombination in yeast: pMVB2 digested with *Xba*I and *Not*I was co-transformed into strain BY4742 with a PCR product made from template plasmid pGF-IVL794 (*GAL1/10* promoter driving the fragment of GFP(β1-9) (Finnigan *et al.*, 2016)) with primers Cdc12-GFP(1-9)fw and Cdc12-GFP(1-9)re. Primer sequences are provided in Table S5. 15C00ABB, encoding Cdc12(W367K)-GFP(β1-9) was made by GenScript via site-directed mutagenesis of template plasmid D2AC2EB4. 76068B19, encoding Cdc12-GFP(β10), was made by recombination in yeast: pLP29 (Lippincott and Li, 2000) was digested with *Bam*HI and *Xba*I and co-transformed into BY4741 with annealed primers Cdc12-GFP(10)fw and Cdc12-GFP(10)re. E2438448, encoding Cdc12(W267A)-GFP(β11), was made by recombination in yeast: YCpL-Cdc12W267A (McMurray *et al.*, 2011), a derivative of pMVB45 (Versele *et al.*, 2004), was linearized with *Bam*HI and co-transformed into BY4741 with annealed and extended oligos Cdc12-GFP(11)fw and Cdc12-GFP(11)reFIXED. pRS313 and pRS316 have been described previously (Sikorski and Hieter, 1989), as have *HSP104* plasmids 5679 and 5707 (Schirmer *et al.*, 2004). Plasmid 1EB21EA6 encodes Cdc12(G268R W367K)-GFP under *GAL1/10* promoter control and was made by GenScript via site-directed mutagenesis from template plasmid 10633A79. Plasmid YEp-Cdc12(G268R W367K)-GFP encodes Cdc12(G268R W367K)-GFP under *CDC12* promoter control was made by recombination in yeast: pMVB62 (2 µm origin, *CDC12-GFP HIS3* (Versele *et al.*, 2004)) was digested with *Mlu*I and *Hpa*I to excise a portion of the *CDC12* coding sequence and transformed into BY4741 yeast cells carrying plasmid 1EB21EA6. pMETp-CDC10-GFP and the derivative encoding Cdc10αΔ0 (pJT3456) have been described previously (McMurray *et al.*, 2011), as has the *GAL1/10 CDC3-GFP URA3* plasmid pMVB1 (Schaefer *et al.*, 2016), pGF-IVL-287 (*LEU2* P_{GAL}*–CDC11-mCherry*) and pGF-IVL-286 (*LEU2* P_{GAL}*–SHS1-GFP* (Takagi *et al.*, 2021), and plasmids G01273 (P_{GAL}*–CDC3-mCherry–CDC10-GFP*), E00432 (P_{GAL}*–CDC3ΔNTD-*V_C*–CDC10-*V_N), and E00435 (P_{GAL}*–CDC3ΔNTD-*V_C*–CDC10-*V_N) (Benson and McMurray, 2023).

The following yeast strains were used. Existing strains were BY4741, BY4742, and BY4743 (Winzeler *et al.*, 1999); JTY4013 (BY4742 *hsp104Δ::kanMX* (Johnson *et al.*, 2020)); H06799 (BY4741 *HSP104-mCherry* (Hassell *et al.*, 2022)); H07151 (BY4741 *mCherry-CDC3::LEU2* (Benson and McMurray, 2023)); and GFY-160 (BY4741 *CDC11-mCherry::Sphis5 SHS1-eGFP::natMX*) (Finnigan *et al.*, 2015b). The *cdc10Δ::kanMX* strain JTY4010 (McMurray *et al.*, 2011) is originally from the haploid deletion collection (Winzeler *et al.*, 1999). The *pre1(S142F) hsp104Δ* strain F93544A5 was made by crossing JTY4013 (Johnson *et al.*, 2015) with the "*pre1-1*" strain from the BY4741-based temperature-sensitive mutant collection (Li *et al.*, 2011), inducing sporulation in the resulting diploid by plating on 1% potassium acetate agar medium, and dissecting the resulting tetrads. The *cdc3Δ::kanMX/CDC3* strain from the heterozygous deletion collection (Winzeler *et al.*, 1999), which is also heterozygous for a deletion allele at the *MET15*/*MET17/MET25* locus, was transformed with pMVB169. Cells from a plasmid-selective liquid culture were plated onto galactose-containing lead nitrate medium (Cost and Boeke, 1996). Spontaneous recombination events in between rDNA sequences frequently lead to loss of heterozygosity of centromere-distal loci, including *MET15* and *CDC3*. A brown colony, presumed to be *met15Δ/met15Δ cdc3Δ/cdc3Δ*, was confirmed by plating to YPD (2% peptone, 1% yeast extract, 2% glucose) to require galactose for survival; the resulting strain is named MMY0296. Synthetic medium for yeast growth was based on YC (0.1 g/L Arg, Leu, Lys, Thr, Trp, and uracil; 0.05 g/L Asp, His, Ile, Met, Phe, Pro, Ser, Tyr, and Val; 0.01 g/L adenine; 1.7 g/L Yeast Nitrogen Base without amino acids or ammonium sulfate; 5 g/L ammonium sulfate; 2% dextrose or galactose) with individual components eliminated as appropriate for plasmid selection. For solid media, agar was added to 2%.

Peptide expression and purification

E. coli Rosetta(DE3) (Novagen) or T7Express (NEB) strains transformed with the respective plasmid were grown in LB medium containing the appropriate antibiotic(s) for selection. Culture was grown at 37 °C and when OD_{600nm} reached 0.6-0.8, isopropyl-β-D-thiogalactopyranoside (IPTG) was added to 0.2 mM to induce protein expression, which was carried out overnight at 18 °C. Cells were harvested by centrifugation, solubilized in buffer '2x' (100 mM Tris pH 8.0, 1 M NaCl) containing 10 mM imidazole, and lysed by sonication. For Cdc12 constructs, the cell extract was cleared by centrifugation, applied to an immobilized metal affinity chromatograph (IMAC) column (Ni-NTA agarose, Qiagen or HisTrap HP, Cytiva) and washed exhaustively with buffer '2x' plus 10 mM imidazole. An additional washing step (4 column volumes, buffer '2x' plus 35 mM imidazole) was carried out prior to elution (6 column volumes, buffer '2x' plus 200 mM imidazole). Bovine thrombin (Sigma Aldrich #T7326) was added to the eluted peptide in a 2 U/mg ratio and the solution was dialyzed overnight against buffer '1x' (50 mM Tris pH 8.0, 500 mM NaCl) using a 3 kDa dialysis membrane (Spectrum labs), except for the MBP-fused constructs. Solution was loaded to a Benzamidine

Sepharose 6B resin (GE Healthcare) to remove thrombin and later to a second metal affinity chromatography to remove Histag-containing fragments. Size-exclusion chromatography (SEC) was performed in buffer containing 50 mM Tris pH 8.0, 300 mM NaCl using Superdex 75 10/300 (for CTD and CC constructs) or Superdex 200 10/300 columns (for MBP-fused constructs) assisted by an AKTA FPLC system (GE Healthcare). Protein purity was analyzed either by 12% SDS-PAGE or 16% tricine-SDS-PAGE. Cdc3C (UniProt: P32457, residues 413–520) and Cdc3CC (residues 427–503) were purified using the same general procedure, except that both proteins were obtained through a refolding protocol. The insoluble fraction of the cell lysate was resuspended in '2x' buffer containing 6 M urea, and the clarified material was loaded onto a Ni–NTA agarose (Qiagen) column. The resin was subsequently washed with '2x' buffer (urea-free) using a 60-minutes linear gradient on an FPLC system, corresponding to a decrease of 0.1 M urea per minute. Cdc3C and Cdc3CC were then eluted as usual with buffer '2x' plus 200 mM imidazole.

Circular dichroism (CD) spectroscopy

Far-UV circular dichroism (CD) experiments were conducted using a Jasco J-815 spectropolarimeter equipped with a Peltier temperature control module. Purified peptides were prepared at a concentration of 10 µM in a buffer consisting of 20 mM sodium phosphate, 50 mM NaCl, 10% glycerol, pH 7.5. Buffer exchange was performed with a sample dilution of at least 100-fold. Sample was placed in a 1 mm Suprasil quartz cuvette and CD spectra were collected at 4 °C in a wavelength range from 195 to 260 nm, in 1 nm steps, a speed of 100 nm/min and a response time of 0.5 s. A series of six scans were collected, which were averaged and subsequently subtracted from the buffer contribution. Secondary structure content was calculated with BeStSel (Micsonai *et al.*, 2025). Thermal denaturation experiments were monitored at 222 nm over a temperature range of 5 to 80 °C, with data collected every 1 °C and a temperature ramp rate of 1 °C/min. Ellipticity values were normalized from zero (native state, low temperature) to one (denatured state, high temperature) using the measured ellipticities on each plateaus. Sigmoid curves were fitted with either a single or a double Boltzmann equation to obtain the CD melting temperature(s) (T_m).

Size-exclusion chromatography coupled to multi-angle light scattering (SEC-MALS)

Purified peptides at a concentration of 300 µM (~2.6 and 3.4 mg/ml for Cdc12CC and Cdc12C constructs, respectively) were loaded into a Superdex75 10/300 GL column coupled to a Waters 600 Controller HPLC chromatograph. A 0.5 ml/min flow rate and a 50 mM Tris, 300 mM NaCl, pH 8.0 running buffer were used. Multi-angle light scattering (MALS) and the differential refractive index (dRI) of the eluted fractions were analyzed by miniDAWN-TREOS and Optilab T-rEX detectors (Waters Corp.), respectively. Light scattering coefficients obtained from BSA monomer peak were used in MALS detectors normalization. Data were analyzed with ASTRA 7 software.

Size-exclusion chromatography coupled to small-angle X-ray scattering (SEC-SAXS)

SEC-SAXS experiments were performed at the B21 beamline (Diamond Light Source, UK) (Cowieson *et al.*, 2020). The setup employed an Agilent 1200 HPLC system with a Superdex 200 increase 3.2/300 column (GE Healthcare). Samples were prepared at a concentration of 5 mg/ml and a volume of 45 µl was injected and analyzed at a flow rate of 0.075 ml/min in buffer containing 50 mM Tris, 150 mM NaCl, pH 7.5. Data collection was acquired at 15 °C with a wavelength of 0.9464 Å by an EigerX 4 M (Dectris) detector positioned at a fixed camera length of 3.7209 m. The angular q range recorded was from 0.0045 to 0.34 $Å^{-1}$ with a photon flux of 4.1012 s^{-1}.

For data analysis, ScatterIV (Tully *et al.*, 2021), ATSAS (Manalastas-Cantos *et al.*, 2021) and BioXTAS RAW (Hopkins *et al.*, 2017) were used. Mass estimation was carried out through Bayesian inference (Hajizadeh *et al.*, 2018), Size&Shape (Franke *et al.*, 2018) and the volume of correlation methods (Rambo and Tainer, 2013). Atomistic modeling was carried out with MultiFoXS (Schneidman-Duhovny *et al.*, 2016) and/or EOM-NNLSJOE (Bernadó *et al.*, 2007; Tria *et al.*, 2015) considering flexible linkers between the MBPs and the CC helices and using either dimers, trimers or an ensemble of both. The radius of gyration (R_g) in an ensemble was calculated as a weighted root mean square of the individual R_g values. Ab initio bead density models were generated initially by DAMMIF (Franke and Svergun, 2009) averaged over 23 independent runs using DAMAVER (Volkov and Svergun, 2003), and later by a single run of DAMMIN (Svergun, 1999) in ATSAS online 3.2.1 using dummy atoms with 5 Å radius. Calculated and experimental curves were compared using the correlation map method (CorMap) with a P-value of 0.01 as threshold (Franke *et al.*, 2015).

Size-exclusion chromatography of yeast lysates

50-mL cultures in synthetic plasmid-selective medium were pelleted and the cells were washed with PBS, resuspended in 1 mL PBS and transferred to a 2-mL screw-cap microcentrifuge tube, and lysed by four rounds of vortexing for 1 min each following the addition of 0.5-mm zirconia/silica beads (Biospec Products #11079105z). The tubes were incubated on ice for 1 min between each round of vortexing. Lysates were clarified by centrifugation at 16,300 rcf for 10 min at 4˚C. 0.5 mL of clarified lysate was separated in PBS on a HiLoad 16/600 Sephacryl S200 column (GE Healthcare) column run at 0.5 mL/min. The column had been previously calibrated with ~1 mg thyroglobulin, ~1.5 mg alcohol dehydrogenase from *S. cerevisiae*, and ~2 mg albumin (from kit #MWGF1000, Sigma-Aldrich) dissolved together in 500 µL PBS.

BS3 chemical crosslinking

Bis(sulfosuccinimidyl)suberate (BS3) crosslinking agent (molecular weight, 572.43 Da; spacer arm, 11.4 Å, Thermo-Fisher Scientific #21580)) was used to analyze the oligomeric state of samples. Buffer used was 50 mM sodium phosphate, 300 mM NaCl, pH 8.5. BS3 concentration used was 2.5 mM (25-fold excess, 100 µM peptide) and samples were incubated on ice for 2 hours and 30 minutes. Reactions were stopped by the addition of 50 mM Tris-HCl pH 8.0 and analysed by 16% tricine-SDS-PAGE.

Structural model predictions and coiled-coil structural analysis

The sequence logo was generated with WebLogo (Crooks *et al.*, 2004) from 249 UniRef50 amino acid sequences identified using Cdc12 as the query. Deep-learning structural predictions were performed using the AlphaFold3 server (Abramson *et al.*, 2024). Model confidence was assessed by pLDDT (predicted local distance difference test) and pAE (predicted aligned error). Coiled-coil radii were obtained using SamCC-Turbo (Szczepaniak *et al.*, 2021). Predictions were deposited in ModelArchive. The "Contacts" function in ChimeraX v1.8 with van der Waals overlap ≥ -0.40 Å was used to predict intermolecular contacts.

Nanodifferential scanning fluorimetry (NanoDSF)

Intrinsic protein fluorescence was analysed by Prometheus Panta (Nanotemper Technologies). The excitation wavelength of 280 nm was used, and the emission was measured at 330 nm and 350 nm. The buffer used was 25 mM sodium phosphate, 150 mM NaCl, pH 7.0. Samples at 90 µM concentration (1 mg/ml) were loaded into nanoDSF capillaries (Nanotemper Technologies, #PR-C006) in duplicates and transferred to the Prometheus NT.48 apparatus. Samples were heated from 18 to 90 °C (unfolding phase) and 578 measurements were taken (every 0.125 °C). Data were analyzed with Prometheus PR Control software (NanoTemper Technologies).

Dot blotting

For analysis of SEC fractions of yeast lysates, the entirety of each 1-mL fraction was applied to a pre-wetted nitrocellulose membrane (GE Water & Process Technologies #WP4HYB0010) via vacuum using a Hybri-dot manifold (Bethesda Research Laboratories #1050MM). One dot was loaded with PBS alone, as a background control. The membrane was air dried, incubated in TBS for 5 min, and then blocked by incubation in Intercept (TBS) Blocking Buffer (Li-Cor #927-60001) for 1 hour. The membrane was incubated in anti-GFP antibody (Sigma-Aldrich #11814460001 RRID:AB_390913) or anti-Hsp104 antibody (Enzo Life Sciences #ADI-SPA-1040-D RRID:AB_2039208) diluted 1:1,000 in blocking buffer to which Tween 20 (Sigma #P-1379) was added to 0.2%. Following four 5-minute washes with TBS with 0.2% Tween 20 (called TBST), the membrane was incubated for 1 hour in an infrared-fluorophore-labeled secondary antibody (Life Technologies Corporation # W10815 RRID:AB_2556797 or Invitrogen #35569 RRID:AB_1965957) diluted 1:10,000 in TSBT. Following four 5-minute washes with TBST, the blot was scanned with a Li-Cor Odyssey infrared scanner. Signal

intensities were quantified using FIJI (Schindelin *et al.*, 2012) using circular regions of interest slightly larger than the dot size. The signal intensity of the PBS background control dot was subtracted from each, and the background-corrected signals were normalized to that of the dot with the highest signal.

For analysis of total protein (unfractionated), protein was extracted from yeast cultures grown to mid- or late-log phase. Cell pellets were washed with 10% trichloroacetic acid (TCA) and frozen in a dry ice/ethanol bath then thawed in 150 µL of 1.85 M NaOH and 7.4% β-mercaptoethanol. 150 µL of 100% TCA was added before incubation on ice for 10 min. Precipitated proteins were pelleted at 4°C at maximum speed for 10 min, washed twice with cold acetone (1 mL each time), and air dried. Pellets were resuspended in 75 µL of 0.1 M Tris base, 5% SDS. After addition of 25 µL 4X Laemmli buffer (250 mM Tris-HCl (pH 6.8), 8% SDS, 40% glycerol, 0.02% bromophenol blue), the samples were boiled for 5 min and frozen at -20˚C. Samples were thawed at 55˚C and 3 uL aliquots were spotted on nitrocellulose membranes. The membranes were blocked using Intercept (TBS) Blocking Buffer and then submerged for 1 hr in Antibodies (rabbit Anti-Glucose-6-Phosphate Dehydrogenase (Sigma-Aldrich #A9521, RRID AB_258454) or rabbit anti-mCherry (EnCor Cat# RPCA-mCherry, RRID AB_2571870) diluted 1:1000 in blocking buffer. Membranes were then washed thrice with TBST (TBS with 0.1% Tween 20 and submerged for 1 hr in a 1:1000 dilution of Peroxidase Conjugated Goat Anti-Rabbit IgG (ThermoScientific #32460 RRID:AB_1185567) in blocking buffer. After three TBST washes, the membranes were submerged in SuperSignal™ West Pico Chemiluminescent Substrate (Pierce #34080) for 10 minutes prior to imaging with a Bio-Rad Chemidoc MP imaging system. Quantification was performed in FIJI by calculating the integrated density for each spot using a 118x120-pixel oval area. Values for two empty areas of the same size on the same membrane were averaged and subtracted from the values for each sample on the same membrane. Each background-corrected value for mCherry was then normalized to that of Zwf1. Finally, the Zwf1-normalized values were normalized to that of the *CDC3-mCherry* sample (strain H07151).

smiFISH

smiFISH was performed using Stellaris RNA FISH buffers (SMF-HB1, SMF-WA1, SMF-WB1, Biosearch Technologies) essentially as described previously (Tsanov *et al.*, 2016) but modified for budding yeast cells according to Stellaris instructions. Briefly, fixed cells were prepared from 50-mL YPD cultures grown to an OD_{600} of 0.2-0.5 and pelleted at 1600 x *g* for 4 minutes in a centrifuge. Cells were resuspended in 1 mL ice-cold methanol, transferred to a 1.5-mL microcentrifuge tube, and incubated at -20˚C for 10 minutes. Following another pelleting step and two washes with 1 mL ice-cold Fixation buffer (1.2 M sorbitol, 0.1 M potassium phosphate), cells were resuspended in 1 mL of Fixation buffer plus 2.5 µL Zymolyase 20T (#Z1000, US Biologicals) 2.5 mg/mL dissolved in water). Cell wall digestion was performed at 30˚C for ~2 hr then cells were pelleted at 1,000 x *g* for 3-5 minutes and washed twice with ice-cold Fixation buffer. Cells were permeabilized

by resuspending in 1 mL 70% ethanol and stored at 4˚C prior to hybridization. For hybridization, 300 µL of fixed yeast cells in 70% ethanol were pelleted at 400 x *g* and resuspended in 100 µL Hybridization Buffer containing probes, then incubated in the dark at 30˚C overnight. 100 µL of Wash Buffer A was added and cells were pelleted at 400 x *g* for 5 minutes. Cells were resuspended in 1 mL of Wash Buffer A and incubated in the dark at 30˚C for 30 minutes. After pelleting again at 400 x *g* for 5 minutes, cells were resuspended in 1 mL of DAPI stain (Wash Buffer A consisting of 5 ng/mL DAPI) and incubated in the dark at 30˚C for 30 minutes. Cells were pelleted and resuspended in 1 mL of Wash Buffer B for 5 minutes, then pelleted and resuspended in a small drop of Vectashield Mounting Medium (Vector Laboratories, #H-1000). 5-10 µL of Vectashield-suspended yeast cells were spotted on a glass microscope slide and then covered with an 18 × 18 mm square #1 coverglass. The coverglass was pressed onto the slide and excess mounting medium was removed with a laboratory wipe. The coverglass perimeter was sealed with clear nail polish. All probes were purchased from Integrated DNA Technologies. Primary probes (13-19 per mRNA) were designed manually; sequences used are provided in Table S5. Primary probes were combined in equimolar amounts and diluted to 20 µM and hybridized with the fluorescent FLAP probe. 3.125 µL of hybridized probe was added to 100 µL of Hybridization buffer. Slides were imaged using a 63X objective on a widefield DeltaVision Microscope with consistent laser intensity and exposure times across samples. For the negative control for the Cdc3 probe set, strain MMY0296 was cultured in plasmid-selective medium containing 2% raffinose overnight and then glucose was added to 2% final concentration to block new *CDC3* transcription. The cells were then fixed after 6 hr at 30˚C. The *cdc10*Δ*::kanMX* strain is known to be as large as wild-type diploid cells (Jorgensen *et al.*, 2002).

Microscopy

Micrographs were captured with an EVOSfl all-in-one epifluorescence microscope (Thermo-Fisher Scientific) with a 60× oil objective and GFP (#AMEP4651) and Texas Red (#AMEP4655) LED/filter cubes. Image adjustment was performed using FIJI software (Schindelin *et al.*, 2012). Cellular length-to-width ratios were calculated with FIJI line tool as described previously (Benson and McMurray, 2023).

DATA AVAILABILITY

SEC-SAXS datasets and analysis are available in SASBDB (sasbdb.org) with the respective accession codes: MBP-Cdc12 CTD 332-407aa “MBP-Cdc12CC+8” (SASDYR4), MBP-Cdc12CC+8 peak front (SASDYS4), MBP-Cdc12CC+8 peak tail (SASDYU4) and MBP-Cdc12 CTD 340-407aa “MBP-Cdc12CC” (SASDYQ4). The following AlphaFold structural predictions are available in ModelArchive (modelarchive.org) with the respective accession codes: Hsp104 N-terminal domain/Cdc12 WALTZ amyloidogenic sequence (ma-k1rre), Hsp104 N-terminal domain/Cdc12 C-terminal domain (ma-gmeo1), Hsp104 N-terminal domain/full-length Cdc12 (ma-huwgf), Hsp104 N-terminal domain/Cdc10 WALTZ amyloidogenic sequence (ma-5n6qq), Hsp104

N-terminal domain/Sup35 binding site (ma-vj5d5), Cdc12-Cdc3 heterodimeric coiled coil (ma-t43av), Cdc12 homotrimeric coiled coil (ma-nmv5d), shorter Cdc12 homotrimeric coiled coil (ma-evurw), full-length Cdc12 dimer with GDP (ma-5hhc4), full-length Cdc12 trimer with GDP (ma-99kcr), full-length Cdc11-3xCdc12-Cdc3-Cdc10 TriFC complex (ma-37ka2) and full-length 3xCdc12 TriFC complex (ma-s4slk).

ACKNOWLEDGEMENTS

We thank Prof. Matthew P. Crump (University of Bristol, UK) for providing SEC-SAXS beamtime, B21 beamline specialists (Diamond Light Source, UK) and Daniel Frank (BIOSAXS GmbH, Germany) for the assistance with SEC-SAXS data acquisition/analysis, the Integrated Structural Biology Platform of Carlos Chagas Institute and Dr. Beatriz Gomes Guimarães (Fiocruz Paraná, Brazil) for the use of and help with the nanoDSF/Prometheus Panta, Matt Taliaferro (University of Colorado School of Medicine) for use of the Deltavision microscope, Lenny Teytelman (Protocols.io) for advice with smiFISH, and Allison McClure (University of Colorado School of Medicine) for FPLC use. We gratefully acknowledge the National Institutes of Health (grants T32 GM136444 and R35 GM148198), Fundação de Amparo à Pesquisa do Estado de São Paulo (grants 2015/16812-0, 2018/19992-7, 2020/02897-1, 2022/00262-4 and 2024/23432-8), and a pilot grant from the department of Cell and Developmental Biology at the University of Colorado School of Medicine for financial support. The funders had no role in study design, data collection and analysis, decision to publish or preparation of the manuscript.

DISCLOSURE AND COMPETING INTERESTS STATEMENT

The authors declare that they have no conflict of interest.

REFERENCES

Abbey, M, Hakim, C, Anand, R, Lafera, J, Schambach, A, Kispert, A, Taft, MH, Kaever, V, Kotlyarov, A, Gaestel, M, *et al.* (2016). GTPase domain driven dimerization of SEPT7 is dispensable for the critical role of septins in fibroblast cytokinesis. Sci Rep 6, 20007.

Abramson, J, Adler, J, Dunger, J, Evans, R, Green, T, Pritzel, A, Ronneberger, O, Willmore, L, Ballard, AJ, Bambrick, J, *et al.* (2024). Accurate structure prediction of biomolecular interactions with AlphaFold 3. Nature 630, 493–500.

Adams, AE, and Pringle, JR (1984). Relationship of actin and tubulin distribution to bud growth in wild-type and morphogenetic-mutant Saccharomyces cerevisiae. J Cell Biol 98, 934–945.

Alkhanjari, RR, Alhajeri, MM, Bhamidimarri, PM, Alhosani, K, Kashir, J, Torii, T, and Hamdan, H (2025). Septins in the nervous system: from cytoskeletal dynamics to neurological disorders. Cell Commun Signal CCS 23, 425.

Arava, Y, Wang, Y, Storey, JD, Liu, CL, Brown, PO, and Herschlag, D (2003). Genome-wide analysis of mRNA translation profiles in Saccharomyces cerevisiae. Proc Natl Acad Sci 100, 3889–3894.

Barth, P, Schoeffler, A, and Alber, T (2008). Targeting metastable coiled-coil domains by computational design. J Am Chem Soc 130, 12038–12044.

Baur, JD, Rösler, R, Wiese, S, Johnsson, N, and Gronemeyer, T (2019). Dissecting the nucleotide binding properties of the septins from S. cerevisiae. Cytoskeleton 76, 45–54.

Benson, A, and McMurray, M (2023). Simultaneous co-overexpression of Saccharomyces cerevisiae septins Cdc3 and Cdc10 drives pervasive, phospholipid-, and tag-dependent plasma membrane localization. Cytoskelet Hoboken NJ 80, 199–214.

Bernadó, P, Mylonas, E, Petoukhov, M V., Blackledge, M, and Svergun, DI (2007). Structural characterization of flexible proteins using small-angle X-ray scattering. J Am Chem Soc 129, 5656–5664.

Bertin, A, McMurray, MA, Grob, P, Park, S-S, Garcia, G, Patanwala, I, Ng, H-L, Alber, T, Thorner, J, and Nogales, E (2008). Saccharomyces cerevisiae septins: supramolecular organization of heterooligomers and the mechanism of filament assembly. Proc Natl Acad Sci U S A 105, 8274–8279.

Bertin, A, McMurray, MA, Thai, L, Garcia, G, Votin, V, Grob, P, Allyn, T, Thorner, J, and Nogales, E (2010). Phosphatidylinositol-4,5-bisphosphate promotes budding yeast septin filament assembly and organization. J Mol Biol 404, 711–731.

Bianchi-Smiraglia, A, Wolff, DW, Marston, DJ, Deng, Z, Han, Z, Moparthy, S, Wombacher, RM, Mussell, AL, Shen, S, Chen, J, *et al.* (2021). Regulation of local GTP availability controls RAC1 activity and cell invasion. Nat Commun 12, 6091.

Boronat, S, Cabrera, M, Vega, M, Alcalá, J, Salas-Pino, S, Daga, RR, Ayté, J, and Hidalgo, E (2023). Formation of Transient Protein Aggregate-like Centers Is a General Strategy Postponing Degradation of Misfolded Intermediates. Int J Mol Sci 24, 11202.

Brausemann, A, Gerhardt, S, Schott, A-K, Einsle, O, Große-Berkenbusch, A, Johnsson, N, and Gronemeyer, T (2016). Crystal structure of Cdc11, a septin subunit from Saccharomyces cerevisiae. J Struct Biol 193, 157–161.

Brennan, CM, Vaites, LP, Wells, JN, Santaguida, S, Paulo, JA, Storchova, Z, Harper, JW, Marsh, JA, and Amon, A (2019). Protein aggregation mediates stoichiometry of protein complexes in aneuploid cells. Genes Dev 33, 1031–1047.

Bridges, AA, Zhang, H, Mehta, SB, Occhipinti, P, Tani, T, and Gladfelter, AS (2014). Septin assemblies form by diffusion-driven annealing on membranes. Proc Natl Acad Sci U S A 111, 2146–2151.

Brown, MT, and McMurray, MA (2025). Stepwise order in protein complex assembly: approaches and emerging themes. Open Biol 15, 240283.

Cabantous, S, Nguyen, HB, Pedelacq, J-D, Koraïchi, F, Chaudhary, A, Ganguly, K, Lockard, MA, Favre, G, Terwilliger, TC, and Waldo, GS (2013). A new protein-protein interaction sensor based on tripartite split-GFP association. Sci Rep 3, 2854.

Cannon, KS, Woods, BL, Crutchley, JM, and Gladfelter, AS (2019). An amphipathic helix enables septins to sense micrometer-scale membrane curvature. J Cell Biol, jcb.201807211.

Carminati, JL, and Stearns, T (1997). Microtubules orient the mitotic spindle in yeast through dynein-dependent interactions with the cell cortex. J Cell Biol 138, 629–641.

Castro, DKSV, Rosa, HVD, Mendonça, DC, Cavini, IA, Araujo, APU, and Garratt, RC (2023). Dissecting the Binding Interface of the Septin Polymerization Enhancer Borg BD3. J Mol Biol 435, 168132.

Cavini, IA, Fontes, MG, Zeraik, AE, Lopes, JLS, and Araujo, APU (2024). Novel lipid-interaction motifs within the C-terminal domain of Septin10 from Schistosoma mansoni. Biochim Biophys Acta Biomembr 1866, 184371.

Cavini, IA, Leonardo, DA, Rosa, HVD, Castro, DKSV, D'Muniz Pereira, H, Valadares, NF, Araujo, APU, and Garratt, RC (2021). The Structural Biology of Septins and Their Filaments: An Update. Front Cell Dev Biol 9, 765085.

Cavini, IA, Winter, AJ, D'Muniz Pereira, H, Woolfson, DN, Crump, MP, and Garratt, RC (2023). X-ray structure of the metastable SEPT14-SEPT7 coiled coil reveals a hendecad region crucial for heterodimerization. Acta Crystallogr Sect Struct Biol 79, 881–894.

Chahwan, R, Gravel, S, Matsusaka, T, and Jackson, SP (2013). Dma/RNF8 proteins are evolutionarily conserved E3 ubiquitin ligases that target septins. Cell Cycle Georget Tex 12, 1000–1008.

Cost, GJ, and Boeke, JD (1996). A useful colony colour phenotype associated with the yeast selectable/counter-selectable marker MET15. Yeast Chichester Engl 12, 939–941.

Cowieson, NP, Edwards-Gayle, CJC, Inoue, K, Khunti, NS, Doutch, J, Williams, E, Daniels, S, Preece, G, Krumpa, NA, Sutter, JP, *et al.* (2020). Beamline B21: High-throughput small-angle X-ray scattering at Diamond Light Source. J Synchrotron Radiat 27, 1438–1446.

Crooks, GE, Hon, G, Chandonia, J-M, and Brenner, SE (2004). WebLogo: a sequence logo generator. Genome Res 14, 1188–1190.

Cvrcková, F, and Nasmyth, K (1993). Yeast G1 cyclins CLN1 and CLN2 and a GAP-like protein have a role in bud formation. EMBO J 12, 5277–5286.

DeMay, BS, Noda, N, Gladfelter, AS, and Oldenbourg, R (2011). Rapid and quantitative imaging of excitation polarized fluorescence reveals ordered septin dynamics in live yeast. Biophys J 101, 985–994.

Denney, AS, Weems, AD, and McMurray, MA (2021). Selective functional inhibition of a tumor-derived p53 mutant by cytosolic chaperones identified using split-YFP in budding yeast. G3 Bethesda Md 11, jkab230.

Dobbelaere, J, Gentry, MS, Hallberg, RL, and Barral, Y (2003). Phosphorylation-dependent regulation of septin dynamics during the cell cycle. Dev Cell 4, 345–357.

Doonan, LM, Guerriero, CJ, Preston, GM, Buck, TM, Khazanov, N, Fisher, EA, Senderowitz, H, and Brodsky, JL (2019). Hsp104 facilitates the endoplasmic-reticulum-associated degradation of disease-associated and aggregation-prone substrates. Protein Sci Publ Protein Soc 28, 1290–1306.

Farkasovsky, M, Herter, P, Voss, B, and Wittinghofer, A (2005). Nucleotide binding and filament assembly of recombinant yeast septin complexes. Biol Chem 386, 643–656.

Finnigan, GC, Booth, EA, Duvalyan, A, Liao, EN, and Thorner, J (2015a). The Carboxy-Terminal Tails of Septins Cdc11 and Shs1 Recruit Myosin-II Binding Factor Bni5 to the Bud Neck in Saccharomyces cerevisiae. Genetics.

Finnigan, GC, Duvalyan, A, Liao, EN, Sargsyan, A, and Thorner, J (2016). Detection of protein-protein interactions at the septin collar in Saccharomyces cerevisiae using a tripartite split-GFP system. Mol Biol Cell 27, 2708–2725.

Finnigan, GC, Takagi, J, Cho, C, and Thorner, J (2015b). Comprehensive Genetic Analysis of Paralogous Terminal Septin Subunits Shs1 and Cdc11 in Saccharomyces cerevisiae. Genetics 200, 821–841.

Franke, D, Jeffries, CM, and Svergun, DI (2015). Correlation Map, a goodness-of-fit test for one-dimensional X-ray scattering spectra. Nat Methods 12, 419–422.

Franke, D, Jeffries, CM, and Svergun, DI (2018). Machine learning methods for X-ray scattering data analysis from biomacromolecular solutions. Biophys J 114, 2485–2492.

Franke, D, and Svergun, DI (2009). DAMMIF, a program for rapid ab-initio shape determination in small-angle scattering. J Appl Crystallogr 42, 342–346.

Frattini, V, Trifonov, V, Chan, JM, Castano, A, Lia, M, Abate, F, Keir, ST, Ji, AX, Zoppoli, P, Niola, F, *et al.* (2013). The integrated landscape of driver genomic alterations in glioblastoma. Nat Genet 45, 1141–1149.

Frazier, JA, Wong, ML, Longtine, MS, Pringle, JR, Mann, M, Mitchison, TJ, and Field, C (1998). Polymerization of purified yeast septins: evidence that organized filament arrays may not be required for septin function. J Cell Biol 143, 737–749.

Gao, X-D, Sperber, LM, Kane, SA, Tong, Z, Tong, AHY, Boone, C, and Bi, E (2007). Sequential and Distinct Roles of the Cadherin Domain-containing Protein Axl2p in Cell Polarization in Yeast Cell Cycle. Mol Biol Cell 18, 2542–2560.

Garcia, G, Finnigan, GC, Heasley, LR, Sterling, SM, Aggarwal, A, Pearson, CG, Nogales, E, McMurray, MA, and Thorner, J (2016). Assembly, molecular organization, and membrane-binding properties of development-specific septins. J Cell Biol 212, 515–529.

Garcia, W, de Araújo, APU, Lara, F, Foguel, D, Tanaka, M, Tanaka, T, and Garratt, RC (2007). An intermediate structure in the thermal unfolding of the GTPase domain of human septin 4 (SEPT4/Bradeion-beta) forms amyloid-like filaments in vitro. Biochemistry 46, 11101–11109.

Giorgini, F, Guidetti, P, Nguyen, Q, Bennett, SC, and Muchowski, PJ (2005). A genomic screen in yeast implicates kynurenine 3-monooxygenase as a therapeutic target for Huntington disease. Nat Genet 37, 526–531.

Grupp, B, Denkhaus, L, Gerhardt, S, Vögele, M, Johnsson, N, and Gronemeyer, T (2024). The structure of a tetrameric septin complex reveals a hydrophobic element essential for NC-interface integrity. Commun Biol 7, 48.

Gunde-Cimerman, N, Plemenitaš, A, and Buzzini, P (2013). Changes in lipids composition and fluidity of yeast plasma membrane as response to cold. In: Cold-Adapted Yeasts: Biodiversity, Adaptation Strategies and Biotechnological Significance, Springer, 225–242.

Haarer, BK, and Pringle, JR (1987). Immunofluorescence localization of the Saccharomyces cerevisiae CDC12 gene product to the vicinity of the 10-nm filaments in the mother-bud neck. Mol Cell Biol 7, 3678–3687.

Hajizadeh, NR, Franke, D, Jeffries, CM, and Svergun, DI (2018). Consensus Bayesian assessment of protein molecular mass from solution X-ray scattering data. Sci Rep 8, 7204.

Harari, A, Zoltsman, G, Levin, T, and Rosenzweig, R (2022). Hsp104 N-terminal domain interaction with substrates plays a regulatory role in protein disaggregation. FEBS J 289, 5359–5377.

Hartwell, LH (1971). Genetic control of the cell division cycle in yeast. IV. Genes controlling bud emergence and cytokinesis. Exp Cell Res 69, 265–276.

Haslberger, T, Zdanowicz, A, Brand, I, Kirstein, J, Turgay, K, Mogk, A, and Bukau, B (2008). Protein disaggregation by the AAA+ chaperone ClpB involves partial threading of looped polypeptide segments. Nat Struct Mol Biol 15, 641–650.

Hassell, D, Denney, A, Singer, E, Benson, A, Roth, A, Ceglowski, J, Steingesser, M, and McMurray, M (2022). Chaperone requirements for de novo folding of Saccharomyces cerevisiae septins. Mol Biol Cell 33, ar111.

Heinemeyer, W, Kleinschmidt, JA, Saidowsky, J, Escher, C, and Wolf, DH (1991). Proteinase yscE, the yeast proteasome/multicatalytic-multifunctional proteinase: mutants unravel its function in stress induced proteolysis and uncover its necessity for cell survival. EMBO J 10, 555–562.

Holstege, FC, Jennings, EG, Wyrick, JJ, Lee, TI, Hengartner, CJ, Green, MR, Golub, TR, Lander, ES, and Young, RA (1998). Dissecting the regulatory circuitry of a eukaryotic genome. Cell 95, 717–728.

Hopkins, JB, Gillilan, RE, and Skou, S (2017). BioXTAS RAW: Improvements to a free open-source program for small-angle X-ray scattering data reduction and analysis. J Appl Crystallogr 50, 1545–1553.

Jackrel, ME, DeSantis, ME, Martinez, BA, Castellano, LM, Stewart, RM, Caldwell, KA, Caldwell, GA, and Shorter, J (2014). Potentiated Hsp104 variants antagonize diverse proteotoxic misfolding events. Cell 156, 170–182.

Jackrel, ME, and Shorter, J (2014). Potentiated Hsp104 variants suppress toxicity of diverse neurodegenerative disease-linked proteins. Dis Model Mech 7, 1175–1184.

Johnson, CR, Steingesser, MG, Weems, AD, Khan, A, Gladfelter, A, Bertin, A, and McMurray, MA (2020). Guanidine hydrochloride reactivates an ancient septin hetero-oligomer assembly pathway in budding yeast. eLife 9, e54355.

Johnson, CR, Weems, AD, Brewer, JM, Thorner, J, and McMurray, MA (2015). Cytosolic chaperones mediate quality control of higher-order septin assembly in budding yeast. Mol Biol Cell.

Johnston, M, Flick, JS, and Pexton, T (1994). Multiple mechanisms provide rapid and stringent glucose repression of GAL gene expression in Saccharomyces cerevisiae. Mol Cell Biol 14, 3834–3841.

Jorgensen, P, Nishikawa, JL, Breitkreutz, B-J, and Tyers, M (2002). Systematic identification of pathways that couple cell growth and division in yeast. Science 297, 395–400.

Kammerer, RA, Kostrewa, D, Progias, P, Honnappa, S, Avila, D, Lustig, A, Winkler, FK, Pieters, J, and Steinmetz, MO (2005). A conserved trimerization motif controls the topology of short coiled coils. Proc Natl Acad Sci U S A 102, 13891–13896.

Kang, PJ, Mullner, R, Lian, K, and Park, H-O (2024). Cdc42 couples septin recruitment to the axial landmark assembly via Axl2 in budding yeast. J Cell Sci 137, jcs261080.

Kilchert, C, and Spang, A (2011). Cotranslational transport of ABP140 mRNA to the distal pole of S. cerevisiae. EMBO J 30, 3567–3580.

Kourouniotis, G, Wang, Y, Pennock, S, Chen, X, and Wang, Z (2016). Non-Ligand-Induced Dimerization is Sufficient to Initiate the Signalling and Endocytosis of EGF Receptor. Int J Mol Sci 17, 1200.

Kumagai, PS, Martins, CS, Sales, EM, Rosa, HVD, Mendonça, DC, Damalio, JCP, Spinozzi, F, Itri, R, and Araujo, APU (2019). Correct partner makes the difference: Septin G-interface plays a critical role in amyloid formation. Int J Biol Macromol 133, 428–435.

Kuzmić, M, Castro Linares, G, Leischner Fialová, J, Iv, F, Salaün, D, Llewellyn, A, Gomes, M, Belhabib, M, Liu, Y, Asano, K, *et al.* (2022). Septin-microtubule association via a motif unique to isoform 1 of septin 9 tunes stress fibers. J Cell Sci 135, jcs258850.

Lee, AR, Kweon, YC, Lee, SM, and Park, CY (2023). Human coronavirus 3CL proteases cleave septins and disrupt Hedgehog signaling, causing ciliary dysfunction. J Med Virol 95, e28618.

Lee, DH, and Goldberg, AL (2010). Hsp104 is essential for the selective degradation in yeast of polyglutamine expanded ataxin-1 but not most misfolded proteins generally. Biochem Biophys Res Commun 391, 1056–1061.

Leonardo, DA, Cavini, IA, Sala, FA, Mendonça, DC, Rosa, HVD, Kumagai, PS, Crusca, E, Valadares, NF, Marques, IA, Brandão-Neto, J, *et al.* (2021). Orientational Ambiguity in Septin Coiled Coils and its Structural Basis. J Mol Biol 433, 166889.

Li, H, Saucedo-Cuevas, L, Yuan, L, Ross, D, Johansen, A, Sands, D, Stanley, V, Guemez-Gamboa, A, Gregor, A, Evans, T, *et al.* (2019). Zika Virus Protease Cleavage of Host Protein Septin-2 Mediates Mitotic Defects in Neural Progenitors. Neuron 101, 1089-1098.e4.

Li, Y, Zhang, H-B, Chen, X, Yang, X, Ye, Y, Bekaii-Saab, T, Zheng, Y, and Zhang, Y (2020). A Rare EGFR-SEPT14 Fusion in a Patient with Colorectal Adenocarcinoma Responding to Erlotinib. The Oncologist 25, 203–207.

Li, Z, Vizeacoumar, FJ, Bahr, S, Li, J, Warringer, J, Vizeacoumar, FS, Min, R, Vandersluis, B, Bellay, J, Devit, M, *et al.* (2011). Systematic exploration of essential yeast gene function with temperature-sensitive mutants. Nat Biotechnol 29, 361–367.

Lippincott, J, and Li, R (2000). Nuclear envelope fission is linked to cytokinesis in budding yeast. Exp Cell Res 260, 277–283.

Long, RM, Singer, RH, Meng, X, Gonzalez, I, Nasmyth, K, and Jansen, RP (1997). Mating type switching in yeast controlled by asymmetric localization of ASH1 mRNA. Science 277, 383–387.

Lum, R, Tkach, JM, Vierling, E, and Glover, JR (2004). Evidence for an Unfolding/Threading Mechanism for Protein Disaggregation by Saccharomyces cerevisiae Hsp104. J Biol Chem 279, 29139–29146.

Manalastas-Cantos, K, Konarev, P V., Hajizadeh, NR, Kikhney, AG, Petoukhov, M V., Molodenskiy, DS, Panjkovich, A, Mertens, HDT, Gruzinov, A, Borges, C, *et al.* (2021). ATSAS 3.0: Expanded functionality and new tools for small-angle scattering data analysis. J Appl Crystallogr 54, 343–355.

Marttinen, M, Kurkinen, KM, Soininen, H, Haapasalo, A, and Hiltunen, M (2015). Synaptic dysfunction and septin protein family members in neurodegenerative diseases. Mol Neurodegener 10, 16.

Maurer-Stroh, S, Debulpaep, M, Kuemmerer, N, Lopez de la Paz, M, Martins, IC, Reumers, J, Morris, KL, Copland, A, Serpell, L, Serrano, L, *et al.* (2010). Exploring the sequence determinants of amyloid structure using position-specific scoring matrices. Nat Methods 7, 237–242.

McMurray, MA (2016). Assays for genetic dissection of septin filament assembly in yeast, from de novo folding through polymerization. Methods Cell Biol 136, 99–116.

McMurray, MA, Bertin, A, Garcia, G, 3rd, Lam, L, Nogales, E, and Thorner, J (2011). Septin filament formation is essential in budding yeast. Dev Cell 20, 540–549.

McMurray, MA, and Thorner, J (2019). Turning it inside out: The organization of human septin heterooligomers. Cytoskelet Hoboken NJ 76, 449–456.

McQuilken, M, Jentzsch, MS, Verma, A, Mehta, SB, Oldenbourg, R, and Gladfelter, AS (2017). Analysis of Septin Reorganization at Cytokinesis Using Polarized Fluorescence Microscopy. Front Cell Dev Biol 5, 42.

Mendonça, DC, Macedo, JN, Guimarães, SL, Barroso da Silva, FL, Cassago, A, Garratt, RC, Portugal, RV, and Araujo, APU (2019). A revised order of subunits in mammalian septin complexes. Cytoskelet Hoboken NJ.

Mendonça, DC, Morais, STB, Ciol, H, Pinto, APA, Leonardo, DA, Pereira, HD, Valadares, NF, Portugal, RV, Klaholz, BP, Garratt, RC, *et al.* (2024). Structural Insights into Ciona intestinalis Septins: Complexes Suggest a Mechanism for Nucleotide-dependent Interfacial Cross-talk. J Mol Biol 436, 168693.

Micsonai, A, Wien, F, Murvai, N, Nyiri, MP, Balatoni, B, Lee, Y-H, Molnár, T, Goto, Y, Jamme, F, and Kardos, J (2025). BeStSel: analysis site for protein CD spectra-2025 update. Nucleic Acids Res 53, W73–W83.

Miura, F, Kawaguchi, N, Yoshida, M, Uematsu, C, Kito, K, Sakaki, Y, and Ito, T (2008). Absolute quantification of the budding yeast transcriptome by means of competitive PCR between genomic and complementary DNAs. BMC Genomics 9, 574.

Mostowy, S, and Cossart, P (2012). Septins: the fourth component of the cytoskeleton. Nat Rev Mol Cell Biol 13, 183–194.

Nilsson, J, Weis, K, and Kjems, J (2002). The C-terminal extension of the small GTPase Ran is essential for defining the GDP-bound form. J Mol Biol 318, 583–593.

Ong, K, Wloka, C, Okada, S, Svitkina, T, and Bi, E (2014). Architecture and dynamic remodelling of the septin cytoskeleton during the cell cycle. Nat Commun 5, 5698.

Pissuti Damalio, JC, Garcia, W, Alves Macêdo, JN, de Almeida Marques, I, Andreu, JM, Giraldo, R, Garratt, RC, and Ulian Araújo, AP (2012). Self assembly of human septin 2 into amyloid filaments. Biochimie 94, 628–636.

Rambo, RP, and Tainer, JA (2013). Accurate assessment of mass, models and resolution by small-angle scattering. Nature 496, 477–481.

Sala, FA, Valadares, NF, Macedo, JNA, Borges, JC, and Garratt, RC (2016). Heterotypic Coiled-Coil Formation is Essential for the Correct Assembly of the Septin Heterofilament. Biophys J 111, 2608–2619.

Schaefer, RM, Heasley, LR, Odde, DJ, and McMurray, MA (2016). Kinetic partitioning during de novo septin filament assembly creates a critical G1 “window of opportunity” for mutant septin function. Cell Cycle Georget Tex, 0.

Schindelin, J, Arganda-Carreras, I, Frise, E, Kaynig, V, Longair, M, Pietzsch, T, Preibisch, S, Rueden, C, Saalfeld, S, Schmid, B, *et al.* (2012). Fiji: an open-source platform for biological-image analysis. Nat Methods 9, 676–682.

Schirmer, EC, Homann, OR, Kowal, AS, and Lindquist, S (2004). Dominant gain-of-function mutations in Hsp104p reveal crucial roles for the middle region. Mol Biol Cell 15, 2061–2072.

Schneidman-Duhovny, D, Hammel, M, Tainer, JA, and Sali, A (2016). FoXS, FoXSDock and MultiFoXS: Single-state and multi-state structural modeling of proteins and their complexes based on SAXS profiles. Nucleic Acids Res 44, W424-429.

Scott, KL, Halfmann, CT, Hoefakker, AD, Purkayastha, P, Wang, TC, Lele, TP, and Roux, KJ (2024). Nucleocytoplasmic transport rates are regulated by cellular processes that modulate GTP availability. J Cell Biol 223, e202308152.

Sellin, ME, Holmfeldt, P, Stenmark, S, and Gullberg, M (2011a). Microtubules support a disk-like septin arrangement at the plasma membrane of mammalian cells. Mol Biol Cell 22, 4588–4601.

Sellin, ME, Sandblad, L, Stenmark, S, and Gullberg, M (2011b). Deciphering the rules governing assembly order of mammalian septin complexes. Mol Biol Cell 22, 3152–3164.

Sellin, ME, Stenmark, S, and Gullberg, M (2012). Mammalian SEPT9 isoforms direct microtubule-dependent arrangements of septin core heteromers. Mol Biol Cell 23, 4242–4255.

Sellin, ME, Stenmark, S, and Gullberg, M (2014). Cell type-specific expression of SEPT3-homology subgroup members controls the subunit number of heteromeric septin complexes. Mol Biol Cell 25, 1594–1607.

Seufert, W, and Jentsch, S (1992). In vivo function of the proteasome in the ubiquitin pathway. EMBO J 11, 3077–3080.

Shen, C-HH, Komi, Y, Nakagawa, Y, Kamatari, YO, Nomura, T, Kimura, H, Shida, T, Burke, J, Tamai, S, Ishida, Y, *et al.* (2024). Exposed Hsp70-binding site impacts yeast Sup35 prion disaggregation and propagation. Proc Natl Acad Sci U S A 121, e2318162121.

Shorter, J, and Lindquist, S (2004). Hsp104 Catalyzes Formation and Elimination of Self-Replicating Sup35 Prion Conformers. Science 304, 1793–1797.

Shorter, J, and Southworth, DR (2019). Spiraling in Control: Structures and Mechanisms of the Hsp104 Disaggregase. Cold Spring Harb Perspect Biol 11, a034033.

Sikorski, RS, and Hieter, P (1989). A system of shuttle vectors and yeast host strains designed for efficient manipulation of DNA in Saccharomyces cerevisiae. Genetics 122, 19–27.

Sirajuddin, M, Farkasovsky, M, Hauer, F, Kühlmann, D, Macara, IG, Weyand, M, Stark, H, and Wittinghofer, A (2007). Structural insight into filament formation by mammalian septins. Nature 449, 311–315.

Sirajuddin, M, Farkasovsky, M, Zent, E, and Wittinghofer, A (2009). GTP-induced conformational changes in septins and implications for function. Proc Natl Acad Sci U S A 106, 16592–16597.

Sopko, R, Huang, D, Preston, N, Chua, G, Papp, B, Kafadar, K, Snyder, M, Oliver, SG, Cyert, M, Hughes, TR, *et al.* (2006). Mapping pathways and phenotypes by systematic gene overexpression. Mol Cell 21, 319–330.

Soroor, F, Kim, MS, Palander, O, Balachandran, Y, Collins, RF, Benlekbir, S, Rubinstein, JL, and Trimble, WS (2021). Revised subunit order of mammalian septin complexes explains their in vitro polymerization properties. Mol Biol Cell 32, 289–300.

Stein, KC, Kriel, A, and Frydman, J (2019). Nascent Polypeptide Domain Topology and Elongation Rate Direct the Cotranslational Hierarchy of Hsp70 and TRiC/CCT. Mol Cell 75, 1117-1130.e5.

Svergun, DI (1999). Restoring low resolution structure of biological macromolecules from solution scattering using simulated annealing. Biophys J 76, 2879–2886.

Swaney, DL, Beltrao, P, Starita, L, Guo, A, Rush, J, Fields, S, Krogan, NJ, and Villén, J (2013). Global analysis of phosphorylation and ubiquitylation cross-talk in protein degradation. Nat Methods 10, 676–682.

Sweeny, EA, Jackrel, ME, Go, MS, Sochor, MA, Razzo, BM, DeSantis, ME, Gupta, K, and Shorter, J (2015). The Hsp104 N-terminal domain enables disaggregase plasticity and potentiation. Mol Cell 57, 836–849.

Szczepaniak, K, Bukala, A, da Silva Neto, AM, Ludwiczak, J, and Dunin-Horkawicz, S (2021). A library of coiled-coil domains: from regular bundles to peculiar twists. Bioinforma Oxf Engl 36, 5368–5376.

Takagi, J, Cho, C, Duvalyan, A, Yan, Y, Halloran, M, Hanson-Smith, V, Thorner, J, and Finnigan, GC (2021). Reconstructed evolutionary history of the yeast septins Cdc11 and Shs1. G3 Bethesda Md 11.

Testa, OD, Moutevelis, E, and Woolfson, DN (2009). CC+: a relational database of coiled-coil structures. Nucleic Acids Res 37, D315-322.

Touati, SA, Hofbauer, L, Jones, AW, Snijders, AP, Kelly, G, and Uhlmann, F (2019). Cdc14 and PP2A Phosphatases Cooperate to Shape Phosphoproteome Dynamics during Mitotic Exit. Cell Rep 29, 2105-2119.e4.

Tria, G, Mertens, HDT, Kachala, M, and Svergun, DI (2015). Advanced ensemble modelling of flexible macromolecules using X-ray solution scattering. IUCrJ 2, 207–217.

Tsanov, N, Samacoits, A, Chouaib, R, Traboulsi, A-M, Gostan, T, Weber, C, Zimmer, C, Zibara, K, Walter, T, Peter, M, *et al.* (2016). smiFISH and FISH-quant - a flexible single RNA detection approach with super-resolution capability. Nucleic Acids Res 44, e165.

Tully, MD, Tarbouriech, N, Rambo, RP, and Hutin, S (2021). Analysis of sec-saxs data via efa deconvolution and scatter. J Vis Exp 2021.

Velculescu, VE, Zhang, L, Zhou, W, Vogelstein, J, Basrai, MA, Bassett, DE, Hieter, P, Vogelstein, B, and Kinzler, KW (1997). Characterization of the yeast transcriptome. Cell 88, 243–251.

Versele, M, Gullbrand, B, Shulewitz, MJ, Cid, VJ, Bahmanyar, S, Chen, RE, Barth, P, Alber, T, and Thorner, J (2004). Protein-protein interactions governing septin heteropentamer assembly and septin filament organization in Saccharomyces cerevisiae. Mol Biol Cell 15, 4568–4583.

Versele, M, and Thorner, J (2004). Septin collar formation in budding yeast requires GTP binding and direct phosphorylation by the PAK, Cla4. J Cell Biol 164, 701–715.

Vetter, IR, Nowak, C, Nishimoto, T, Kuhlmann, J, and Wittinghofer, A (1999). Structure of a Ran-binding domain complexed with Ran bound to a GTP analogue: implications for nuclear transport. Nature 398, 39–46.

Volkov, V V., and Svergun, DI (2003). Uniqueness of ab initio shape determination in small-angle scattering. J Appl Crystallogr 36, 860–864.

Vrabioiu, AM, Gerber, SA, Gygi, SP, Field, CM, and Mitchison, TJ (2004). The majority of the Saccharomyces cerevisiae septin complexes do not exchange guanine nucleotides. J Biol Chem 279, 3111–3118.

Vrabioiu, AM, and Mitchison, TJ (2006). Structural insights into yeast septin organization from polarized fluorescence microscopy. Nature 443, 466–469.

Wang, H-Y, Chen, K-R, Yeh, B-C, Li, W-D, Wu, S-R, Ching, Y-H, Wang, C-Y, and Kuo, P-L (2025). SEPT14 complexes maintain sperm morphogenesis and function. FASEB J Off Publ Fed Am Soc Exp Biol 39, e70414.

Weems, AD, Johnson, CR, Argueso, JL, and McMurray, MA (2014). Higher-Order Septin Assembly Is Driven by GTP-Promoted Conformational Changes: Evidence From Unbiased Mutational Analysis in Saccharomyces cerevisiae. Genetics 196, 711–727.

Weems, AD, and McMurray, MA (2017). The step-wise pathway of septin hetero-octamer assembly in budding yeast. eLife 6.

Winzeler, EA, Shoemaker, DD, Astromoff, A, Liang, H, Anderson, K, Andre, B, Bangham, R, Benito, R, Boeke, JD, Bussey, H, *et al.* (1999). Functional Characterization of the S. cerevisiae Genome by Gene Deletion and Parallel Analysis. Science 285, 901–906.

Woods, BL, Cannon, KS, Vogt, EJD, Crutchley, JM, and Gladfelter, AS (2021). Interplay of septin amphipathic helices in sensing membrane-curvature and filament bundling. Mol Biol Cell 32, br5.

Woolfson, DN (2023). Understanding a protein fold: The physics, chemistry, and biology of α-helical coiled coils. J Biol Chem 299, 104579.

Zeraik, AE, Pereira, HM, Santos, YV, Brandão-Neto, J, Spoerner, M, Santos, MS, Colnago, LA, Garratt, RC, Araújo, APU, and Demarco, R (2014). Crystal Structure of a Schistosoma mansoni Septin Reveals the Phenomenon of Strand Slippage in Septins Dependent on the Nature of the Bound Nucleotide. J Biol Chem 289, 7799–7811.

Zhang, Y, Gao, J, Chung, KK, Huang, H, Dawson, VL, and Dawson, TM (2000). Parkin functions as an E2-dependent ubiquitin- protein ligase and promotes the degradation of the synaptic vesicle-associated protein, CDCrel-1. Proc Natl Acad Sci U S A 97, 13354–13359.

Zhu, Y-C, Wang, W-X, Li, X-L, Xu, C-W, Chen, G, Zhuang, W, Lv, T, and Song, Y (2019). Identification of a Novel Icotinib-Sensitive EGFR-SEPTIN14 Fusion Variant in Lung Adenocarcinoma by Next-Generation Sequencing. J Thorac Oncol Off Publ Int Assoc Study Lung Cancer 14, e181–e183.

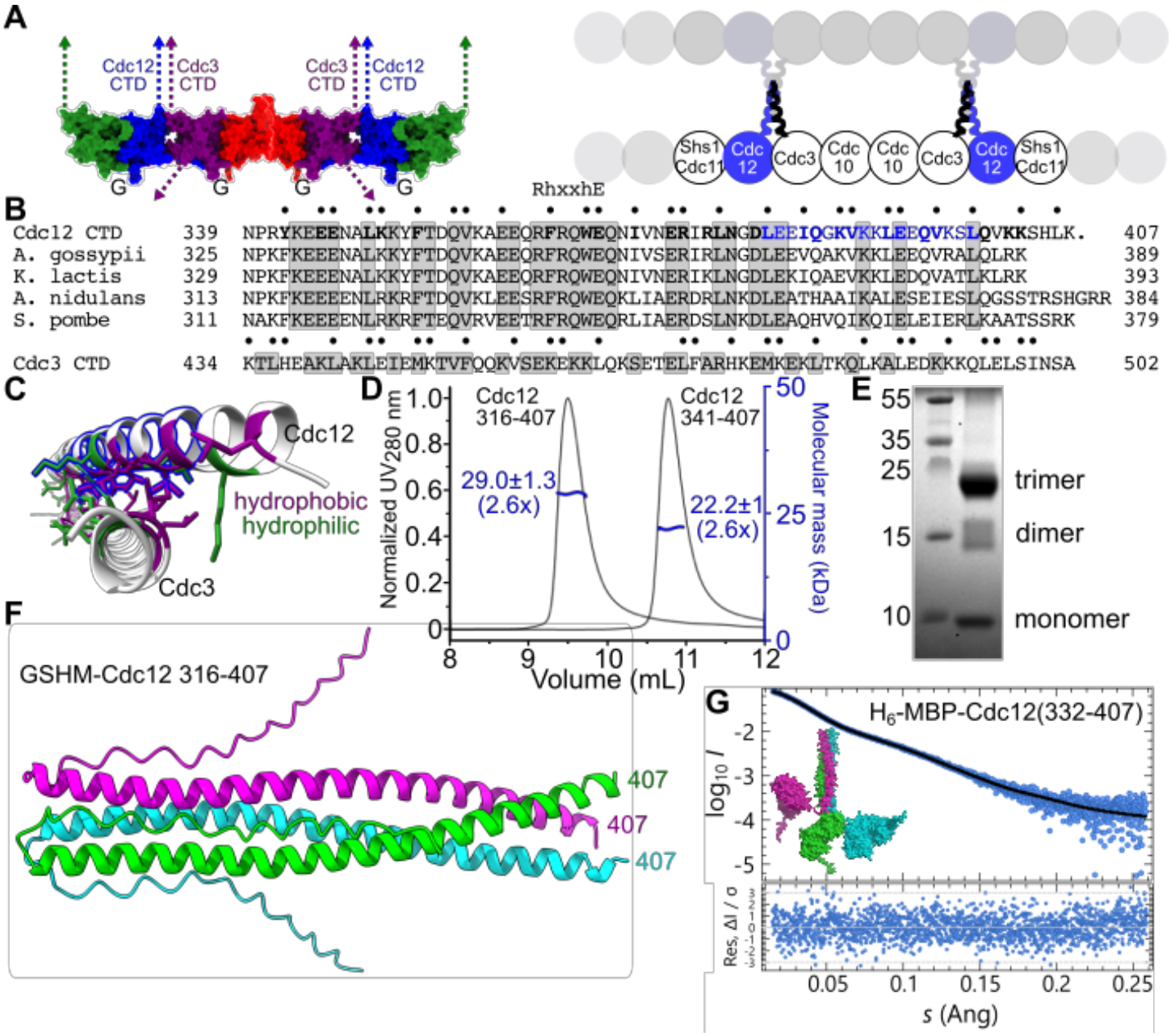

Figure 1. Homotrimerization of the Cdc12 C-terminal domain.
(A) Schematic illustration of budding yeast septin hetero-octamer and filament organization focusing on putative roles for coiled coils formed by the C-terminal domains of Cdc3 and Cdc12. At left is a model of the septin hetero-octamer from *S. cerevisiae* based on the crystal structure of a Shs1–Cdc12–Cdc3–Cdc10 hetero-tetramer lacking the extended N- and C-terminal domains (PDB 8PFH (Grupp *et al.*, 2024)). The missing domains are illustrated as dashed arrows. "CTD", C-terminal domain; "G", so-called G interface between septins. The cartoon at right shows end-on-end hetero-octamer polymerization and also the putative four-helix coiled coils that have been proposed to mediate lateral pairing of adjacent filaments (Bertin *et al.*, 2008).
(B) Sequence alignment of the Cdc12 CTD from *S. cerevisiae* with homologs from other fungal species, with the sequence of the Cdc3 CTD shown below. Gray shading indicates identity among all five species (other Cdc3 sequences are not shown). Bullet points above residues indicate those that are predicted to make contacts in a heterodimeric Cdc3–Cdc12 coiled coil. Bold residues are predicted to make contacts in a homotrimeric Cdc12 coiled coil. The "RhxxhE" motif known to mediate homotrimerization in non-septin coiled coils (Kammerer *et al.*, 2005) is also indicated above the sequence in Cdc12 that matches this motif. Blue residues comprise the amphipathic helix that is necessary and sufficient for the curvature preference of membrane binding by yeast hetero-octamers (Cannon *et al.*, 2019; Woods *et al.*, 2021).

(C) The heterodimeric Cdc3–Cdc12 coiled coil as predicted by AlphaFold3, showing Cdc3 residues 434-503 and Cdc12 residues 339-406 and the hydrophobic (isoleucine, leucine, methionine, phenylalanine, tryptophan, and valine, in purple) and charged/hydrophilic (arginine, aspartate, glutamate, lysine, in green) side chains that make predicted contacts. The blue outline indicates the residues of the Cdc12 amphipathic helix that are predicted to interact with the inner leaflet of the plasma membrane.
(D) SEC-MALS analysis of purified Cdc12 CTD at 300 µM. Both purified versions also include the residual thrombin cleavage sequence GSHM at the N terminus. Blue values show MALS-derived molecular mass and, in parenthesis, the relative mass compared to the monomer. SEC indicates non-resolved peaks corresponding to a mixture of dimers and trimers. Buffer employed was 50 mM Tris, 300 mM NaCl, pH 8.0 and protein concentration at injection was 0.3 mM.
(E) SDS-PAGE analysis of the smaller Cdc12 CTD fragment (341-407, 9.3 kDa monomeric mass) following crosslinking with BS3. Left lane contains molecular weight standards (Promega Broad Range Marker); values indicate band masses. Labels indicate presumed identity of the Cdc12 CTD bands.
(F) AlphaFold3 prediction of trimers of the Cdc12 CTD (residues 316-407) where residue 407 is labeled, and including the four residues (GSHM) left from protease cleavage during purification.
(G) EOM-NNLSJOE fit and residuals of the SAXS dataset representing the top of the SEC elution peak of MBP-Cdc12CC+8 using parallel dimers and trimers. Inset, model of the most abundant species (27%).

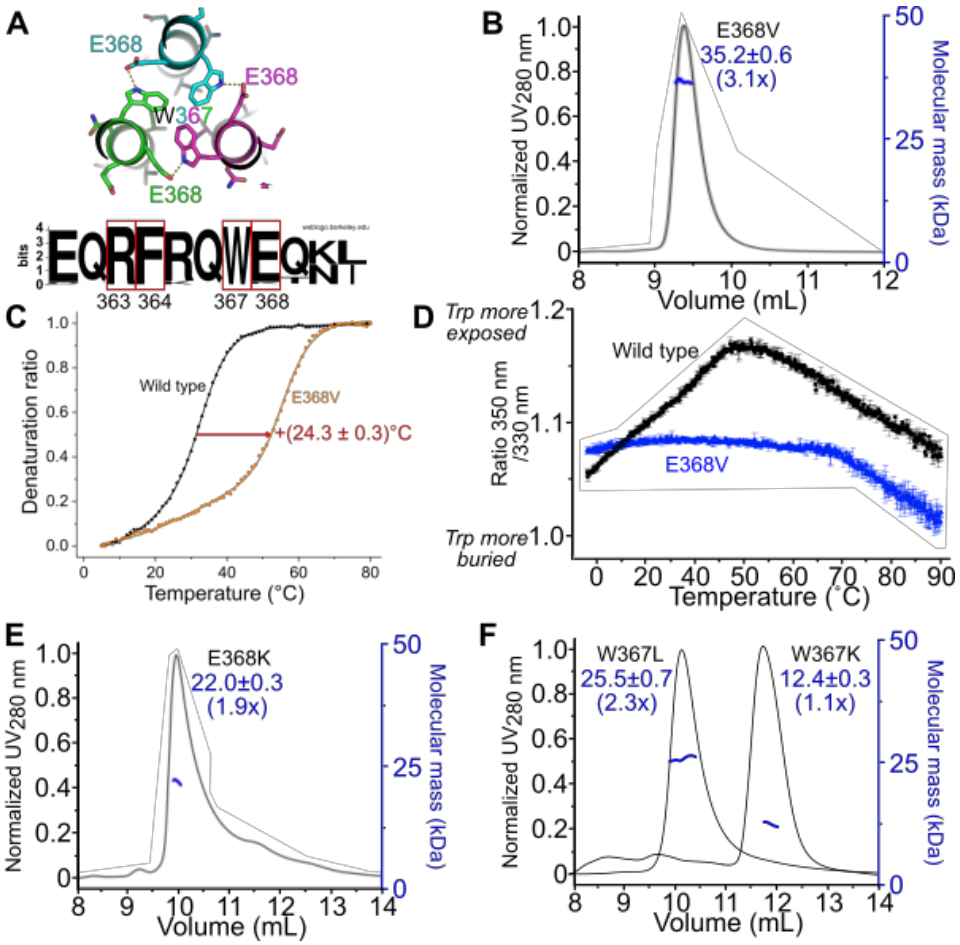

Figure 2. Mutations in a conserved homotrimerization motif within the Cdc12 C-terminal domain alter coiled-coil oligomerization
(A) The W367 environment within the predicted Cdc12 CTD homotrimeric coiled coil, and sequence logo of the neighbouring residues, highlighting R363, F364, W367 and E368, the residues that match the RhxxhE homotrimerization motif.
(B) As in Fig.1D, SEC-MALS analysis of purified Cdc12 CTD with the E368V mutation.

(C) Circular dichroism denaturation transitions monitored at 222 nm of wild type (black) or E368V mutant (orange) Cdc12 CTD at 10 µM. The red arrow indicates the difference in temperature for which 50% of the protein was denatured.
(D) NanoDSF analysis of the intrinsic fluorescence intensity ratio (350/330 nm) of wild type (black) or E368V mutant (blue) at 90 µM over the indicated temperature range during unfolding. Error bars represent standard deviation from duplicate measurements. As W367 is the sole tryptophan in Cdc12 CTD and there are only two tyrosines, the signals acquired predominantly report on W367.
(E-F) As in (B), SEC-MALS analysis of purified Cdc12 CTD with the indicated mutations.

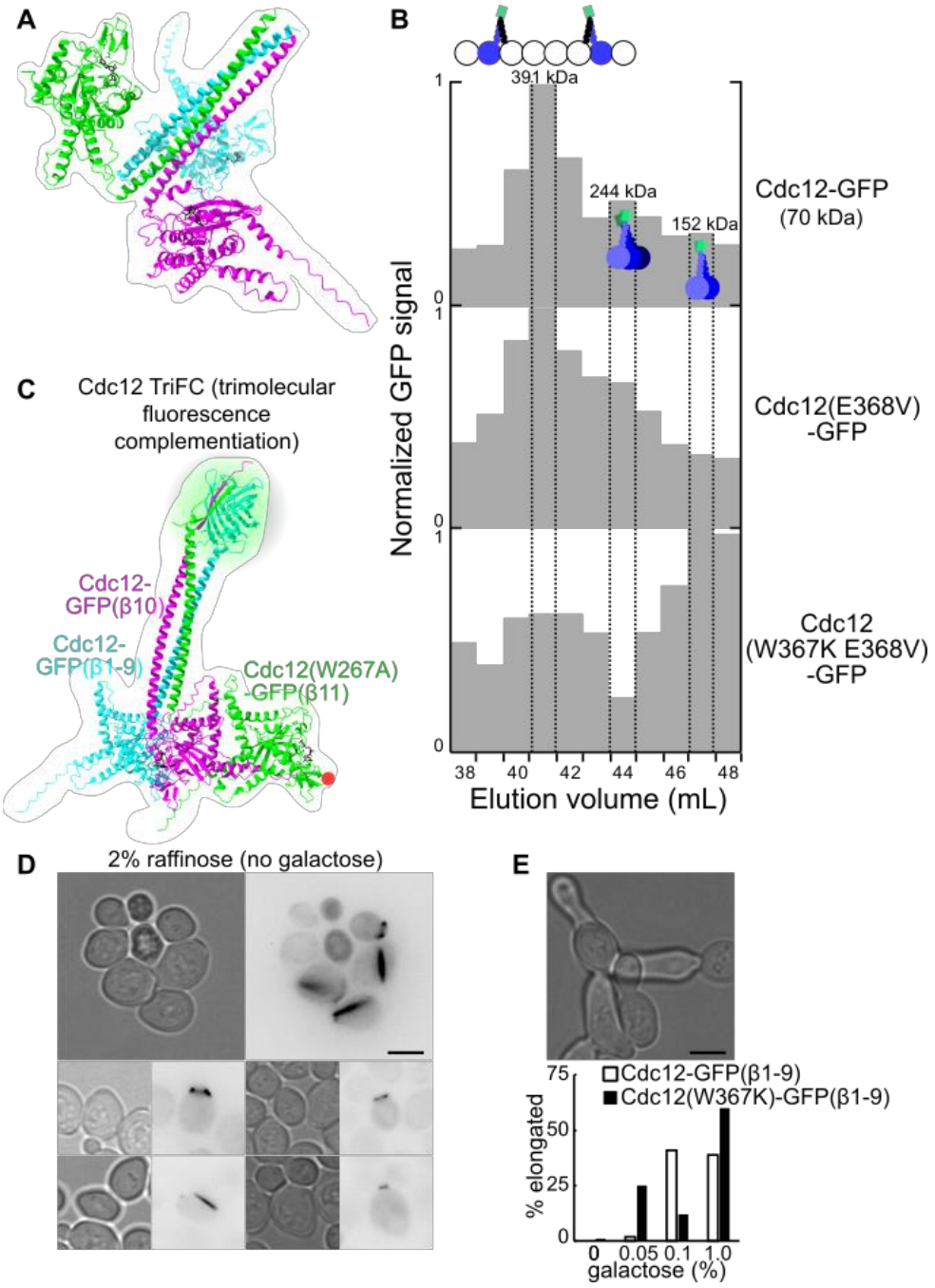

Figure 3. Homo-oligomerization in vivo by excess Cdc12 molecules.
(A) Top-ranked AlphaFold3 prediction for homotrimer of full-length Cdc12 bound to GDP.
(B) SEC analysis of lysates of wild-type yeast cells (strain BY4741) overexpressing the indicated version of C-terminally GFP-tagged Cdc12. Plotted are the relative amount of Cdc12-GFP in each 1-mL elution fraction as

determined by dot blotting and detection with anti-GFP antibody and fluorescently labeled anti-GFP antibodies. Fluorescence for each dot was normalized to the signal from the dot from that sample with the highest signal. The dashed lines outline fractions corresponding to the three apparent peaks; values given above each peak indicate the largest size in kDa of molecules expected in that fraction, based on calibration of the column with molecular weight standards (Fig. S7). Cartoons indicate the Cdc12-containing septin complex that each peak likely represents, based on a monomeric Cdc12-GFP size of 70 kDa, with the largest complex being a septin hetero-octamer. Green squares represent GFP. Plasmids were pMVB2 ("Cdc12-GFP"), BD7C264E ("Cdc12(E368V)-GFP"), and 9F2B6E98 ("Cdc12(W367K E368V)-GFP").

(C) Schematic of trimolecular fluorescence complementation (TriFC) assay to detect Cdc12 homotrimerization in vivo. Ribbon diagram shows top-ranked AlphaFold3 prediction for the complex formed by three C-terminal fusions of GFP fragments to Cdc12. Note that the Cdc12-GFP(β11) fusion harbors the W267A mutation (highlighted in red) to inhibit interactions between the Cdc12 GTPase domains.

(D) Representative micrographs of TriFC signal detected in diploid yeast cells (strain BY4743) grown in medium with 2% raffinose (0% galactose) and selective for the plasmids encoding the three fusions, which were D2AC2EB4 ("Cdc12-GFP(β1-9)"), 76068B19 ("Cdc12-GFP(β10)"), and E2438448 ("Cdc12(W267A)-GFP(β11)"). Scale bar, 5 µm.

(E) Top, example elongated cells. Below, the percentage among 100 cells analyzed per sample that were elongated (length to width ratio >2, a symptom of septin dysfunction) within cultures with the indicated galactose concentration and expressing Cdc12-GFP(β10), Cdc12(W267A)-GFP(β11), and either wild-type Cdc12-GFP(β1-9) or, as indicated, a derivative carrying Cdc12 mutation W367K (from plasmid 15C00ABB).

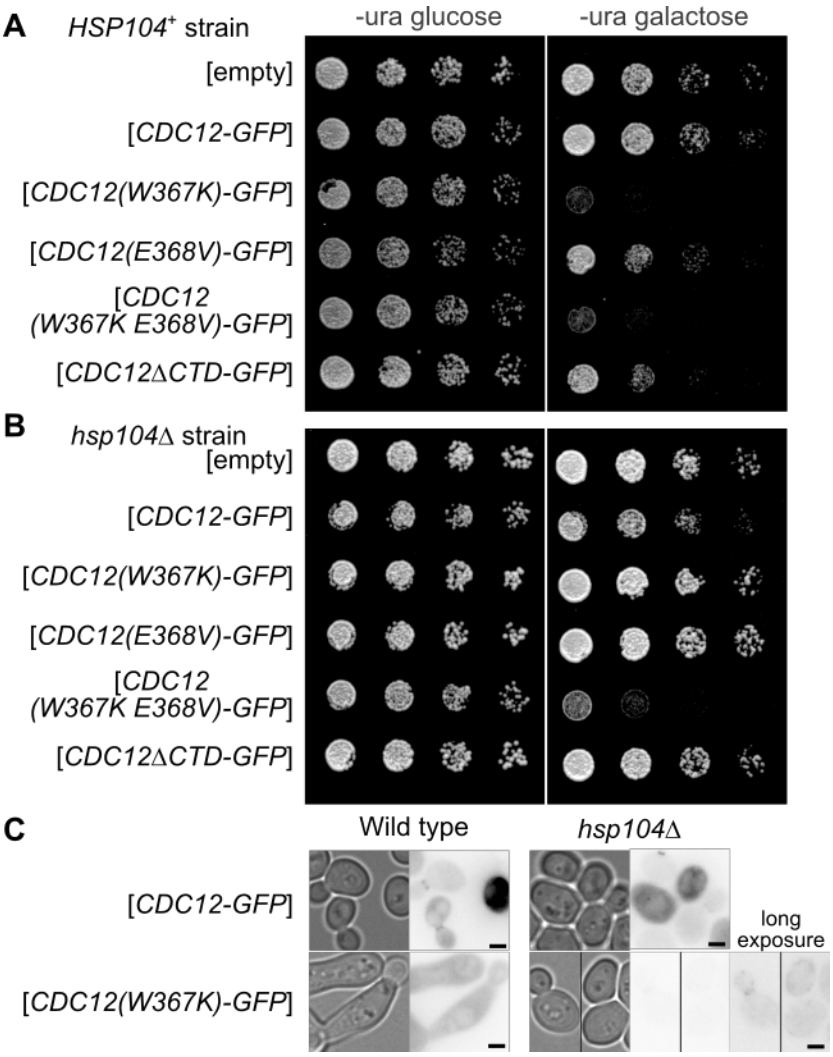

Figure 4. Dominant inhibition of septin function by C-terminal domain homo-oligomerization mutants of the septin Cdc12

(A) Five-fold serial dilutions of yeast cells (strain BY4741) were spotted on medium selective for the indicated *URA3*-marked plasmid and either repressing ("-ura glucose") or inducing ("-ura galactose") expression of the indicated version of GFP-tagged Cdc12 or the empty vector pRS316. *CDC12* plasmids were pMVB2 ("*CDC12-GFP*"), C6F1B99E ("*CDC12(W367K)-GFP*"), (BD7C264E ("*CDC12(E368V)-GFP*"), 9F2B6E98 ("*CDC12(W367K E368V)-GFP*"), and pMVB160 ("*CDC12ΔCTD-GFP*"). Plates were imaged after 2 days incubation at 30˚C.

(B) As in (A) but with the *hsp104*Δ yeast strain JTY4013.

(C) Micrographs of representative cells scraped from the galactose plates in (A) and (B) and imaged by transmitted light or the GFP cube (60-msec exposure). "Long exposure" indicates a 250-msec exposure. Scale bars, 2 µm.

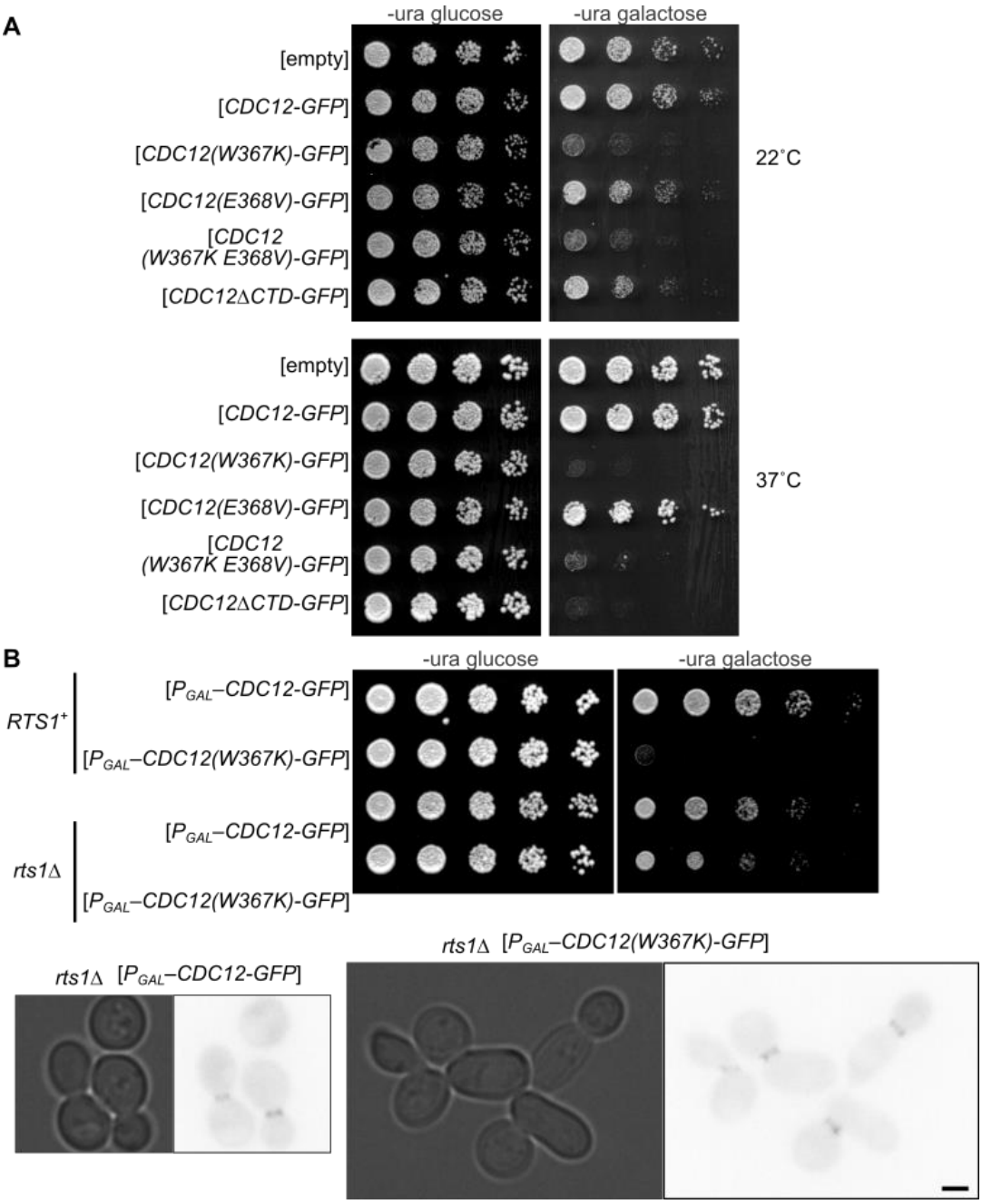

Figure 5. The PP2A phosphatase subunit Rts1 is required for dominant inhibition of septin function by C-terminal domain homo-oligomerization mutants of the septin Cdc12

(A) As in Fig. 4A but at the indicated temperatures.

(B) Top, as in (A), dilution series of wild-type (strain BY4741) or *rts1*Δ (strain H06957) cells carrying plasmids encoding the indicated Cdc12-GFP fusion under control of the galactose-inducible *GAL1/10* promoter. Plasmids were pMVB2 ("*CDC12-GFP*") or C6F1B99E ("*CDC12(W367K)-GFP*"). Bottom, cells were scraped from colonies on the galactose plates in (A), suspended in water, and imaged by transmitted light or the GFP cube (60-msec exposure). Scale bar is 2 µm.

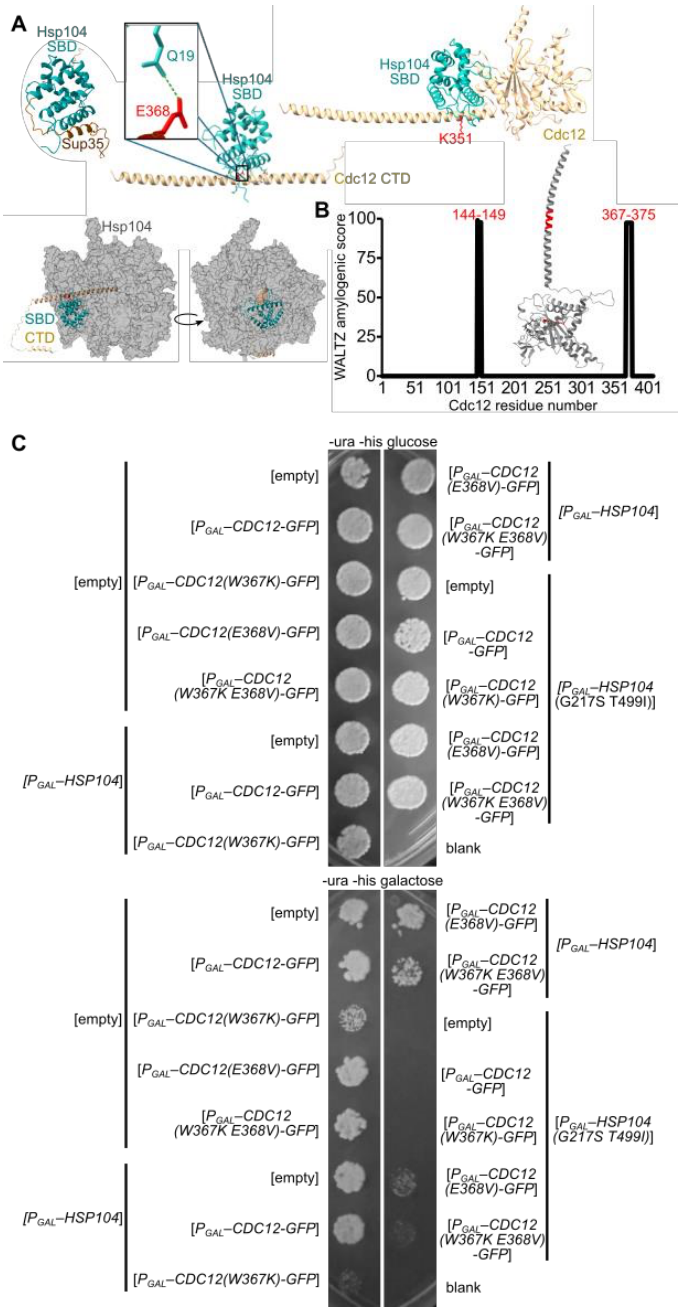

Figure 6. Evidence for direct Hsp104 binding to E368 in the Cdc12 C-terminal domain

(A) Top-ranked AlphaFold3 predictions for binding of the substrate-binding domain ("SBD") of Hsp104 (residues 1-152) to the known substrate Sup35 (residues 96-151), the Cdc12 CTD (residues 297-407), or full-length Cdc12. Below, the complex of Hsp104 homohexamer bound to Cdc12 CTD was predicted by structurally aligning the Hsp104 SBD–Cdc12 CTD prediction to chain B of a closed-conformation Hsp104 cryo-EM structure (PDB 6N8T).

(B) Left, WALTZ amyloidogenic scores plotted against the sequence of Cdc12. Right, the two regions with high WALTZ scores are colored in red in the top-ranked AlphaFold3 prediction for GDP-bound full-length Cdc12. (C) Serial dilutions were performed as in Fig. 4A of wild-type cells (strain BY4741) on glucose or galactose medium selective for *HIS3*- and *URA3*-marked plasmids, either empty vectors ("[empty]") or encoding the indicated alleles of *HSP104* and *CDC12*, incubated at 30˚C for 2 days before imaging. For the sake of space, only the most concentrated spot in each dilution series is shown. Empty vectors were pRS313 and pRS316, other plasmids were 5679 ("P_{GAL}–*HSP104*"), 5707 ("P_{GAL}–*HSP104(G217S T499I)*"), pMVB2 ("P_{GAL}–*CDC12-GFP*"), C6F1B99E ("P_{GAL}–*CDC12(W367K)-GFP*"), (BD7C264E ("P_{GAL}–*CDC12(E368V)-GFP*"), and 9F2B6E98 ("P_{GAL}–*CDC12(W367K E368V)-GFP*"). No cells were spotted in the "blank" row.

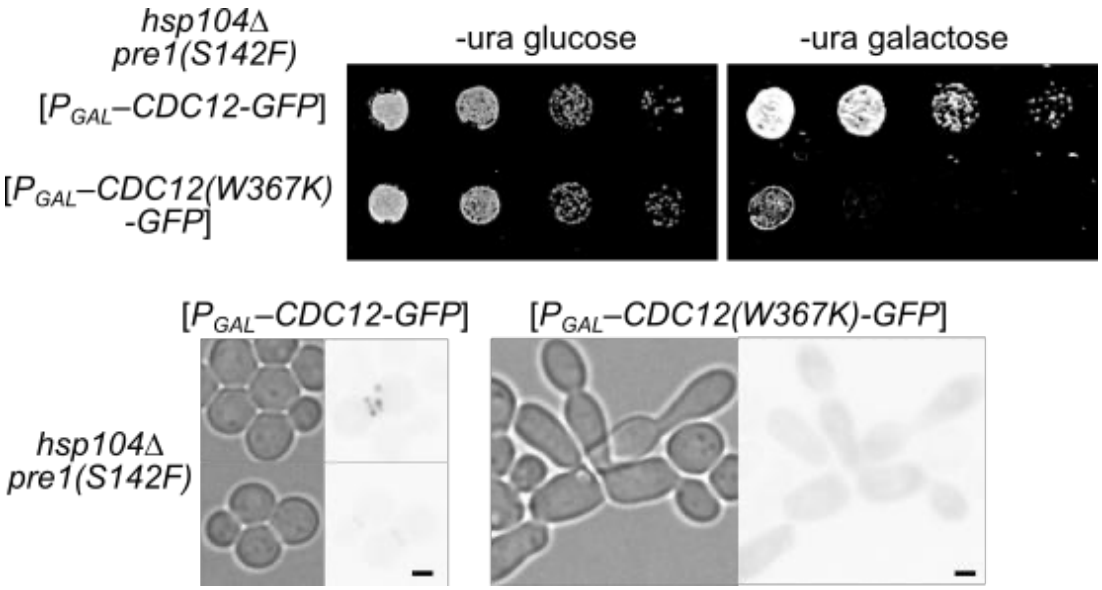

Figure 7. Hsp104 protects monomeric Cdc12 against proteasomal degradation
Top, dilution series as in Fig.4A with the *hsp104Δ pre1(S142F)* yeast strain F93544A5 carrying plasmids pMVB2 ("*CDC12-GFP*") or C6F1B99E ("*CDC12(W367K)-GFP*"). Below, micrographs of representative cells scraped from the galactose plate and imaged with transmitted light or the GFP cube (250-msec exposures). Scale bars, 2 µm.

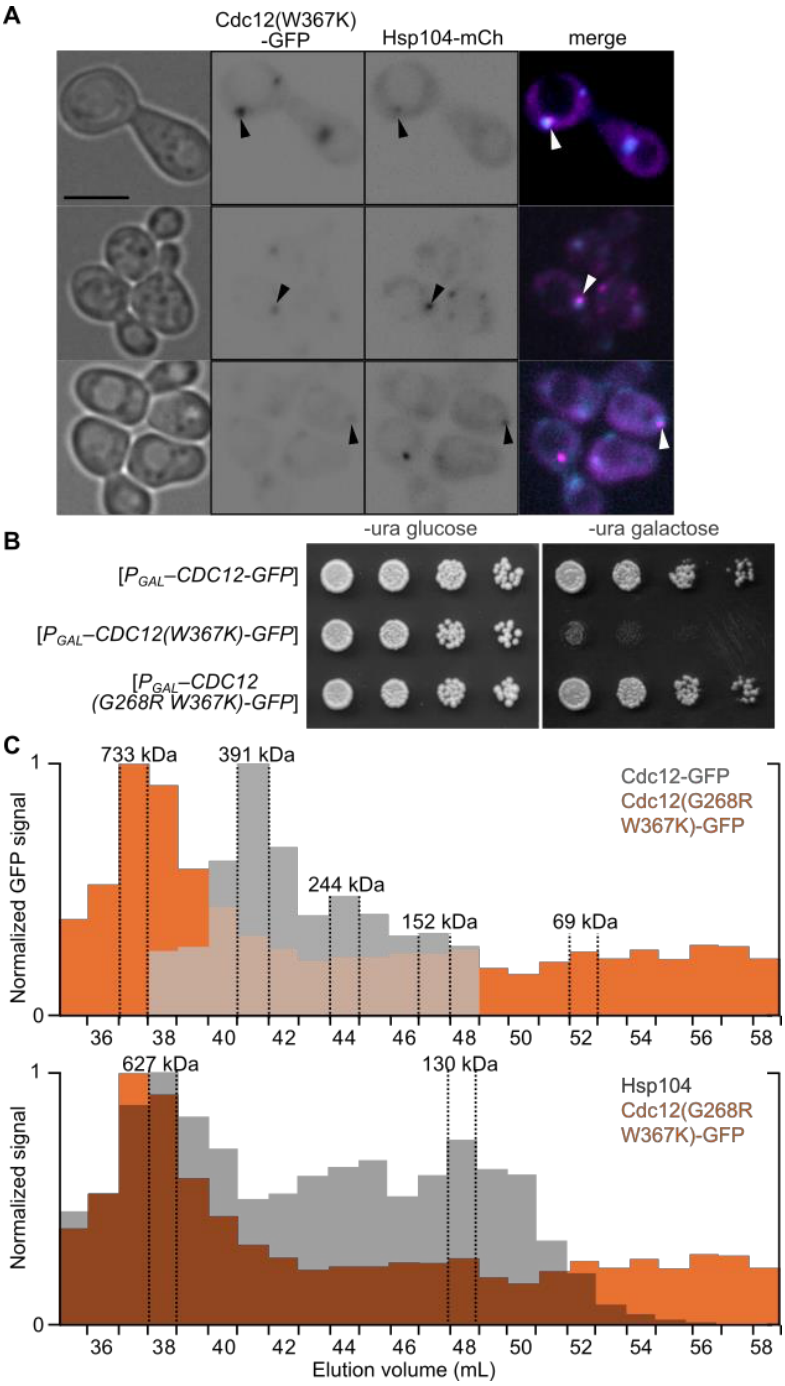

Figure 8. Hsp104 co-localizes and co-elutes with monomeric mutant Cdc12
(A) Representative images of cells of *HSP104-mCherry* strain H06799 carrying Cdc12(W367K)-GFP-expressing plasmid C6F1B99E cultured in selective medium with 2% galactose and imaged with transmitted light (first column of images), the GFP cube (second column, 60-msec exposure), or the Texas Red cube (third column, 250-msec exposure). The fourth column shows false-colored overlay/merge images. Arrowheads point to overlapping foci. Scale bar is 5 µm.
(B) Serial dilutions of cells of strain BY4741 carrying plasmid 1EB21EA6 were spotted on selective medium with 2% glucose or 2% galactose and incubated at 30˚C for 3 days.
(C) As in Fig. 3B, SEC analysis of lysates of cells of strain BY4741 carrying plasmid pMVB2 ("Cdc12-GFP") or YEp-Cdc12(G268R W367K)-GFP ("Cdc12(G268R W367K)-GFP"). Top plot shows results from blotting with anti-GFP antibodies. The data for Cdc12-GFP (gray bars) are the same as in Fig. 3B, in which only fractions 38-48 were analyzed. For the Cdc12(G268R W367K)-GFP lysate, additional fractions were analyzed. kDa values above peaks indicate the calculated molecular weight for the largest molecules in that fraction,

based on molecular weight standards analyzed in a separate SEC run. The 69-kDa fraction is where monomeric Cdc12(W367K)-GFP would be expected to elute. The bottom plot has the same values for GFP detection in the Cdc12(G268R W367K)-GFP lysate (orange) and also includes values for detection of Hsp104 on the same blot using anti-Hsp104 antibodies (dark gray).

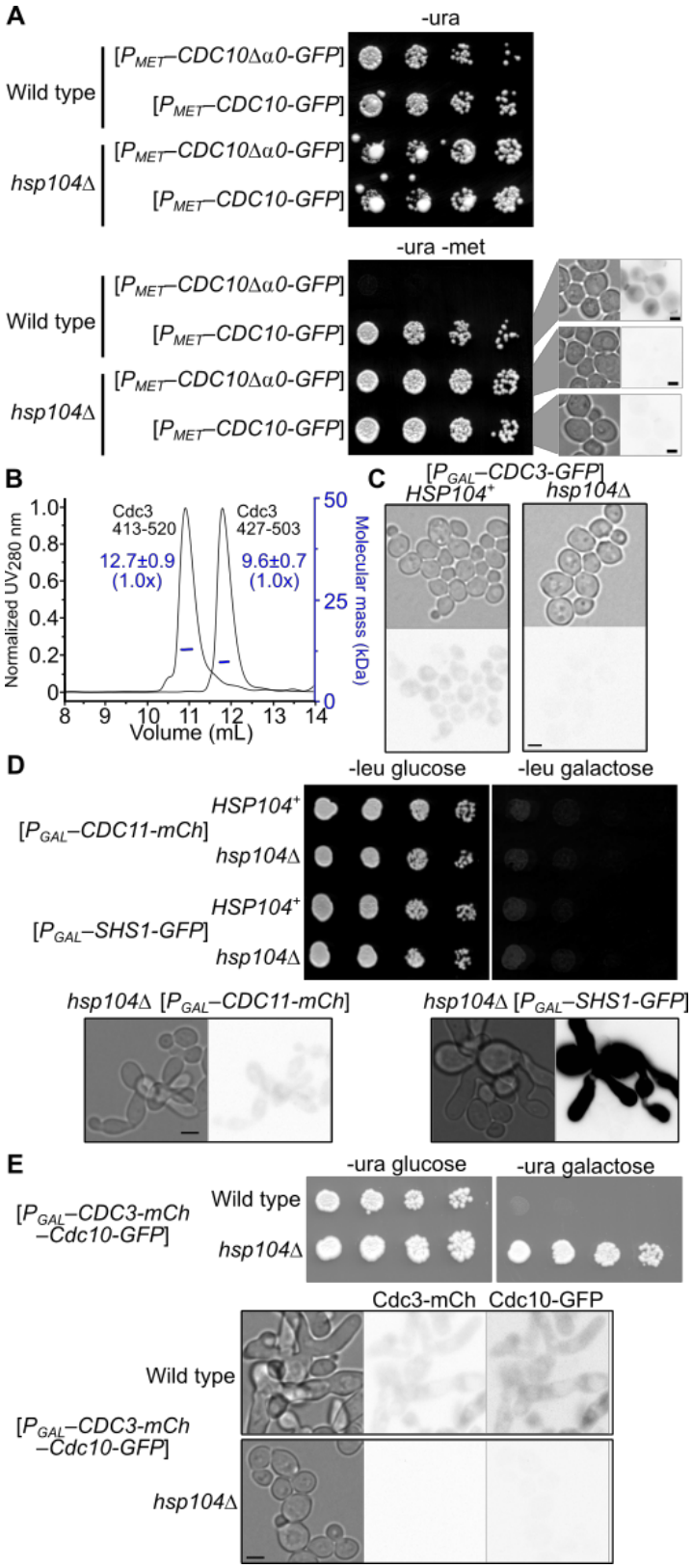

Figure 9. Specific septins require Hsp104 for super-stoichiometric stability

(A) Five-fold serial dilutions of yeast cells were spotted on medium selective for the indicated *URA3*-marked plasmid and either repressing (containing methionine, "-ura") or inducing (lacking methionine, "-ura -met") expression of the indicated tagged septin. Plates were incubated at 30˚C and imaged after 2 days. Micrographs at right show cells scraped from that plate and imaged by transmitted light (left) or with the GFP cube (right, 60-msec exposure). Scale bar is 2 µm. Strains were BY4742 ("Wild type") and JTY4013 ("*hsp104*Δ") and plasmids were pMETp-CDC10-GFP ("P_{MET}–*CDC10-GFP*") and pJT3456 ("P_{MET}–*CDC10*Δ*α0-GFP*").
(B) As in Fig.2B, SEC-MALS analysis of purified Cdc3 CTD. The CTD residues present in the two constructs are indicated.
(C) The same strains as in (A) but carrying plasmid pMVB1 ("P_{GAL}–*CDC3-GFP*") were cultured in medium selective for the plasmid and containing 2% galactose to induce Cdc3-GFP expression. Shown are representative images of cells visualized by transmitted light (left) or with the GFP cube (right, 60-msec exposure). Scale bar is 2 µm.
(D) Top, serial dilution as in (A) but with glucose as the repressor and galactose as the inducer, *LEU2*-marked plasmids pGF-IVL-287 ("P_{GAL}–*CDC11-mCh*") and pGF-IVL-286 ("P_{GAL}–*SHS1-GFP*"), and imaging Cdc11-mCherry (250-msec exposure) or Shs1-GFP (250-msec exposure). Scale bar is 5 µm.
(E) As in (D) but with *URA3*-marked plasmid G01273 and imaging Cdc3-mCherry (250-msec exposure) and Cdc10-GFP (250-msec exposure). Scale bar is 5 µm.

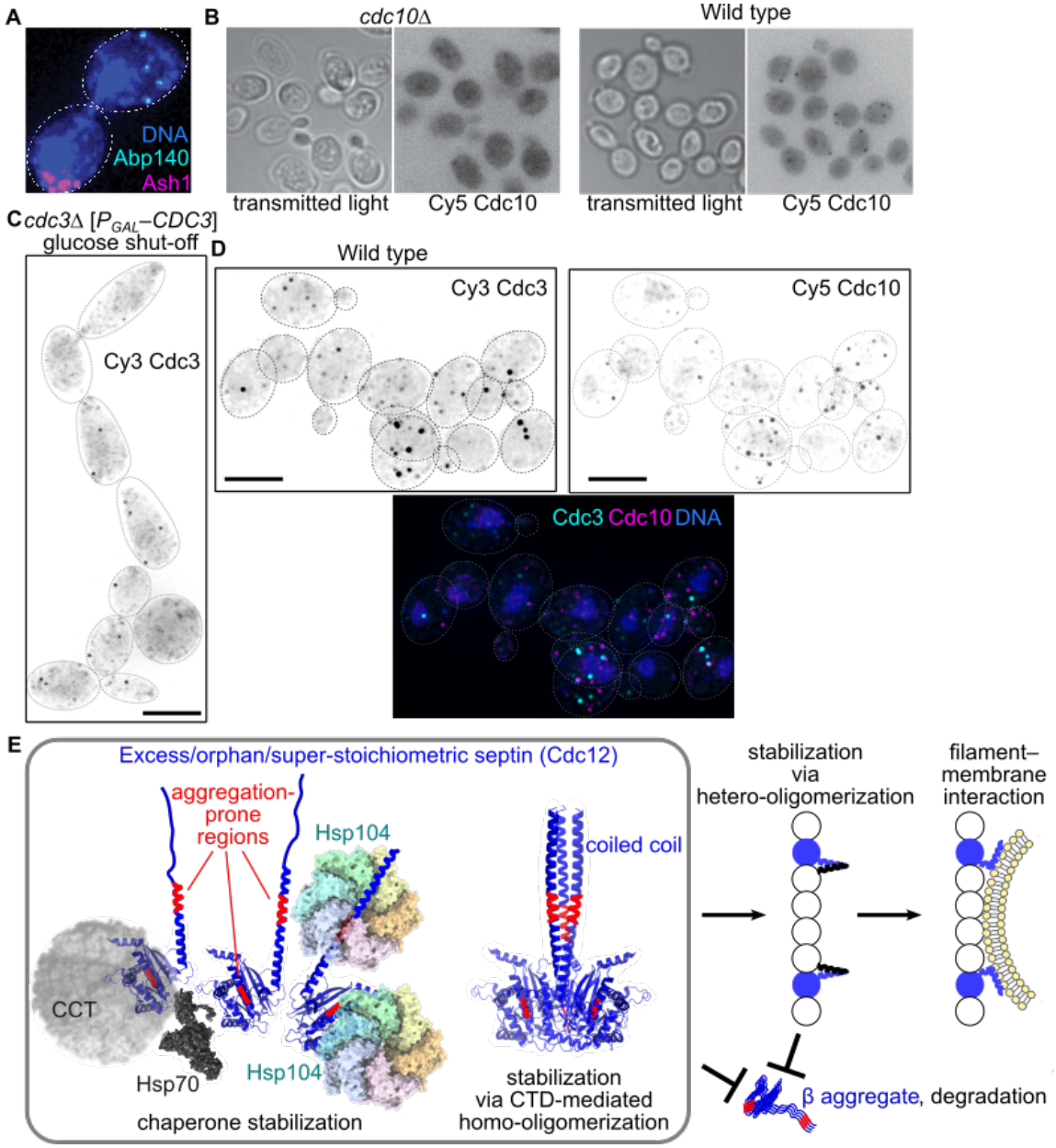

Figure 10. Low, variable numbers of septin-encoding mRNAs per yeast cell
(A) Representative overlay/merge image of smiFISH detection in wild-type (strain BY4743) cells of the mother-cell-localized Abp140 mRNA and the bud-tip-localized Ash1 mRNA, plus DAPI staining of the DNA. Dashed lines outline the cell walls.
(B) SmiFISH with Cy5-labeled Cdc10 probe set, showing transmitted light and Cy5 fluorescence images of negative control (*cdc10*Δ, strain JTY4010) or wild-type (strain BY4743) cells.
(C) Negative control Cdc3 smiFISH. As in (B) but with Cy3-labeled Cdc3 probe set, Cy3 fluorescence detection, and *cdc3*Δ strain MMY0296 carrying plasmid pMVB169 that was cultured in glucose-containing medium to shut off *CDC3* transcription and deplete Cdc3 mRNAs. Faint spots in these cells are interpreted as non-specific signal. Scale bar, 5 µm.
(D) As in (A), Wild-type (strain BY4743) cells were fixed, permeabilized, and labeled with DAPI and the same Cy5-Cdc10 and Cy3-Cdc3 probe sets used in (B) and (C).
(E) Schematic illustration, adapted from Hassell et al., 2022, of the proposed role for CTD-mediated coiled coil homo-oligomerization in the pathway by which excess/orphan molecules of a budding yeast septin (using Cdc12 as an example) assemble post-translationally into hetero-octamers. Two parallel modes of conformational stabilization are shown, one mediated by chaperones and the other by coiled-coil homo-

oligomerization. Hsp104 binds aggregation-prone sequences (red). Both modes prevent aggregation and proteasome-mediated degradation. Co-assembly into a septin hetero-octamer also stabilizes. In the case of Cdc12, hetero-oligomerization requires dissociation of homo-oligomeric coiled coils and assembly of hetero-dimeric coiled coils, which also dissociate when septin filaments interact with the plasma membrane.

Table S1 SEC-SAXS data and analysis.

SASBDB entry	SASDYR4	SASDYS4	SASDYU4	SASDYQ4
Sample	**MBP-Cdc12CC+8**	**MBP-Cdc12CC+8 (peak front)**	**MBP-Cdc12CC+8 (peak tail)**	**MBP-Cdc12CC**
Instrumental				
Instrument and SEC parameters:	beamline, B21 Diamond Light Source; frames, 600 total (one every 3 s); column, Superdex 200 Increase 3.2/300; flow rate, 0.075 ml/min; concentration at injection, 5.0 mg/ml; injection volume, 45 µl; buffer, 50 mM Tris-HCl, 150 mM NaCl, pH 7.5			
Selected frames (total number of frames)	337-350 (14)	345-353 (9)	392-407 (16)	364-373 (10)
Guinier analysis				
$I(0) \pm \sigma$, cm^{-1}	0.0943 ± 0.0001	0.0951 ± 0.0002	0.0252 ± 0.0001	0.0823 ± 0.0002
$R_g \pm \sigma$, Å	47.79 ± 0.09	48.6 ± 0.2	44.2 ± 0.2	44.3 ± 0.2
q_{min} (calculated q_{min} max, π/D_{max}), Å^{-1}	0.0151 (0.0180)	0.0149 (0.0180)	0.0164 (0.0187)	0.0139 (0.0188)
$q.R_g$ max	1.2936	1.2530	1.2945	1.1294
r^2	0.9988	0.9957	0.9904	0.9953
PDDF/*P*(*r*) analysis				
$I(0)$, cm^{-1}	0.0957 ± 0.0001	0.0949 ± 0.0004	0.0256 ± 0.0001	0.0825 ± 0.0002
Real space R_g, Å	49.3 ± 0.2	49.4 ± 0.2	46.4 ± 0.3	45.2 ± 0.1
D_{max}, Å	175	175	168	167
q range*, Å^{-1}	0.0151-0.2589	0.0149-0.2000	0.0164-0.2150	0.0139-0.2394
χ^2 (total estimate from GNOM)	1.037 (0.82)	1.059 (0.84)	0.977 (0.71)	1.336 (0.72)
Porod volume V_p, 10^3 Å^{-3}	335	345	256	262
Resolution from SASRES, Å	40.39	47.54	42.46	45.74
DATCLASS shape	flat	flat	flat	flat
AMBIMETER score	2.91	2.91	2.77	2.70
Molecular mass determination (ratio to monomeric mass)				
From chemical composition, kDa	51.01289	51.01289	51.01289	50.10885
From Bayesian inference, kDa	138.2 (2.71)	146.8 (2.88)	109.1 (2.14)	109.1 (2.18)
From Size&Shape, kDa	166.0 (3.25)	159.1 (3.12)	111.6 (2.19)	110.4 (2.20)
From volume of correlation V_c, kDa	137.1 (2.69)	146.1 (2.86)	104.6 (2.05)	99.1 (1.98)
Shape model fitting				
DAMMIF (fast, default parameters, P1 symmetry, no anisotropy assumptions, 23 reconstructions):				
NSD (standard deviation)	0.89 (0.17)	1.00 (0.17)	1.47 (0.31)	1.10 (0.21)
DAMMIN (expert mode, $r_{dummy\ atoms}$ = 5 Å):				
χ^2, CorMap *P*-value	1.036, 0.583	1.061, 0.278	0.980, 0.045	1.333, 0.013
Atomistic modelling				
MultiFoXS (parallel dimer, single state, flexible linkers†, 10,000 iterations):				
R_g, Å	45.53	45.75	43.78	42.93
c_1, c_2	1.04, 4.00	1.04, 3.24	0.99, 0.04	1.00, 2.02
χ^2, CorMap *P*-value	2.17, 0.000	1.20, 0.005	1.28, 0.006	1.41, 0.051
MultiFoXS (parallel trimer, single state, flexible linkers†, 10,000 iterations):				
R_g, Å	47.65	48.36	48.16	
c_1, c_2	0.99, -0.50	0.99, -0.50	0.99, -0.50	
χ^2, CorMap *P*-value	7.91, 0.000	4.91, 0.000	16.4, 0.000	
EOM-NNLSJOE (MBP free, CC fixed[ψ], flexible linkers[‡], constant subtraction allowed):				
No. of representative structures	9	8	6	
Oligomer percentage	34.0% dimers, 66.0% trimers	46.6% dimers, 53.4% trimers	93.0% dimers, 7.0% trimers	
Ensemble-averaged R_g, Å	47.70	47.92	44.74	
χ^2, CorMap *P*-value	1.07, 0.203	1.01, 0.940	0.97, 0.310	

*Also used for mass determination, model fitting and atomistic modelling.
†Five-residues linker, 378-382 aa for MBP-Cdc12CC, 382-386 aa for MBP-Cdc12CC+8.
‡Eleven-residues linker, 379-389 aa for MBP-Cdc12CC+8.
ψParallel trimeric CC from AlphaFold (5000 models) and parallel dimeric CC generated from trimer (5000 models).

Table S2 Melting temperatures of Cdc12C wild type and mutants monitored by circular dichroism at 222 nm. Peptide concentration, 10 µM. Values were taken from duplicates.

Peptide	T_m, °C	ΔT_m, °C	Number of states considered during fit	Transition width, °C
Wild type	31.2 ± 0.1	---	2	5.1 ± 0.1
K391N-L392stop (mutant -6)	ND	---	---	14 ± 1
W367K	ND	---	---	8.1 ± 0.3
W367K-E368V	23.6 ± 0.1	-7.4 ± 0.2	2	5.6 ± 0.1
R363K (mutant -122)	30.3 ± 0.1	-0.9 ± 0.2	2	5.9 ± 0.1
W367L	33.8 ± 0.1	2.6 ± 0.2	2	5.2 ± 0.1
E368K	31.7 ± 0.1	0.5 ± 0.2	2	6.1 ± 0.1
E368Q	34.4 ± 0.1	3.2 ± 0.2	2	6.1 ± 0.1
E368V	55.4 ± 0.2	24.2 ± 0.3	3*	4.8 ± 0.2

*Second transition at T_m = (27 ± 3) °C.

Table S3 Circular dichroism spectral analysis of wild-type and mutant purified Cdc12 CTD. The 222/208 nm ratio, indicative of coiled-coil assemblies, and the secondary structure determination by BeStSel (Micsonai *et al.* 2025) are presented. Peptide concentration, 10 µM. Temperature, 4 °C.

Peptide	222/208 nm ratio ± 0.04	Secondary structure determination, %			
		Regular helix	Distorted helix	Helices (regular+ distorted)	Other
Wild type	0.99	70.6	22.9	93.5	6.5
K391N-L392stop (mutant -6)	0.72	20.2	11.1	31.2	68.8
W367K	0.83	29.7	14.2	44.0	56.0
W367K-E368V	0.88	37.6	17.7	55.3	44.7
R363K (mutant -122)	1.02	54.9	18.9	73.9	26.1
W367L	0.96	58.2	22.5	80.7	19.3
E368K	0.99	62.6	21.9	84.5	15.5
E368Q	0.96	67.9	21.1	89.0	11.0
E368V	0.93	46.0	17.6	63.5	36.5

Table S4 Calculated mass of peptides in the SEC-MALS experiments.

Peptide	**Calculated mass, kDa (ratio to monomer)**
Cdc3	
413-520 (Cdc3C)	
wild type	12.7 ± 0.9 (1.0)
427-520 (Cdc3CC)	
wild type	9.6 ± 0.7 (1.0)
Cdc12	
316-407 (Cdc12C)	
wild type	29.0 ± 1.3 (2.6)
K391N-L392stop (mutant -6)	9.9 ± 0.1 (1.1)
W367K	12.4 ± 0.3 (1.1)
W367K-E368V	16.2 ± 1.6 (1.4)
R363K (mutant -122)	24.6 ± 0.6 (2.2)
W367L	25.5 ± 0.7 (2.3)
E368K	22.0 ± 0.3 (1.9)
E368Q	28.2 ± 0.7 (2.5)
E368V	35.2 ± 0.6 (3.1)
341-407 (Cdc12CC)	
wild type	22.2 ± 1.0 (2.6)

Table S5 Sequences of select oligonucleotides used in this study.

Primer name	Sequence (5' to 3')
Cdc12-GFP(1-9)fw	AACTAGAAGAGCAGGTCAAAAGCTTGCAAGTAAAAAAATCCCATTTAAAAAT GAGAAAGGGTGAAGAATTGTTTACTG
Cdc12-GFP(1-9)re	AGAGAGAGGTACATACATAAACATGCGCGCACAAAAGCAGAGATTATCTATC ATGAACCGTTGTCAGGTAATAAGAC
Cdc12-GFP(10)fw	AACTAGAAGAGCAGGTCAAAAGCTTGCAAGTAAAAAAATCCCATTTAAAAGA TTTGCCAGATGATCATTATTTGTCTACTCAAACTATTTTGTCTAAAGA
Cdc12-GFP(10)re	GTTGTAAAACGACGGCCAGTGAATTCGAGCTCGGTACCCGGGGATCCTCAATT CAAATCTTTAGACAAAATAGTTTGAGTAGACAAATAATGATCATCTG
Cdc12-GFP(11)fw	AAGAGCAGGTCAAAAGCTTGCAAGTAAAAAAATCCCATTTAAAAGGATCCGA AAAAAGAGATCATATGGTTTTGTTGGAATATGTTACTGCTGCTGGTAT
Cdc12-GFP(11)reFIXED	AGTCACGACGTTGTAAAACGACGGCCAGTGAATTCGAGCTCGGTACCCGGCTA AGAAGCATCAGTAATACCAGCAGCAGTAACATATTCCAACAAAACCA
FLAP-Y Cy3	Cy3-AATGCATGTCGACGAGGTCCGAGTGTAA-Cy3
FLAP-Y Cy5	Cy5-AATGCATGTCGACGAGGTCCGAGTGTAA-Cy5
Cdc10_FISHa	CAGGCTGTACTGAGCTGAGAGGATCCttacactcggacctcgtcgacatgcatt
Cdc10_FISHc	CTTCAACAGACGATGTTCGATCTGttacactcggacctcgtcgacatgcatt
Cdc10_FISHe	GAGTACTTTTACCCAATCCGGttacactcggacctcgtcgacatgcatt
Cdc10_FISHg	CAGGCAGGGCAGAAATATCATCACCAGttacactcggacctcgtcgacatgcatt
Cdc10_FISHh	CAAGCGAACGCGGTCCTCCACAAGAGttacactcggacctcgtcgacatgcatt
Cdc10_FISHj	CACAATAGGCTCCCAAGCTTTAGttacactcggacctcgtcgacatgcatt
Cdc10_FISHl	CACGTTGGGCTGTCAATTCTTTACGttacactcggacctcgtcgacatgcatt
Cdc10_FISHo	CAAGGCTTCAACGTCAAGGCGGCTCttacactcggacctcgtcgacatgcatt
Cdc10_FISHq	GCTCCCTAAACTCCGTTCTTTCATCttacactcggacctcgtcgacatgcatt
Cdc10_FISHs	CCAACCACTGCAAACGGAATGATAGATCttacactcggacctcgtcgacatgcatt
Cdc10_FISHu	GCGCTCCAACGAGTTTTTCTTCCCCTGttacactcggacctcgtcgacatgcatt
Cdc10_FISHv	CACACTGGTTGATATCCTCAACttacactcggacctcgtcgacatgcatt
Cdc10_FISHw	GGAGATGAGTTCGAATCAAAAATTCCCttacactcggacctcgtcgacatgcatt
Cdc10_FISHx	GGCAATTAATTGTCTTGCTCTGAACCCttacactcggacctcgtcgacatgcatt
Cdc10_FISHy	GACATATGAGCTGAGGAACGACTATTCGCttacactcggacctcgtcgacatgcatt
Cdc10_FISHz	GAGATTCAACGTTGAATGGCGTTGCttacactcggacctcgtcgacatgcatt
Cdc3_FISHa	CGTTCAGTTGTCGTGTGATCCTGGttacactcggacctcgtcgacatgcatt
Cdc3_FISHc	CCTGCTTAATGGACACTTGTTCCTCCttacactcggacctcgtcgacatgcatt
Cdc3_FISHd	GATCATGCTGACGCTCTTCTTGTTCCGttacactcggacctcgtcgacatgcatt
Cdc3_FISHf	CGTGTACTGCGAGTCCACTCCATCATGttacactcggacctcgtcgacatgcatt
Cdc3_FISHg	CTCTCGCTGTCGTCATTTTGCGTACCGttacactcggacctcgtcgacatgcatt
Cdc3_FISHh	CCACCTTTACATCGGATTCAGCTGCCTCttacactcggacctcgtcgacatgcatt
Cdc3_FISHi	GGTGATGCCCATACCGAGGCCGGGttacactcggacctcgtcgacatgcatt
Cdc3_FISHj	GGTCAGGCAGAACTTGACCCTTTTCGCTttacactcggacctcgtcgacatgcatt
Cdc3_FISHk	GACGACGAATGAACTTAATCTCCGGttacactcggacctcgtcgacatgcatt
Cdc3_FISHm	CCGTTCTTTATGGACCTTCTGTGCCttacactcggacctcgtcgacatgcatt
Cdc3_FISHn	CCATCAGGGCCGACACATAGGAGttacactcggacctcgtcgacatgcatt
Cdc3_FISHp	GACCCTCGCCCTGACCCTCCttacactcggacctcgtcgacatgcatt
Cdc3_FISHs	CAATCTCCTTAATGATCGGGTCCCttacactcggacctcgtcgacatgcatt
Cdc3_FISHv	CCCCCCATGGATAGGAACGGCCttacactcggacctcgtcgacatgcatt
Cdc3_FISHy	CCCTTCTTCTTTGTAGGGACGGGGGttacactcggacctcgtcgacatgcatt
Ash1_FISHd	GATGTGGCGATGCTGGTGCAGttacactcggacctcgtcgacatgcatt
Ash1_FISHi	GAGACGGACGATAGCCTGTCttacactcggacctcgtcgacatgcatt

Ash1_FISHj	GGCTTTGTTGTGGGCGCTCCGGttacactcggacctcgtcgacatgcatt
Ash1_FISHl	GATGTATCAGGGAAGCGTGCTGCGttacactcggacctcgtcgacatgcatt
Ash1_FISHq	CGGCGGTGTGACGGGAGGAGttacactcggacctcgtcgacatgcatt
Ash1_FISHs	GAGGCCTCTACTCCTCTAAGCGttacactcggacctcgtcgacatgcatt
Ash1_FISHx	GCCTTGGGACGCACAGGTGAGGttacactcggacctcgtcgacatgcatt
Ash1_FISHy	GGGTGACCTTGGGCTTGGttacactcggacctcgtcgacatgcatt
Ash1_FISHz	GAGGGGGAGAGTCGAGAGCttacactcggacctcgtcgacatgcatt
Ash1_FISHaa	GAGCCACTGGACCTTCTACTTCCCttacactcggacctcgtcgacatgcatt
Ash1_FISHbb	CACTCTTGTGGTGTGACGAGTGGGttacactcggacctcgtcgacatgcatt
Ash1_FISHdd	GCTTTCTTGGCGACCACGATGGCCttacactcggacctcgtcgacatgcatt
Ash1_FISHgg	CGCAGTTGCGTTCGGGGACGttacactcggacctcgtcgacatgcatt
Abp140_FISHa	GGTAGCATCGCCTTCTTCCTttacactcggacctcgtcgacatgcatt
Abp140_FISHb	CCTCTTGCGGAACAGCAGTAGACTCttacactcggacctcgtcgacatgcatt
Abp140_FISHc	GGAGCCCTCTTCTTCGTCTTCTTCGttacactcggacctcgtcgacatgcatt
Abp140_FISHd	CTTGCAAGAACTTCAGCGCCAGttacactcggacctcgtcgacatgcatt
Abp140_FISHe	CCTTCAGTTTCCTCAGCCACACCttacactcggacctcgtcgacatgcatt
Abp140_FISHf	CTTCGGCTGGTTCAGATGCAttacactcggacctcgtcgacatgcatt
Abp140_FISHg	GCTGTCGTCGACATTAGCGTTGGTGttacactcggacctcgtcgacatgcatt
Abp140_FISHh	CGTGGTGTCGCCGGTTGTATCATCAttacactcggacctcgtcgacatgcatt
Abp140_FISHi	CACTTCTTGAATGGCGGAGGttacactcggacctcgtcgacatgcatt
Abp140_FISHj	CCTCTGCCCTCGTGCGCAATATTCTCttacactcggacctcgtcgacatgcatt
Abp140_FISHk	CTGCATTCTGATCGCCTGTGttacactcggacctcgtcgacatgcatt
Abp140_FISHl	GTCGCGGCCTATTCTTGAACCttacactcggacctcgtcgacatgcatt
Abp140_FISHm	GATCCCAAACGTCAGATTCCTCGGttacactcggacctcgtcgacatgcatt
Abp140_FISHn	CCTCCGCCTGCTGGACTTGTttacactcggacctcgtcgacatgcatt
Abp140_FISHo	GTCCCAATAACGTGCCGGATttacactcggacctcgtcgacatgcatt
Abp140_FISHp	CTAATTCGACGGCTCTTGGAGCttacactcggacctcgtcgacatgcatt
Abp140_FISHq	CCATACTGTTGCGTGGCCGTttacactcggacctcgtcgacatgcatt
Abp140_FISHr	GAGGTTCGACGCCATCAGGTAAttacactcggacctcgtcgacatgcatt
Abp140_FISHt	CAGCTTGTACCCAGCAGCGGttacactcggacctcgtcgacatgcatt

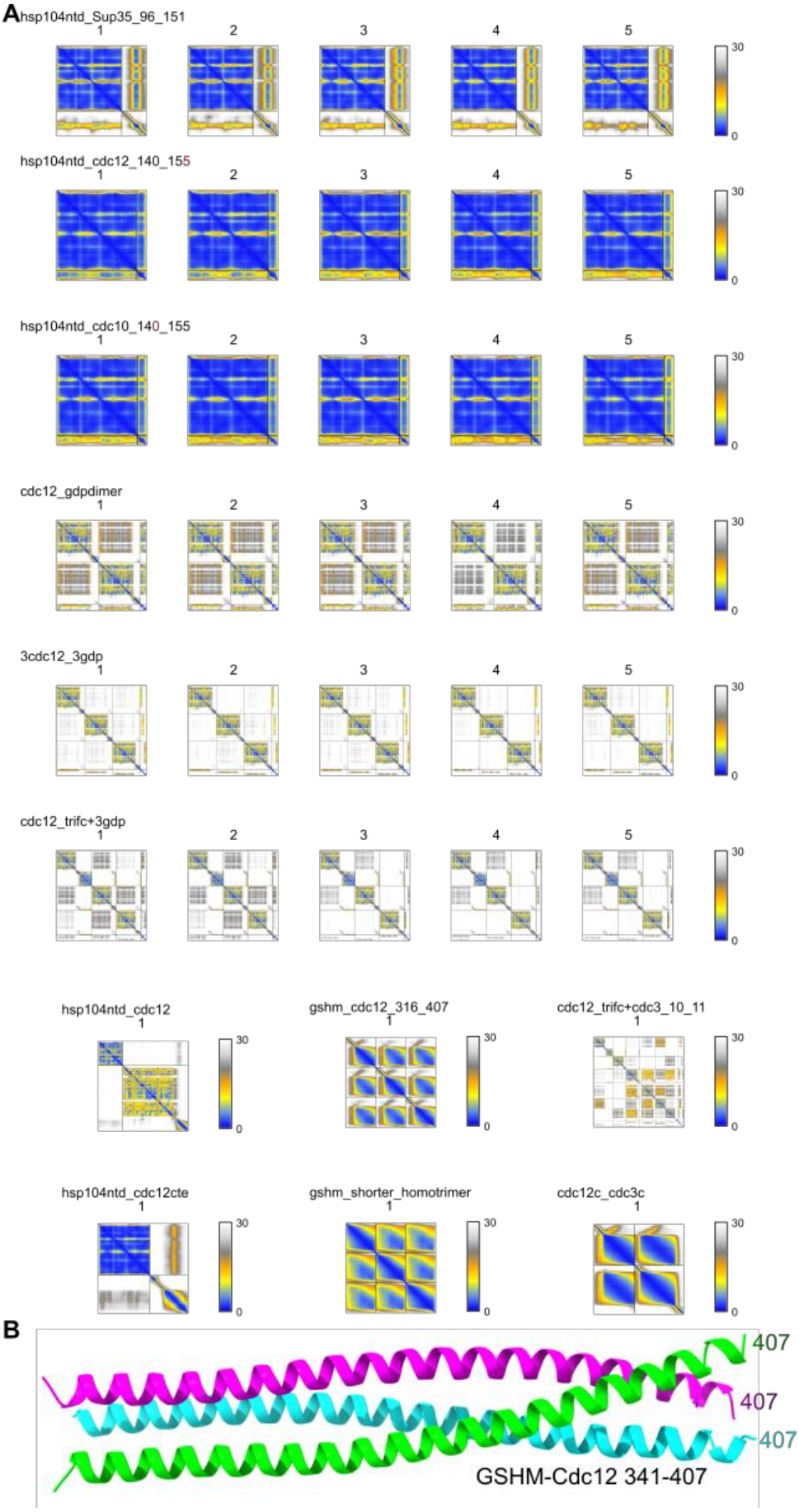
A
hsp104ntd_Sup35_96_151
hsp104ntd_cdc12_140_155
hsp104ntd_cdc10_140_155
cdc12_gdpdimer
3cdc12_3gdp
cdc12_trifc+3gdp
hsp104ntd_cdc12
gshm_cdc12_316_407
cdc12_trifc+cdc3_10_11
hsp104ntd_cdc12cte
gshm_shorter_homotrimer
cdc12c_cdc3c
1
2
3
4
5
30
0
B
407
407
407
GSHM-Cdc12 341-407

Figure S1. AlphaFold Multimer modeling metrics and output. (A) Predicted Aligned Error matrices for the AlphaFold3 predictions in this study. (B) Top-ranked AlphaFold3 prediction for Cdc12 residues 341-407 with residual N-terminal sequence GSHM from protease cleavage.

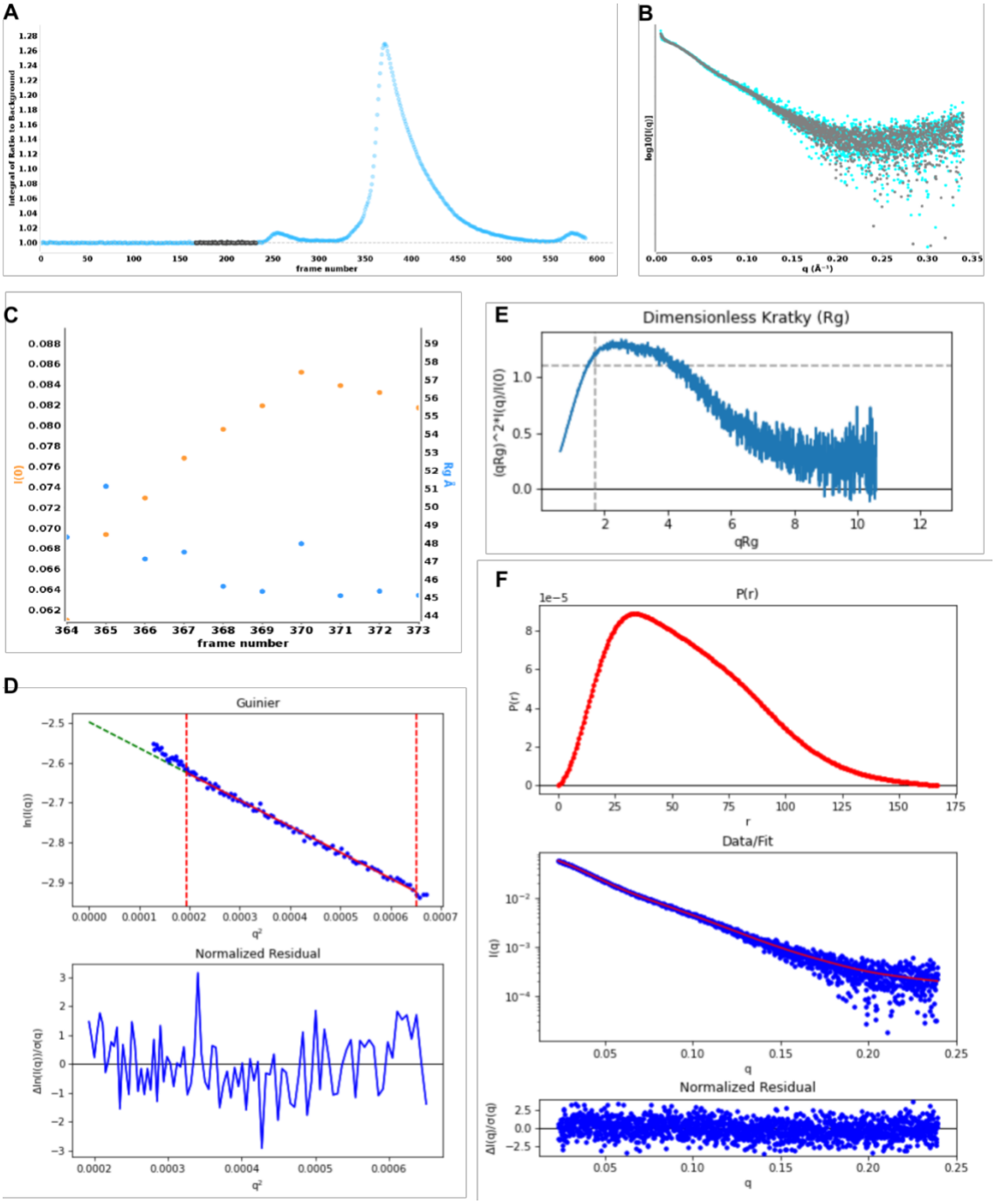

Figure S2. SEC-SAXS of MBP-Cdc12CC. (A) SEC profile (blue dots) showing regions used for buffer subtraction (gray dots). (B) Log10 intensity plot of subtracted and merged SAXS frames (black dots, average; cyan dots, median). (C) $I(0)$ (orange) and R_g (blue) across the selected frames. (D) Guinier fit and residuals for data at $q*R_g < 1.3$. (E) Dimensionless Kratky plot with crosshair (1.10, 1.73) indicating the expected peak maxima for a globular protein. F) $P(r)$ distribution (top) with the fit of the $P(r)$ profile in red to the raw scattering data in blue (middle) and the normalized residuals (bottom).

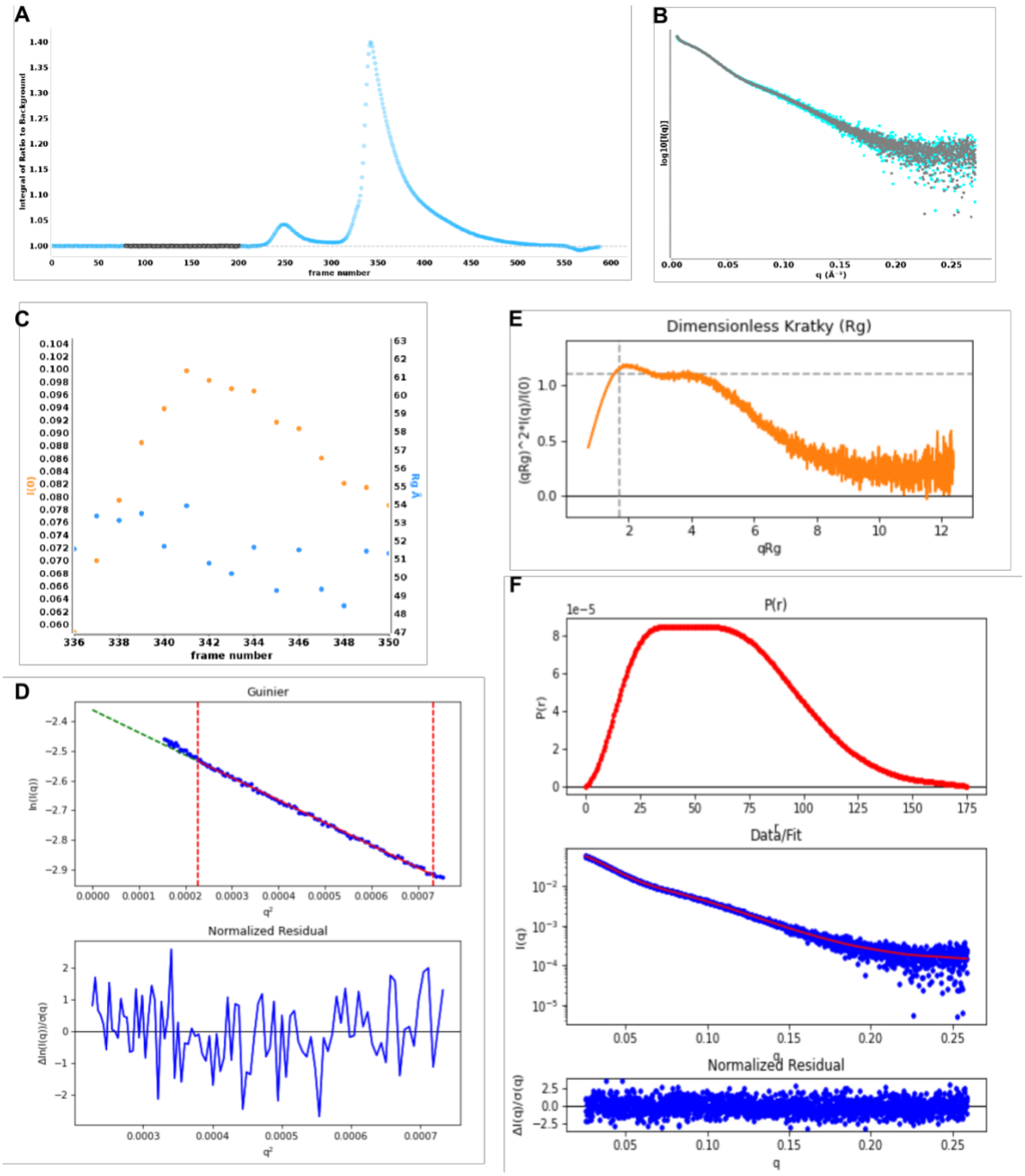

Figure S3. **SEC-SAXS of MBP-Cdc12CC+8.** As in Fig. S2 but for MBP-Cdc12CC+8.

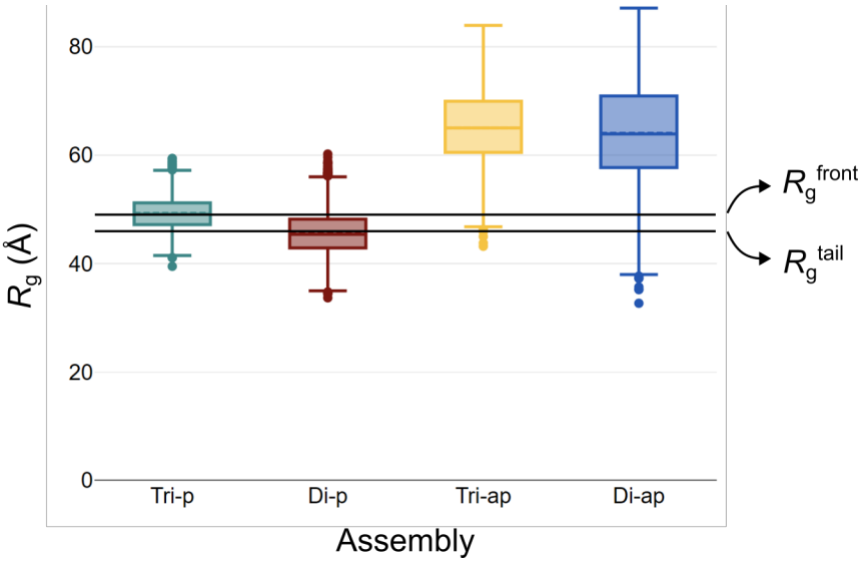

Figure S4. **Box plot of the radius of gyration (R_g) from MBP-Cdc12CC+8 assemblies generated by RANCH.** A total of 5,000 models were made for each assembly (tri-p, parallel trimer; di-p, parallel dimer; tri-ap, antiparallel trimer; di-ap, antiparallel dimer). Real space R_g's from the peak front and the peak tail datasets (horizontal black lines) match well with the mean and median of those from tri-p and di-p models, respectively. Antiparallel assemblies were not considered for NNLSJOE analysis due to the large difference between their R_g's and the experimental R_g's.

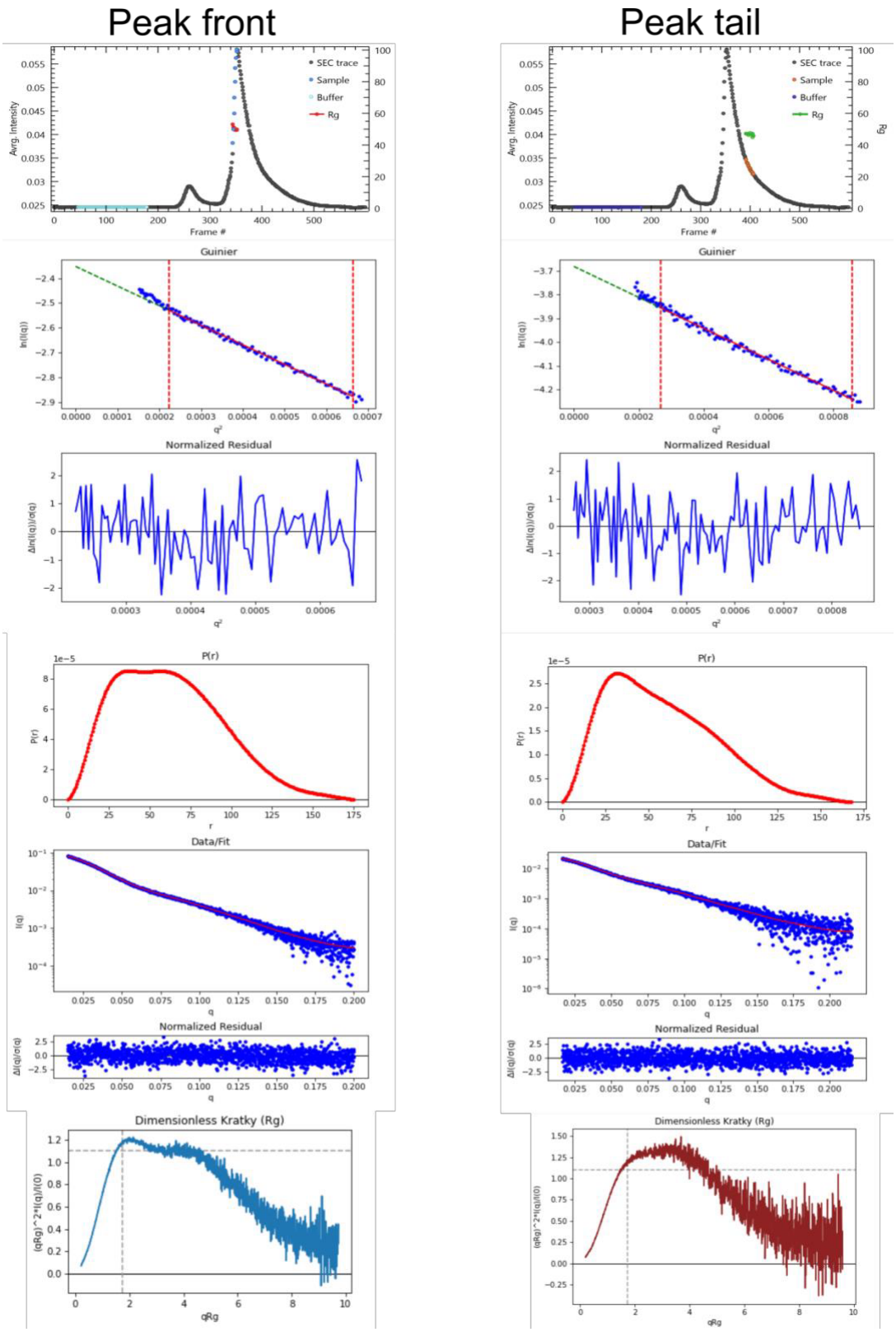

Figure S5. SAXS analyses of MBP-Cdc12CC+8 SEC fractions. SEC profiles, Guinier fit and residuals, *P*(*r*) distribution, fit and normalized residuals and Dimensionless Kratky plots are shown. Significant differences can be seen in the *P*(*r*) and Kratky plots.

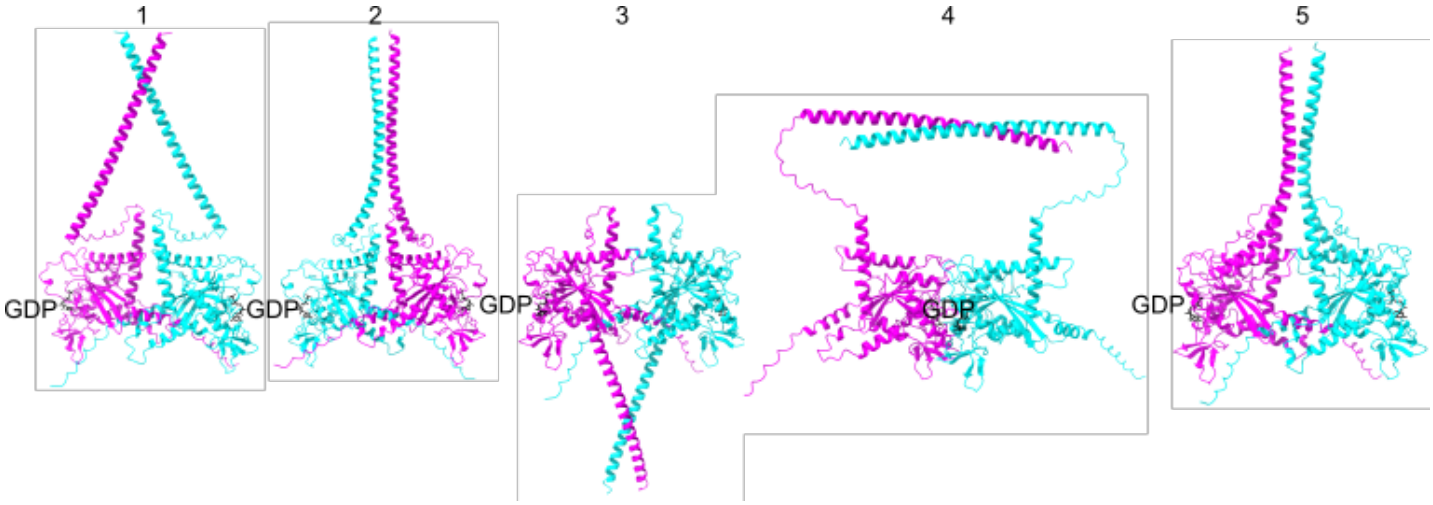

Figure S6. Canonical septin-septin interfaces between GTPase domains in AlphaFold3 predictions of Cdc12•GDP homodimers. Numbers indicate the confidence ranking of the models. "GDP" labels the nucleotide bound in the nucleotide-binding pocket, which is buried in the septin G interface. The septin-septin NC interface is located on the opposite side of the GTPase domain. pAE matrices are in Figure S1. Models have been deposited in ModelArchive, accession code ma-5hhc4.

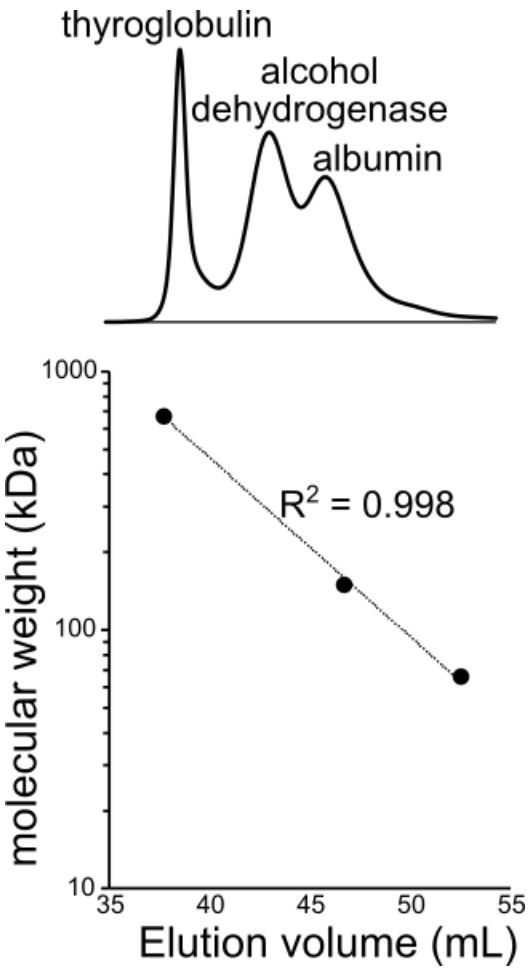

Figure S7. Calibration of Sephacryl S200 column size exclusion column with molecular weight standards. A mix of the indicated proteins dissolved in PBS was separated at 0.5 mL/min. The top chromatogram shows absorbance at 260 nm, and the lower plot shows the elution volumes at each peak versus molecular weight. The R^2 value shows the coefficient of variation of the three points fit to a line.

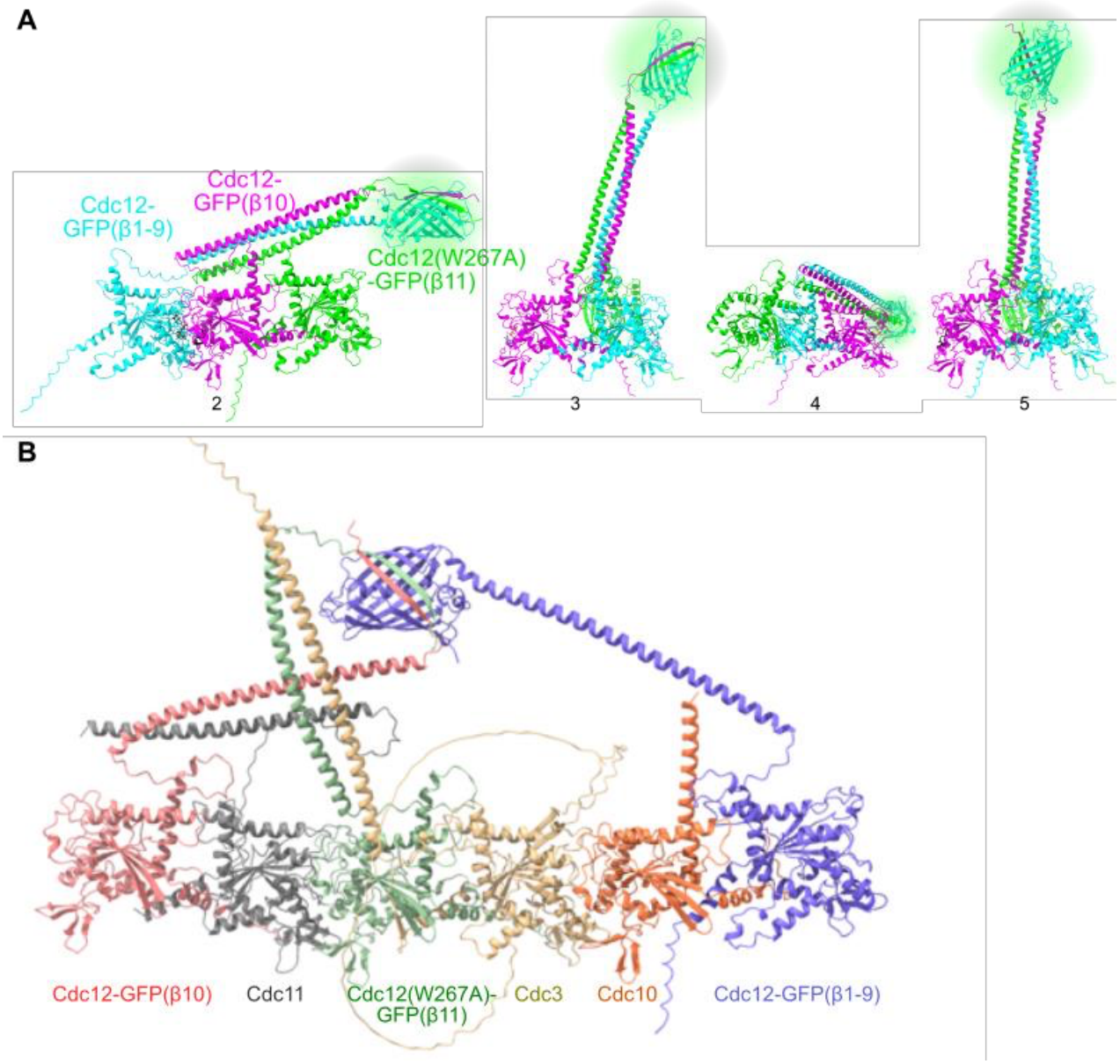

Figure S8. AlphaFold3 predictions of Cdc12 TriFC complexes. (A) As in Fig. 3C, showing the other four top-ranked models. pAE matrices are in Figure S1. Models have been deposited in ModelArchive, accession code ma-s4slk. (B) The top-ranked prediction when Cdc3•GTP, Cdc10•GDP, and Cdc11•GDP were added to the prediction. pAE matrix is in Figure S1. Model has been deposited in ModelArchive, accession code ma-37ka2.

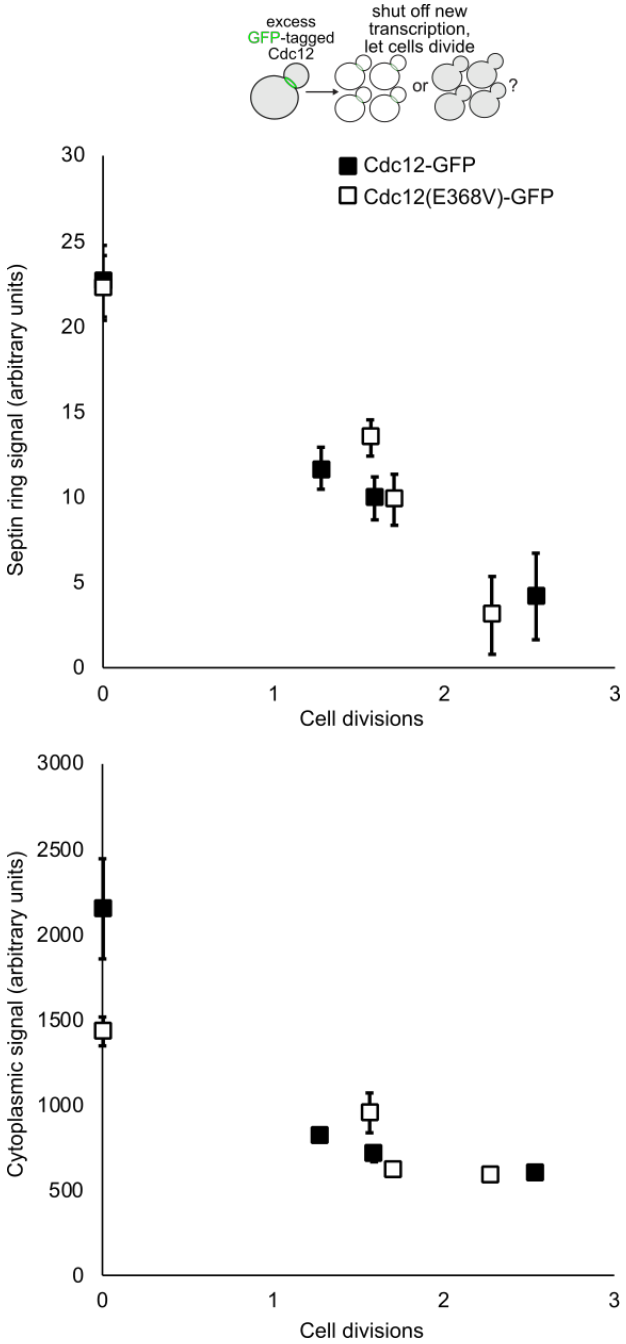

Figure S9. Post-translational assembly into septin filaments by Cdc12-GFP and Cdc12(E368V)-GFP. A pool of excess Cdc12-GFP or Cdc12(E368V)-GFP was generated in wild-type haploid cells (strain BY4741) carrying plasmid pMVB2 or BD7C264E by culturing cells in plasmid-selective medium containing 0.1% galactose and 1.9% raffinose, then new expression of the GFP-tagged Cdc12 was repressed by changing to medium with 2% glucose. Cell concentration per mL was monitored with a hemacytometer at various time points as the glucose cultures grew, and the number of cell divisions was calculated. At the same time points, GFP fluorescence was measured in 24-38 cells per time point per genotype via microscopy using a line scan of bud necks (septin filaments) or a circular area of the cytoplasm. Each point indicates the mean and error bars are standard error of the mean. Cytoplasmic signal is expected to decrease exponentially as the excess Cdc12-GFP is diluted via cell division; if some of the excess septins are able to assemble into septin hetero-octamers and filaments, then the septin ring signal is expected to decrease in a non-exponential manner (Hassell *et al*, 2022).

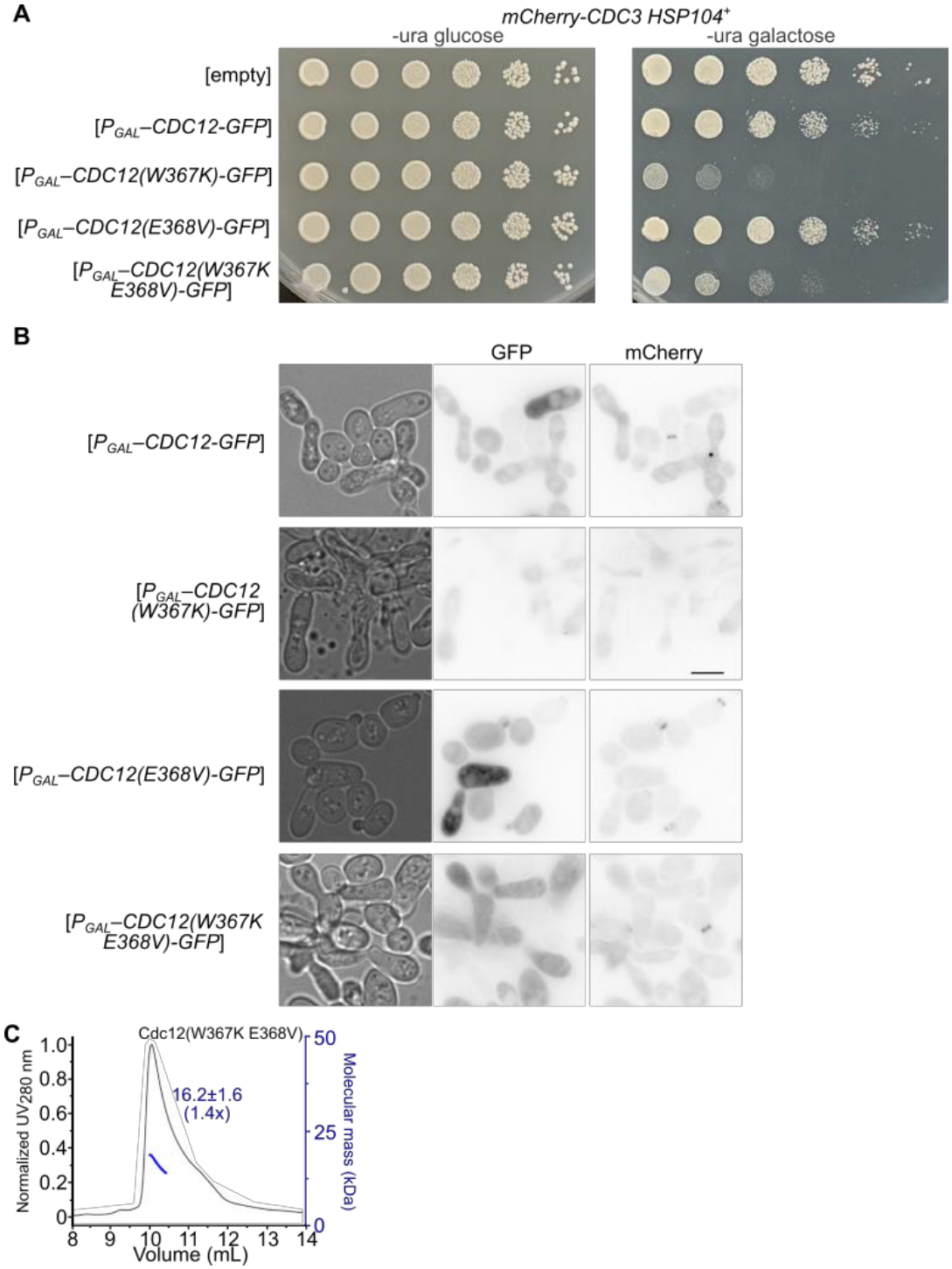

Figure S10. Mutations altering Cdc12 CTD oligomerization state exacerbate dominant perturbation of septin function caused by overexpression of GFP-tagged Cdc12 in cells with mCherry-tagged Cdc3. (A) Yeast strain H07151 carrying plasmid pMVB2 ("*P_{GAL}–CDC12-GFP*"), C6F1B99E ("*P_{GAL}–CDC12(W367K)-GFP*"), (BD7C264E ("*P_{GAL}–CDC12(E368V)-GFP*"), or 9F2B6E98 ("*P_{GAL}–CDC12(W367K E368V)-GFP*") was serially diluted and spotted on solid medium selective for the plasmids and either glucose or galactose as the carbon source. Plates were incubated at 30˚C for 2 days prior to imaging. (B) Cells were scraped from the galactose plates in (A) and imaged with transmitted light or the GFP (60-msec exposure) or mCherry (250-msec) cube. Scale bar, 5 µm. (C) As in Fig. 1D, but with Cdc12 residues 316-407 harboring both the W367K and E368V mutations.

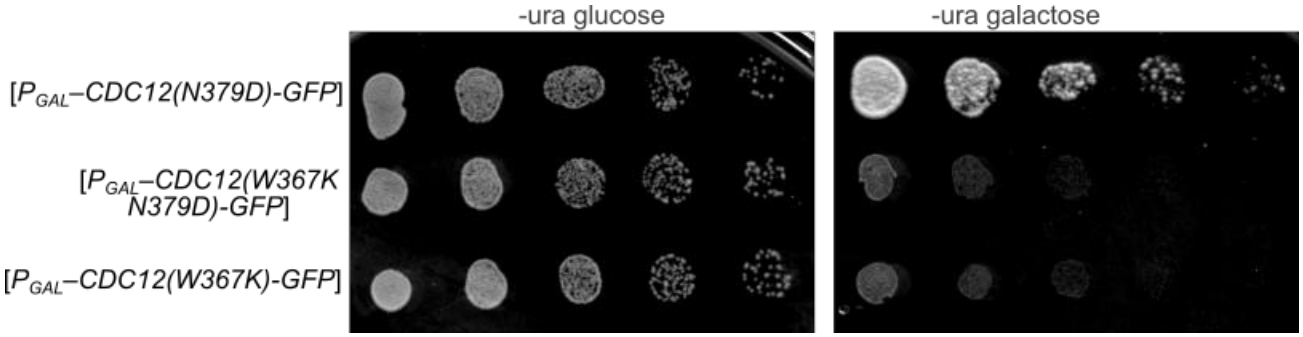

Figure S11. **The unanticipated mutation N379D discovered in the Cdc12-GFP-overexpressing plasmid is not responsible for the dominant lethal effects of the W367K mutation.** Dilution series as in Fig. 4A, plasmids were pMVB2 ("P_{GAL}–*CDC12(N379D)-GFP*") C6F1B99E ("P_{GAL}–*CDC12(W367K N379D)-GFP*"), or 10633A79 ("P_{GAL}–*CDC12(W367K)-GFP*").

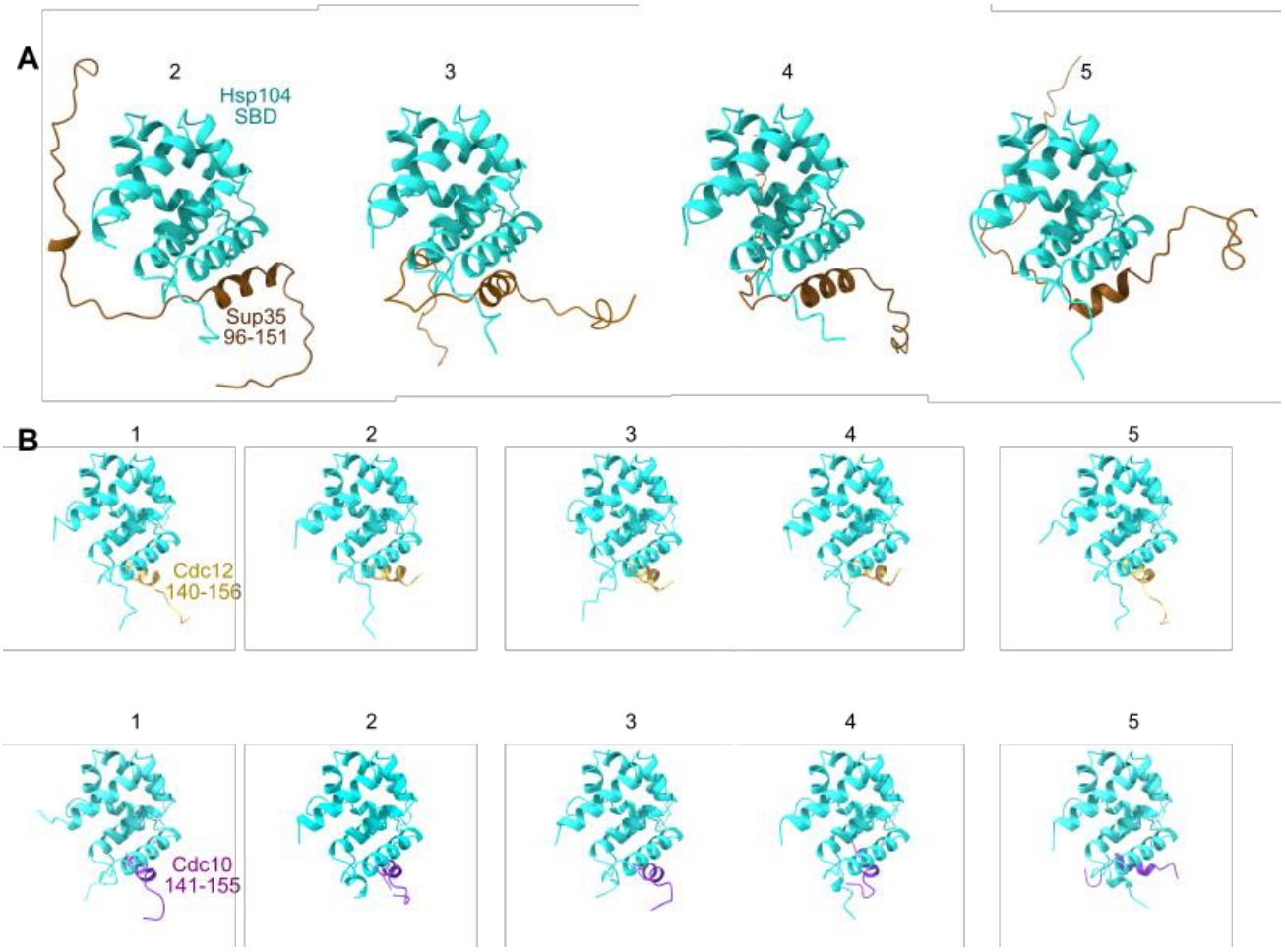

Figure S12. AlphaFold3 predictions of Hsp104–substrate binding. As in Fig. 6A, but showing the substrate-binding domain (SBD) of Hsp104 bound to the indicated peptides from Sup35 (deposited in ModelArchive, accession code ma-vj5d5), Cdc12 (ma-k1rre), or Cdc10 (ma-5n6qq). pAE matrices are in Figure S1.

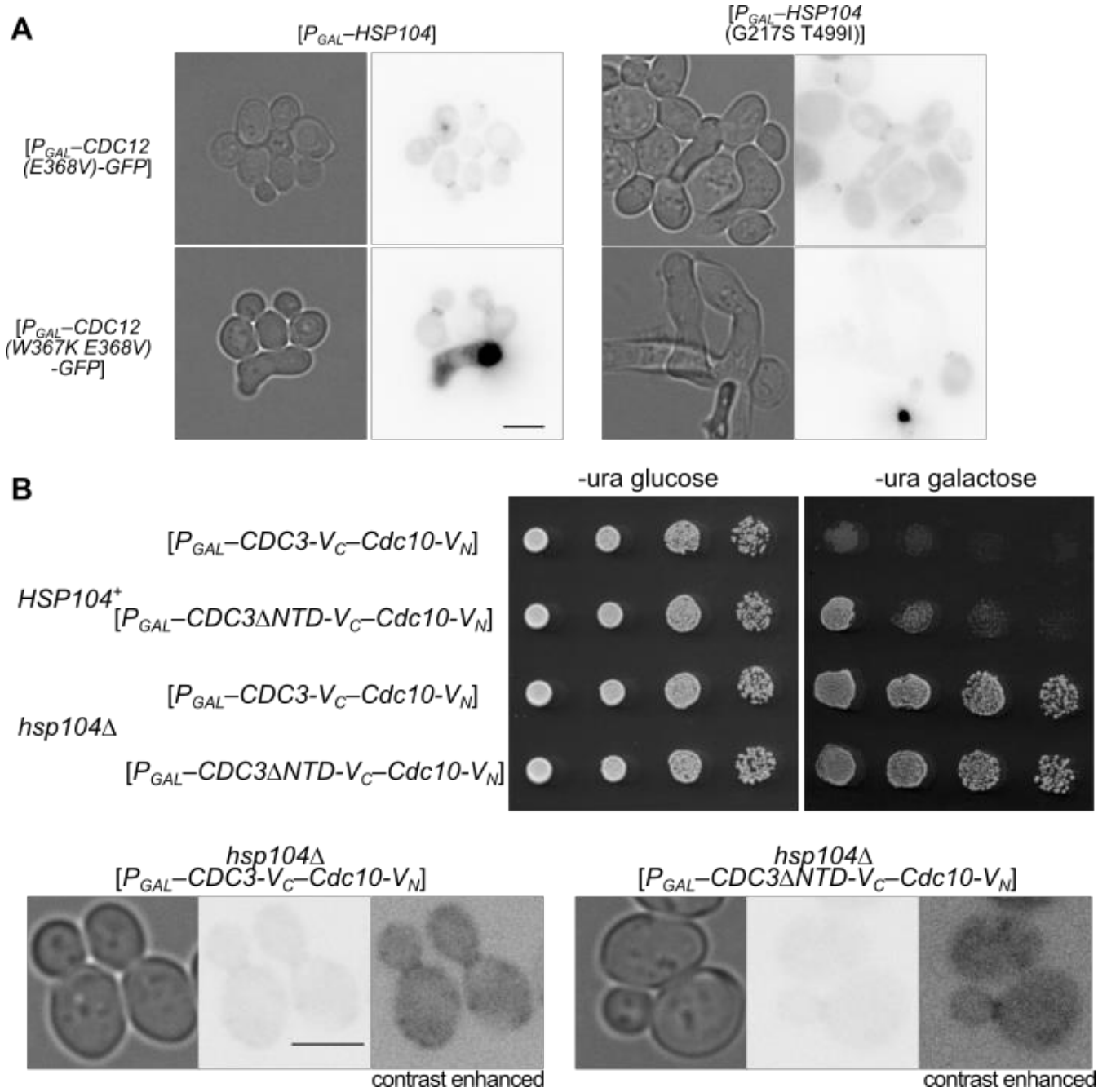

Figure S13. Colony growth, cellular morphology, and/or septin localization upon overexpression of septins and/or Hsp104. (A) As in Fig. 4C, but with cells of strain BY4741 scraped from the galactose plates in Fig. 6C. GFP images had 60-msec exposures. Scale bar is 5 µm. Plasmids were 5679 ("P_{GAL}–*HSP104*"), 5707 ("P_{GAL}–*HSP104(G217S T499I)*"), (BD7C264E ("P_{GAL}–*CDC12(E368V)-GFP*"), and 9F2B6E98 ("P_{GAL}–*CDC12(W367K E368V)-GFP*")

(B) Top, as in Fig.9C but with plasmids E00432 (P_{GAL}–*CDC3-*V_C–*CDC10-*V_N"), and E00435 ("P_{GAL}–*CDC3ΔNTD*–V_C–*CDC10-*V_N"). Bottom, cells scraped from the galactose plates were imaged with transmitted light and the GFP cube (1-sec exposures). As indicated, images with increased contrast are also provided. Scale bar, 5 µm.

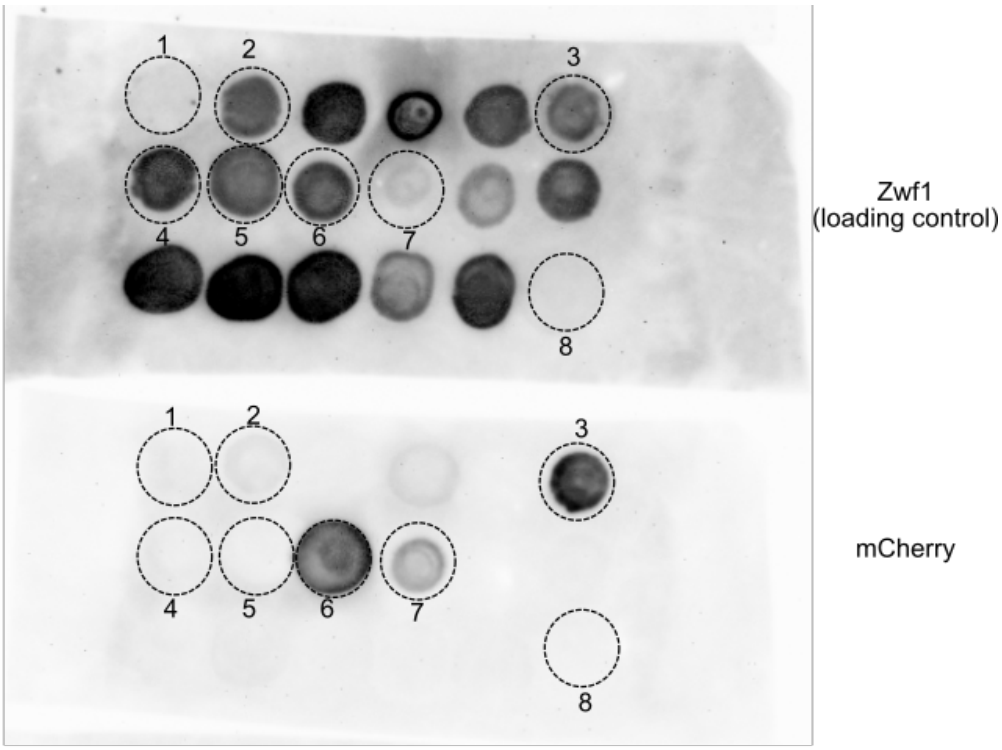

1. loading buffer
2. *HSP104*$^{+}$ *CDC3-mCherry*
3. *HSP104*$^{+}$ [P_{GAL}–*CDC10-GFP–CDC3-mCherry*]
4. *hsp104*Δ [P_{GAL}–*CDC10-GFP–CDC3-mCherry*]
5. *HSP104*$^{+}$ *CDC11-mCherry SHS1-GFP*
6. *HSP104*$^{+}$ [P_{GAL}-*CDC11-mCherry*]
7. *hsp104*Δ [P_{GAL}-*CDC11-mCherry*]
8. loading buffer

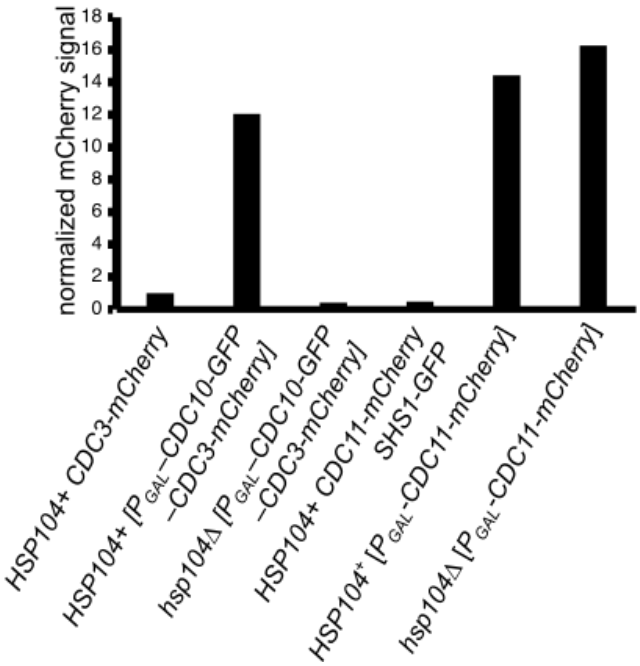

Figure S14. Immunoblotting of levels of tagged septins. Top, membranes were spotted with protein extracts and exposed to anti-mCherry or, as a loading control, anti-Zwf1 antibodies, followed by detection with peroxidase-conjugated secondary

antibodies. Chemiluminescent signal was detected with an imaging system and quantified as described in the Methods. Bottom, normalized mCherry signal for the spots indicated with the key.